DETERMINING THE CONTROL OBJECTIVES OF A SWITCHED RELUCTANCE MACHINE FOR PERFORMANCE IMPROVEMENT IN GENERATING MODE

DETERMINING THE CONTROL OBJECTIVES OF A SWITCHED RELUCTANCE MACHINE FOR PERFORMANCE IMPROVEMENT IN GENERATING MODE

BY

AHSAN ZAHID, B.Sc.

A THESIS

SUBMITTED TO THE DEPARTMENT OF ELECTRICAL & COMPUTER ENGINEERING AND

SCHOOL OF GRADUATE STUDIES IN PARTIAL FULFILLMENT OF THE REQUIREMENTS

FOR THE DEGREE OF MASTER OF APPLIED SCIENCE

Master of Applied Science (2022)	McMaster University
(Electrical & Computer Engineering)	Hamilton, Ontario, Canada

TITLE: Determining the Control Objectives of a Switched

                  Reluctance Machine for Performance Improvement in

                  Generating Mode

AUTHOR: M. Ahsan Zahid

                  B.Sc. (Electrical Engineering)

                  Ryerson University, Toronto, Canada

SUPERVISOR: Dr. Berker Bilgin

                  Ph.D. (Electrical & Computer Engineering)

                  Illinois Institute of Technology, Chicago, US

NUMBER OF PAGES: xix, 155

To my parents

Zahid & Rehana

Abstract

Switched reluctance machines are becoming more prevalent in various motor drive applications due to their simple construction, robust design, fault tolerant operation, and relatively low-cost construction. There are nonetheless some drawbacks to the switched reluctance machines operational behavior which limit its potential market penetration. The electromagnetic torque ripple is one of those limitations. However, unlike most four-quadrant variable speed electric motors, switched reluctance machines need additional control considerations to operate in generating mode to maximize power returned while minimizing torque ripple.

The goal of this thesis is to explore different control schemes which are used in motoring mode and compare their performance in generating mode for different operational points. Using the lessons learned from the comparisons in generating mode, key optimizations objectives are established to improve the switched reluctance machines performance for generating applications. A multi-objective optimizer is used to select conduction angles using established objectives of maximizing torque and minimizing torque ripple. The proposed generating-specific objectives are compared to the motoring-specific objectives to validate the generating performance improvement for a wide torque-speed range.

Finally, a setup is constructed to validate the generating performance of a 3-phase 12/8 SRM using the new optimization objectives and it is compared with conventional objectives.

Acknowledgements

First and foremost, I would like to thank my supervisor Dr. Berker Bilgin for giving me the opportunity to work in his research lab and supporting me throughout my graduate studies for the past two years. Dr. Berker played a vital role in my success by providing guidance, encouragement, and support not only for my thesis but also for my industry project and career goals. For that I am very grateful, as everything I have achieved would not be possible without him.

Next, I would like to thank my colleagues and friends at MARC 219: Ehsan, Moien, Francisco, and Aniruddha for helping me to deploy the setup used for my thesis. We began working in an empty lab room with absolutely no provision for a experimental setup. Despite COVID restrictions they were able to tackle all difficult challenges to deploy a robust and reliable four-quadrant SRM setup. I will miss having a committed and motivated team who are enjoyable to work with.

Lastly, I would like to thank my family and especially my parents. I would not have these opportunities if it wasn't for their encouragement and support throughout my academics, career, and personal life. I never had to worry about daily life challenges besides my academics and for that there are no words that can express my gratitude and thankfulness. I hope I have made them proud.

Contents

List of Figures

x

List of Tables

List of Abbreviations

AC   alternating current

ADC   analog-to-digital converter

ASD   asymmetric bridge drive

CAD   computer-aided design

CCW   counter clockwise

CPU   central processing unit

CW   clockwise

DC   direct current

EV   electric vehicle

FEA   finite element analysis

FPGA   field-programmable gate array

GA   genetic algorithm

GHG   greenhouse gas

GPIO   general-purpose input/output

IM   induction machine

IO   input/output

IPM   interior permanent magnet motor

LUT   look-up table

MOSFET metal-oxide-semiconductor field-effect transistor

NEMA   National Electrical Manufacturers Association

PC	personal computer
PF	power factor
PM	permanent magnet
PMSM	permanent magnet synchronous machine
RMS	root mean square
SOC	state of charge
SRG	switched reluctance generator
SRM	switched reluctance motor
TSF	torque sharing function

Chapter 1. Introduction

1.1 – Motivation

In recent years there is incentive to utilize methods of transportation which produces lower emissions and are less dependent on volatile natural resources. This paradigm shift has resulted in the transportation industry to utilize electric drives for propulsion, regeneration, and auxiliary vehicular operations. Electric drives convert electrical energy into mechanical energy and can convert mechanical energy into electrical energy. Relative to their combustion counter parts, electric drives are more efficient in converting an energy source to mechanical work, with minimal losses being attributed to electrical and mechanical conversion processes which are dissipated as heat. Additionally, electric drives can convert mechanical energy into electrical energy, which the conventional combustion propulsion method is not capable of. With these benefits, there is an increase in electrical drives replacing combustion applications beyond the transportation sectors.

From the years 2000 to 2018, greenhouse gas (GHG) emissions from the transportation sector in Canada have risen by 27 %, with this large increase in GHG being attributed to an increase in passenger and freight vehicles. Furthermore, there was an increase in energy demand by 17 % from the years 2000 and 2017 [1]. With the continued growth in passenger vehicles and freight trucks spurred on by an increase in light passenger truck sales, online commerce, and trade globalization; the Canadian energy supply could be greatly burdened by the increase in demand and increase the production of harmful GHGs, which can result in irreversible

effects to the climate. Electrification of the transportation sector can result in the reduction of crude oil energy supply dependance and reduce GHG emissions into the atmosphere. There are government incentives in Canada for electrified vehicles to aid in the increase of adoption. From 2017 to 2018 the number of consumer electric vehicles (EVs) sold in Canada doubled aided by government incentives and investments [1]. The significant price in purchasing an EV remains to be a major obstacle for mass adoption resulting in the continued growth in the production of GHGs and burdening the Canadian energy market.

TRANSPORTATION SECTOR GHG EMISSIONS FOR CANADA, 2000-2017
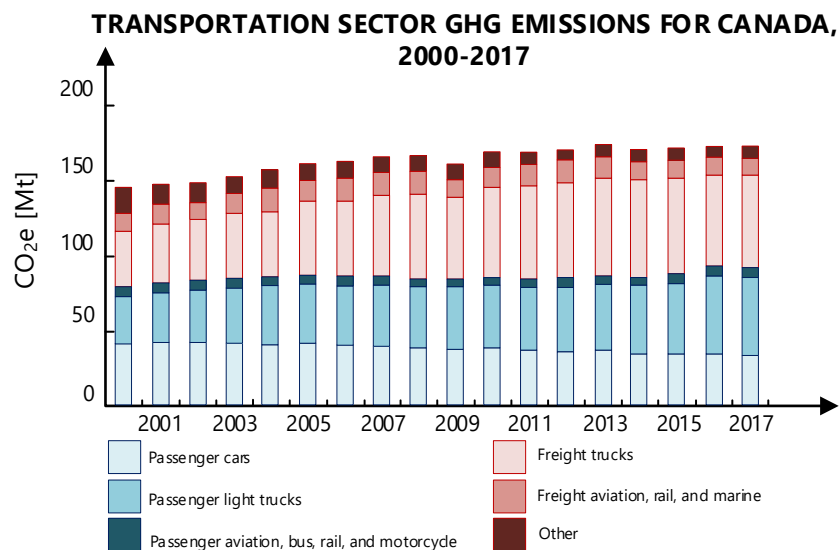
Fig. 1.1: Transportation emissions for Canada from 2000 to 2017 [1].

Currently, the most common electric drives used as a means of propulsion consist of permanent magnet synchronous machines (PMSM) and induction machines (IM). PMSMs have high-energy permanent magnet (PM) material to provide an independent source of magnetic flux, which results in high torque density and high efficiency for the operating speed range [2]. However, PMs in PMSMs use high-energy rare-earth materials such as neodymium and dysprosium,

which are sensitive to temperature and their performance decreases with an increase in temperature. The PMs begin to demagnetize at higher temperatures which can result in the lower-torque production. The PMs are also a significant portion of the total cost of PMSM, while the PMs only contribute an insignificant percentage of the PMSM weight and volume. Furthermore, according to the US department of Energy, rare-earth elements such as neodymium and dysprosium are considered as a critical material [3]. With countries such as China having 37% of the global reserves and producing 60% of the documented global supply in 2019 and 2020, the price of rare-earth is heavily monopolized and can fluctuate due to a magnitude of reasons such as: geopolitics, conflicts, demand, natural disasters, etc. [5]. The mining and transportation of rare-earth also has a significant impact on the environment, human health, and mining of rare-earth produces harmful mining waste [6]. With the current electric drive demand growing especially for traction applications, high-energy rare-earth prices can be expected to increase and further supply-chain/political issues can result in lack of supply altogether.

Price of Rare Earth Material Since 2009
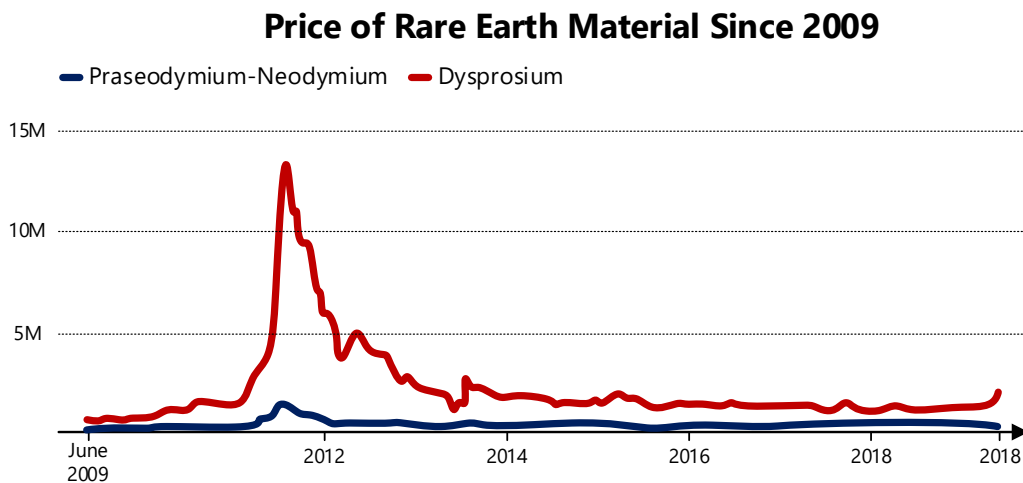
Fig. 1.2: Price of rare earth material since 2009 [4].

3

IMs are one of the most widely used motor types in all sectors. IMs contain conductors within the rotor that must be separately excited to generate a magnetic field [7]. IMs are unique due to their low-cost and self-starting nature which is usually not found in other electric drives. The self-stating capability allows for the IM to operate directly from a 3-phase supply, without the need for complex control systems. IMs cost less than PMSMs, as there is no need for high-energy PMs to provide a rotor magnetic field. At high-speeds or high-torque requirements, the IM rotor copper losses can become significant and thermal management of the rotor windings can become problematic.

Switched Reluctance Machines (SRM) are an excellent alternative to PMSMs and IMs as they can address the issues that the two conventional electric drives face. SRMs are low-cost to manufacture, facilitate simple construction, and are composed of a robust structure. SRMs do not need any high-energy PMs within their rotor to generate a separate rotor magnetic field. This allows for the SRM to have a significantly lower price. Producing motors with lower cost and non-critical material is vital to the manufacturer and consumer as it allows for higher EV penetration into the commercial and consumer sector, contributing to the reduction of GHGs in line with the governmental projections. Additionally, by not utilizing PMs, the material footprint and environmental footprint is also greatly reduced.

SRMs are not sensitive to high temperatures as there are no PMs in the rotor, allowing for reliable high-speed operation without having to consider the effects of PM demagnetization resulting lower torque production [8]. The thermal performance of an SRM is usually limited by magnetic wire insulation or an infill

epoxy used to suspend the magnetic wires in certain applications, but these thermal breakdown temperatures are greater the ones which limit the PM performance in a PMSM.

Due to the lack of PMs in the rotor of an SRM, the low-speed efficiency is inferior to the PMSMs but at medium to higher-speeds the SRM delivers equivalent or higher efficiency when compared to a PMSM, with the added benefits relating to material volatility, cost, and environmental footprint discussed previously. SRMs are also suited for high-speed operation as flux weakening occurs naturally, unlike the PMSM. SRMs are naturally fault tolerant due to its electrically isolated phases. This allows the SRM to continue operation with limited torque production capability if a fault occurs in a phase.

The electrically isolated phases are due to the double salient nature of an SRM and result in independent phase torque production which causes in higher total torque ripple than the PMSM and IM. The torque ripple of an SRM can be reduced by optimizing the motor geometry and developing control schemes by shaping the phase current. Acoustic noise and vibrations are also major drawbacks for an SRM. The acoustic noise and vibrations are due to the double salient nature of the rotor that facilitates in the flux passing in the radial direction which results in significant radial forces to act on the stator geometry. The acoustic noise and vibration in an SRM can be reduced greatly by optimizing the motor geometry, construction, and current control. SRMs also use a unique converter topology known as an asymmetric bridge converter. In an asymmetric bridge converter, there is no shoot-through fault condition that is observed in most PMSM and IM

converter topologies. Due to these main challenges presented, SRMs had a low market share in electric drive applications, historically. In the next section the contribution of this thesis will be discussed, and the effort made to help increase the SRMs market share by targeting a specific challenge which the machine faces.

1.2 – Research in SRM Control

There is significant work done to control SRMs in motoring mode and improve the select performance objectives. Most of the work done is for motoring mode specific objectives such as: maximizing torque production, minimizing torque ripple, and minimizing phase current.

In [8], offline torque sharing functions are proposed to minimize torque ripple for a wide speed range. In addition to the primary objective, two secondary objectives that minimize copper loss and rate of change in current are used to improve the motoring performance using Tikhonov factor to determine which performance objective to pursue. In [9], torque sharing functions are developed to reduce the torque ripple by considering the commutation phase current dynamics and a single weighted parameter. The optimization was carried out for a wide speed range while considering optimal current tracking. References [10] and [11] presents an adaptive control scheme for an SRM to control the turn-off conduction angle using a finite control set model predictive control to reduce the negative torque production in motoring mode reducing torque ripple and minimizing copper losses at high-speed operation. A new torque sharing function method is presented in [12] to reduce torque ripple in SRMs. A novel method of generating phase current references which considers the current dynamics limitations are used to reduce the

current tracking error for various speeds while maintaining average torque performance.

In [13], the firefly algorithm is used to optimize the instantaneous torque performance of an SRM. The algorithm aims to reduce the torque ripple and torque dynamic response of the motor when using a proportional-integral controller. In [14], a modified hybrid whale optimization algorithm is used to reduce the torque ripple for a wide speed range. The optimization considers the limitation of the controller and phase current commutation and improves the desired dynamic performance by optimizing conduction angles. Literature [15] presents an adaptive particle swarm optimization algorithm to enhance the speed regulation dynamic performance of an SRM when controlled using a PI controller. The dynamic response is improved using the algorithm.

In [16], an offline optimization is developed to maximize average torque and minimize average torque ripple by finding the minimum of single-variable function on fixed interval. The optimization was done for a wide current reference and speed range by selecting the conduction angles. Reference [17] presents a sliding mode controller for an SRM to control the speed, and torque sharing functions are used to optimize the torque characteristics. Two objectives of average torque and torque ripple are optimized. In [18], a multi-objective optimization is used to control the turn-off conduction angle using the torque ripple and copper loss objectives. The proposed optimization does not require the motor parameters and the turn-on angle is selected based on the turn-off angle.

In [19], multi-objective optimization is used to improve three objectives using an individual weighted method for motoring mode: average torque, torque ripple, and copper loss. The conduction angles are optimized to be used by a conduction angle control scheme and a hysteresis controller. In [20], the conduction angles are selected using a teaching and learning based optimization technique and Grey Wolf optimization to maximize average torque and minimize torque ripple RMS. The turn-on and off angles are used for conduction angle control with a hysteresis controller. A pattern search optimization algorithm is used to determine conduction angles in [21] to be used in an online torque sharing function. The main objectives are to minimize torque ripple, phase current, and calculation times.

In [22], a torque sharing based optimization is presented to extend the torque-speed range of an SRM. The optimizer selects the turn-on and overlap conduction angles to maintain an acceptable average torque while minimizing phase current. An ant colony optimization is used to determine the conduction angles. In [23], conduction angles are selected using an optimization which maximizes the torque per ampere objective to improve the motor efficiency. The optimization is accomplished using a direct instantaneous torque control which allows for simple implementation. In [24], an elitist-mutated multi-objective particle swarm optimization is used to select conduction angle to minimize torque ripple while maximize torque average.

In [25], an artificial intelligence-based control is used to minimize the torque ripple by selecting conduction angles based on the operating speed. The optimization specifically uses the turn-off conduction angle to change the behaviour

of the demagnetising phase current. In [26], a data driven optimization is developed to control torque sharing function behaviour to minimize torque ripple. The rate of change in phase current is observed to construct optimization constraints.

1.3 – Thesis Contribution

The SRM has been a point of interest in the research and academic community, particularly in the topic of developing control schemes to improve performance in motoring mode by using optimization techniques. Some control strategies: such as single pulse control, conduction angle control, and torque sharing functions have been optimized to improve motoring performance such as maximizing average torque production while minimizing torque ripple and reducing losses for a wide-speed range of operation.

As any conventional electric motor, the SRM is capable of four-quadrant operation and the work done to improve the motoring performance does not directly translate to the generating mode in most cases. As generating mode requirements can be different when compared to motoring mode and little work has been done in literature with regards to this subject. The goal of this thesis is to explore an SRM in generating mode and compare it to motoring mode using conduction angle control at different operating conditions. The performance was compared at different speeds, current references, and various conduction interval behavior. Using the motoring and generating comparisons, key optimization objectives are established to improve the performance of the SRM in generating mode specifically. The new generating specific optimization objectives are compared to conventional optimization objectives to show the improvement in power supplied

to the source for the same or smaller prime mover torque. An experimental dynamometer setup consisting of an SRM and IM is constructed to validate the proposed optimization objectives experimentally.

1.4 – Thesis Overview

This thesis presents optimization objectives to specifically improve the generating mode of operation by maximizing the amount source current returned to the source while minimizing torque.

In chapter 2, the fundamental electromagnetic principles of a switched reluctance machine are presented. The concept of co-energy is outlined, and the non-linear characteristics of the motor are introduced. The motor operational behaviour is visualized using static characteristics and losses of an SRM are broken down. The unique asymmetric bridge convertor topology is shown along with all three modes of operation used in hard and soft-switching to control the phase current of an SRM.

Chapter 3 introduces generating mode of operation for the SRM, and the effect of hard and soft-switching are shown for different rotor speeds and current references. The motoring conduction angles are shifted or reflected along the aligned rotor position to obtain generating conduction angles. The generating conduction angles are used to compare the torque and phase current behaviour between the two modes of operation. Current control conditions are developed which can operate an SRM in generating mode using soft-switching, as motoring mode soft-switching current control conditions are not able to control the phase current. The proposed soft-switching conditions are compared to the hard-switching

current control conditions in generating mode to determine if the proposed conditions can operate for various rotor speeds.

In chapter 4, generating specific optimization objectives are developed using an exhaustive conduction angle search for a specific rotor speed and current reference. The average torque, torque ripple RMS, and source current are determined for all turn-on and off combinations. The source current and torque objectives are combined which results in the amount of source current returned to the supply being maximized while minimizing the prime mover torque. The second objective is to reduce the torque ripple. The proposed optimizer also allows for delayed conduction angles. However, the optimizer did not utilize this range as it results in lower torque production and source current. The new optimization objectives also produce a much smaller Pareto front resulting in working conditions with less variation in improved performance.

In chapter 5, an experimental setup capable of four-quadrant operation is constructed from the ground up to validate the generating specific optimization objectives. The static characteristics of a 3-phase 12/8 SRM are determined using the voltage pulse method and the rising phase current profile. The experimental and simulation results are compared to ensure the conduction angles selected using the simulation-based optimizer yield similar performance for the experimental setup. The generating specific optimization objectives of $\max|I_{source,avg}/T_{avg}|$ and $\min(\Delta T_{RMS})$ are then compared to the original objectives $\max|T_{avg}|$ and $\min(\Delta T_{RMS})$ at different DC-link voltages, rotor speeds, and current references. In all cases explored, the $\max|I_{source,avg}/T_{avg}|$ objective improved greatly due to the

amount of prime mover torque being minimized while improving or maintaining the amount of source current returned to the supply. The proposed optimization objective also reduces the phase RMS current for all operating conditions, which leads to less copper loss.

In chapter 6, the conclusions are presented for the thesis and future work is proposed.

Chapter 2. Fundamentals of Switched Reluctance Machines

This chapter provides the motor topology, electromagnetic fundamentals, modeling techniques, and the converter used to drive the switched reluctance machine.

2.1 – Electromagnetic Principles

Like all motor topologies, the SRM operates based on the fundamental electromagnetic principles to convert electrical energy into mechanical energy, and vice-versa. The SRM has a salient rotor and stator with the rotor containing no magnets or windings for separate excitation. Only the SRM stator has winding around the stator poles. Both the rotor and stator are made of electric steel laminations. In Fig. 2.1, the cross section of an SRM is shown with the rotor, stator, and the coils placed between the stator poles.
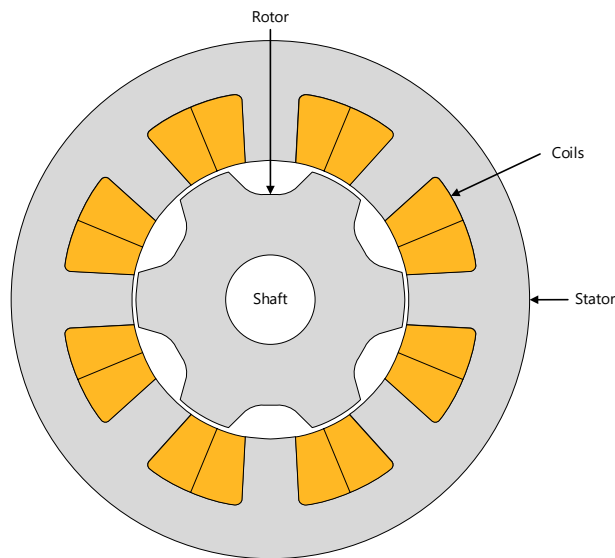
Fig. 2.1: SRM cross section showing rotor, stator, and coils.

When an external magnetic field is introduced, the magnetic domains in the ferromagnetic core align with the external magnetic field. The external field is known as the magnetic field intensity and the internal field is known as magnetic flux density. The relation between internal and external magnetic fields is defined by:

$$\vec{B} = \mu_0 \mu_r \vec{H} \tag{2.1}$$

where μ_r is the relative permeability of the magnetic material, $\vec{H}$ is the magnetic field intensity [A/m]. The relation between magnetic field intensity and magnetic flux density is not a linear relation as the increase in magnetic field intensity does not yield a continuously increasing magnetic flux density. This is defined as saturation. As a result, the relative permeability is not constant in relation to the magnetic field intensity, shown in Fig. 2.2.
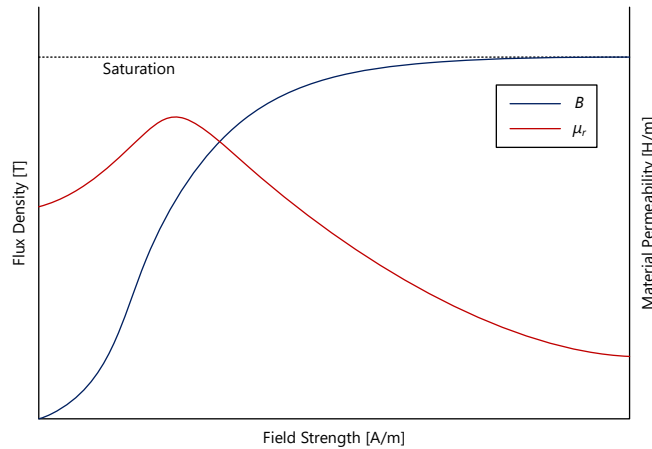
Fig. 2.2: Typical B-H and μ-H relationship.

When two opposing coil windings around the stator poles are excited with constant current, the rotor tends come into alignment to reduce the magnetic reluctance. Since the rotor rotates along the shaft, it experiences forces in the radial

and tangential directions. These directional forces can be quantified by the Maxwell stress tensors:

$$T_r = \frac{1}{2\mu_0}(B_r^2 - B_t^2) \tag{2.2}$$

$$T_t = \frac{1}{\mu_0}(B_r B_t) \tag{2.3}$$

where T_r is the radial force density in N/m^2, T_t is the tangential force density, B_r is the radial magnetic flux density, and B_t is the tangential magnetic flux density. The radial force density is responsible for acoustic noise and vibration partially due to the deformation of the stator. The tangential force density creates the torque production.

2.1.1 – Inductance and Reluctance

Inductance and reluctance are important principles when it comes to understanding the operation of a switched reluctance machine. When an SRM's ferromagnetic rotor pole comes into alignment relative to the ferromagnetic stator pole, the rotor pole experiences an external magnetic field generated from the stator pole and winding. This causes the ferromagnetic rotor to be magnetized and the rotor poles being attracted to the stator poles, Fig. 2.3.
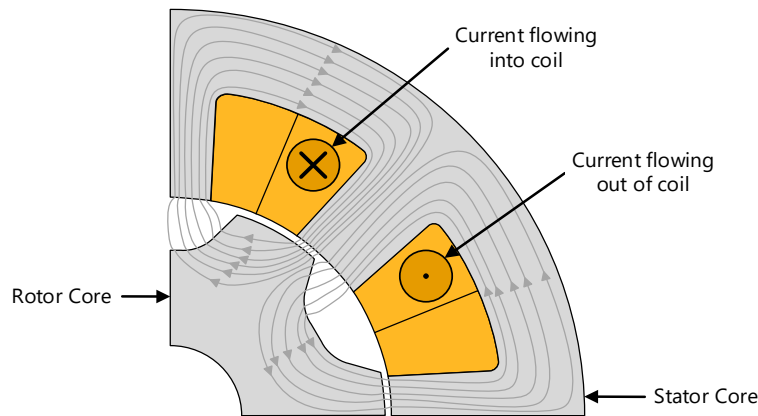
Fig. 2.3: A typical magnetic field propagation within SRM stator and rotor geometry.

The change in magnetic field configuration is due to the change in reluctance of the magnetic circuit. As the rotor pole comes into alignment with the stator pole, the reluctance of the magnetic circuit reduces. This is due the permeability of air being close to unity, and when the rotor pole moves towards the stator pole, the effective airgap reduces and the effective permeability of the magnetic circuit increases. The magnetic reluctance is the smallest when the rotor and stator poles are aligned, as the air gap is at a minimum. Any rotor position prior to or post alignment results in higher reluctance due to the double salient nature of the SRM. With the stator pole excited with a constant current, the rotor and stator will stay in alignment. This is where the 'reluctance' term comes from when classifying the switched reluctance machine.

Inductance is classified by the excited magnetic circuit opposing the change of current in an electrical circuit. In Fig. 2.4, a voltage source, a wire loop with a single turn, and a resistor representing the wire loop lumped resistance is shown.

The voltage expression of the equivalent circuit of a wire loop connected to a voltage source can be expressed as:

$$v = Ri + N\frac{d\varphi}{dt}Ri + \frac{d(N\varphi)}{dt} = Ri + N\frac{d\lambda}{dt}. \tag{2.4}$$

The number of turns of the wire loop can be denoted by N, and λ is the flux linkage. The magnetic flux must also pass through N number of enclosed surfaces. This results in the electromotive force becoming N times larger. The flux linkage is the total magnetic flux linking the electrical circuit. This relation is also used to describe a single phase of an SRM.
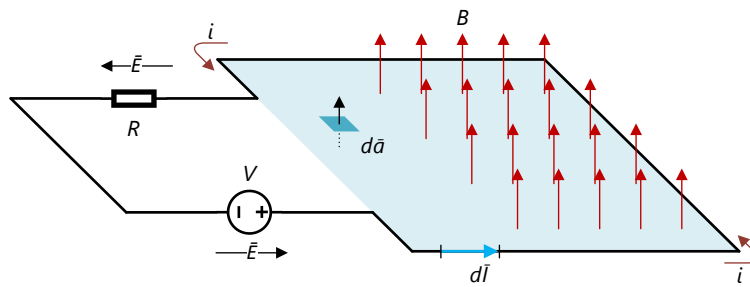
Fig. 2.4: A wire loop equivalent circuit connected to a voltage source.

If a current carrying conductor with N turns is coiled around a ferromagnetic core material, an external magnetic field will be generated and circulate within the closed loop of the core. Fig. 2.5 shows a magnetic flux loop l_c, when the coil wound around a ferromagnetic core is excited with current.
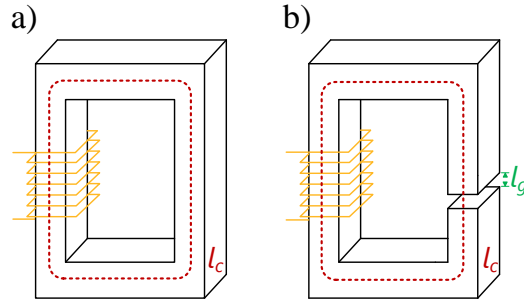
Fig. 2.5: Simple coil around a solid core loop (a) without air gap (b) with airgap.

Reluctance is defined as the opposition of the magnetic flux within a magnetic circuit, it is the equivalent of resistance in an electrical circuit. Reluctance depends on magnetic circuit closed-loop length, permeability, and core cross-section. Reluctance of a magnetic circuit is expressed as:

$$\mathcal{R} = \frac{l_c}{\mu_r \mu_0 A_c}. \tag{2.5}$$

Reluctance and magnetic flux can be expressed as:

$$\mathcal{R}\varphi = Ni. \tag{2.6}$$

Since magnetic reluctance can be compared to resistance in an electrical circuit the entire magnetic circuit can be expressed as an electrical circuit equivalent. The flux component can be compared to a voltage source in an electrical circuit. Fig. 2.6 shows the equivalent electrical circuit for a magnetic system.

A ferromagnetic material has much higher permeability than air. This results in the magnetic reluctance of the two physical regions to be different, as air is defined by permeability of free space μ_0. The flux path relation of the two region is expressed as:

$$H_g l_g + H_c l_c = Ni \tag{2.7}$$

where H_c is the magnetic field intensity of the solid ferromagnetic core and H_g is

the magnetic field intensity of the airgap.
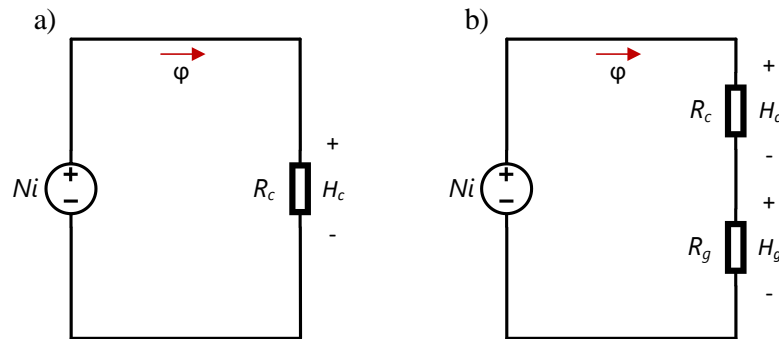
Fig. 2.6: Electrical circuit equivalent for a magnetic system (a) without airgap (b) with airgap.

2.1.2 – Magnetic Stored Energy and Co-Energy

A simple magnetic circuit consists of a solid ferromagnetic core with a coil,

an airgap, and has no mechanically moving parts. The losses experienced in such a

system are electrical, which consists of the winding resistance, and the remaining

electrical energy is stored in the magnetic circuit. The energy balance of such a

system can be calculated as:

$$v = Ri + \frac{d\lambda}{dt} \rightarrow vi = Ri^2 + i\frac{d\lambda}{dt} \rightarrow (vi - Ri^2)dt = id\lambda \qquad (2.8)$$

where $(vi - Ri^2)dt$ represents the electrical losses due to the coil resistance, and

$id\lambda$ represents the stored magnetic field. In Fig. 2.7(a), a linear relationship between

flux linkage and current is shown and is due to constant material permeability. The

upper half of the flux linkage and current relation represents the stored energy in

the magnetic field.
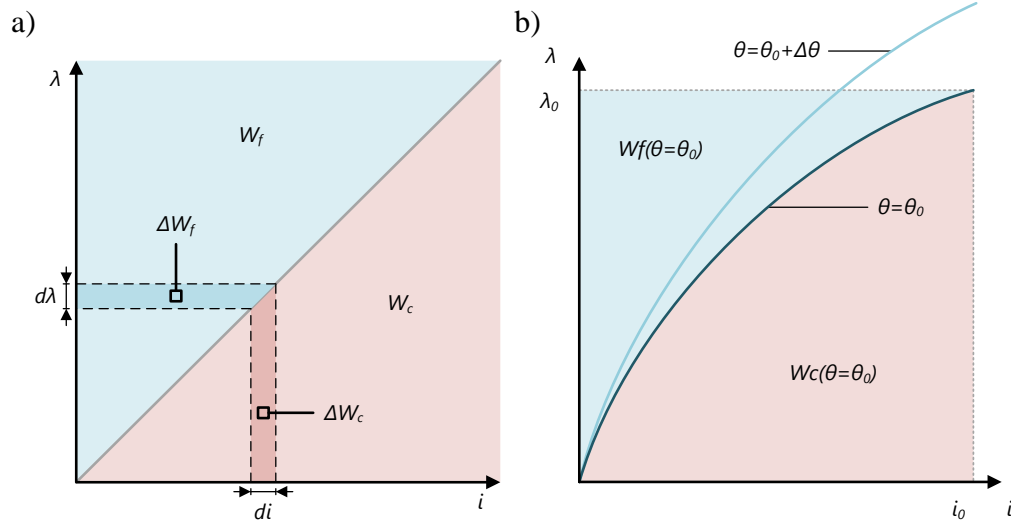
Fig. 2.7: Flux linkage in relation to current for (a) linear magnetic circuit (b) non-linear magnetic circuit.

For a linear magnetic circuit, the magnetic energy and co-energy areas are equal [27]. Co-energy is a non-physical quantity, but it is used in physical systems to quantify theoretical analysis [28]. Physical systems that produce torque and magnetic forces such as rotating machines do not have a linear flux linkage and current relation as shown in Fig. 2.7(b).

If in the SRM the losses are neglected all the supplied electrical energy would be converted into one of two components: magnetic and mechanical energy:

$$eidt = dW_f + T_e d\theta \tag{2.9}$$

where T_e is the electromagnetic torque, and θ is the mechanical rotor angle [29]. By substituting the induced voltage relation $e = d\lambda/dt$ into (2.9), the magnetic energy will be calculated as $id\lambda$ if the rotor position in Fig. 2.8 is fixed ($d\theta = 0$):

$$id\lambda = dW_f + T_e d\theta \rightarrow dW_f = id\lambda - T_e d\theta \tag{2.10}$$

20
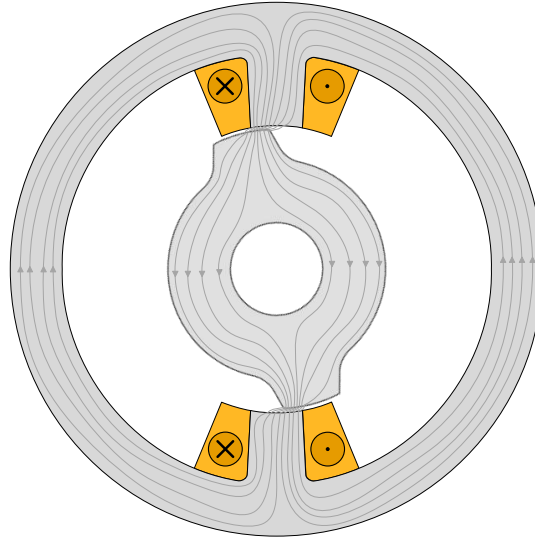
Fig. 2.8: Single phase SRM with flux line and small unalignment.

For a single phase SRM shown in Fig. 2.8, the flux-linkage and current relation is non-linear due the ferromagnetic materials comprising of nonlinear magnetization properties. The rotor position affects the flux linkage and current relation. The magnetic energy is dependent on the rotor position:

$$dW_f(\lambda, \theta) = \frac{\partial W_f}{\partial \lambda} d\lambda \Big|_{\theta=const} + \frac{\partial W_f}{\partial \theta} d\theta \Big|_{\lambda=const}. \qquad (2.11)$$

In which, a constant rotor position will result in the single phase SRM to considered as a simple magnetic circuit with a fixed airgap. By combining relations (2.10) and (2.11), the following current and electromagnetic relations can be written in terms of magnetic energy relative to rotor position:

$$i = \frac{\partial W_f}{\partial \lambda} \Big|_{\theta=const} \text{ and } T_e = -\frac{\partial W_f}{\partial \theta} \Big|_{\lambda=const}. \qquad (2.12)$$

The co-energy components can be determined by subtracting the magnetic energy from the total energy:

$$W_c = i\lambda - W_f(\lambda, \theta) \qquad (2.13)$$

21

By taking the derivative of (2.12) and (2.13), then substituting (2.9), co-energy is expressed as:

$$d(W_c) = d(i\lambda) - dW_f(\lambda, \theta) \rightarrow dW_c = id\lambda + T_e d\theta \qquad (2.14)$$

$$\lambda = \left.\frac{\partial W_c}{\partial i}\right|_{\theta=const} \text{ and } T_e = \left.\frac{\partial W_c}{\partial \theta}\right|_{i=const}.$$

As the SRM has a nonlinear current and flux linkage relationship, it is best for the motor to operate within the saturation region to reduce the magnetic energy component and increase the co-energy and, hence, electromagnetic torque. This results in the use of the power electrotonic with lower volt-ampere requirements.

2.1.3 – Losses in a Switched Reluctance Machine

In an SRM, three main losses usually dominate: electrical copper losses due to the phase windings, core losses due to the iron core laminations, and mechanical losses due to the rotation of the rotor. These losses result in some of the input energy not being converted into mechanical energy entirely and being dissipated as heat. Hence, the efficiency of a system is defined as:

$$\eta = \frac{P_{in} - P_{loss}}{P_{in}} \times 100\% \qquad (2.15)$$

where P_{in} is the input power of a system, and P_{loss} is the total power loss.

For an SRM, the copper losses occur in the stator windings used to create a magnetic field and is usually the largest contributor to power loss. Copper loss can be expresses as:

$$P_{cu} = VI = (IR)I = I^2R \qquad (2.16)$$

The resistance is a function of resistivity of the conducting material, and the length, and surface area of the conductor. The resistivity of the material is also proportional to temperature.

At higher frequencies, the current distribution within the conductor is not uniform, and most of the electron density occurs at the outer radius of the conductor. The tendency of the electrons to travel along the outer edges of the conductor increases as the frequency of the current increases. Skin depth can be expressed with the following relation:

$$\delta = \frac{1}{\sqrt{\pi \sigma \mu f}} \tag{2.17}$$

where σ is the conductivity of the material, μ is the permeability of the conductor material, and f is the frequency. From the skin depth relation (2.17), it can be observed that as the frequency increases the skin depth reduces. A reduction in skin depth results in larger losses due to the smaller effective cross-section in which the AC current can traverse through the conductor. The skin effect can be reduced in an AC system by utilizing stranded wires provides a smaller conductor cross-section area.

The stator and rotor of an SRM are made of a magnetic material with a finite conductivity which introduce core losses. Eddy currents will circulate if the magnetic core experiences a time varying magnetic field, shown in Fig. 2.9.
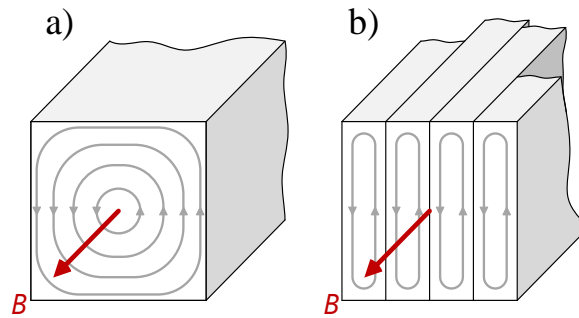
Fig. 2.9: Eddy current in (a) solid core (b) laminated core.

In an SRM, the rotor and stator core materials experience a time varying magnetic field which results in eddy current losses. To reduce the effect of eddy current losses the core material of the SRM is laminated. These laminations are electrically isolated from one another and are stacked to increase the resistance of the core material to reduce the magnitude of eddy current.

Hysteresis loss is due to the energy expended when dipoles change their alignment. In Fig. 2.10, the hysteresis loss loop is shown for ferromagnetic materials. Hysteresis losses are experienced by core material that are magnetized and demagnetized with the field strength changing. The magnetic flux increases when a positive field is applied. However, when the magnetic field is reduced the core material does not demagnetize entirely. To further demagnetize the material, a negative field direction must be applied. This results in an area within the hysteresis loop. This is the energy used to orient the domains in a ferromagnetic material. It is always present when working with time varying magnetic fields, and depends on the material properties and the frequency of the system.

The mechanical losses in an SRM are mainly due to friction and windage. Frictional loses are present when two materials contact one an another with

different relatively velocities and result in a resistance to one another's relative motion. These losses are dissipated as heat and are dependent on the system's relative velocity and static/dynamic friction coefficients. In an SRM, the bearings suspending the rotor which results in frictional losses to be reduced. Windage losses are due to air resistance and are a form of friction as well. Since the rotor in SRM has salient poles, there are windage losses present. Windage losses are dependent on the rotor speed, but also rely on the rotor pole height and rotor diameter.
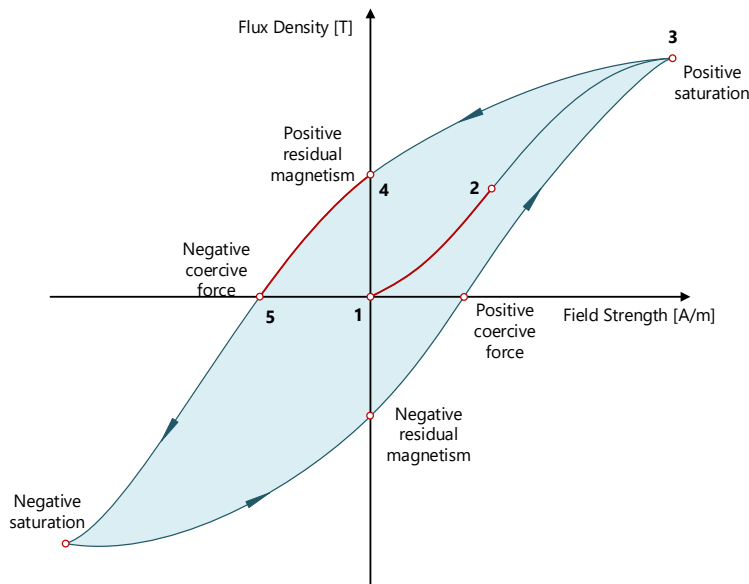
Fig. 2.10: Hysteresis loop diagram.

2.1.4 – Electrical Equivalent Circuit

Like any other electrical machine, the SRM can also be represented by an equivalent circuit. The voltage relation (2.18) can be used to express the SRM equivalent circuit:

$$v = iR + \frac{d\lambda}{dt} \tag{2.18}$$

where v is the terminal voltage across a phase winding, i is the phase current, and λ is the phase flux linkage. In an SRM, the phase inductance depends on the rotor position. Hence, the flux linkage is also dependent on the position of the rotor and is expressed by:

$$\lambda = L(\theta)i. \tag{2.19}$$

The flux linkage equation (2.19) is substituted into the phase voltage expression in (2.20) to obtain the relationship:

$$V = iR + L(\theta)\frac{di}{dt} + i\frac{dL(\theta)}{d\theta}\omega. \tag{2.20}$$

Rotational speed ω and back-emf ε can be represented by equations (2.21) and (2.22). SRM back-emf is zero if there is no phase current, i. In Fig. 2.11, the SRM general equation is shown for a single phase as an electrical equivalent circuit.

$$\omega = \frac{d\theta}{dt} \tag{2.21}$$

$$\epsilon = i\frac{dL(\theta)}{d\theta}\omega \tag{2.22}$$
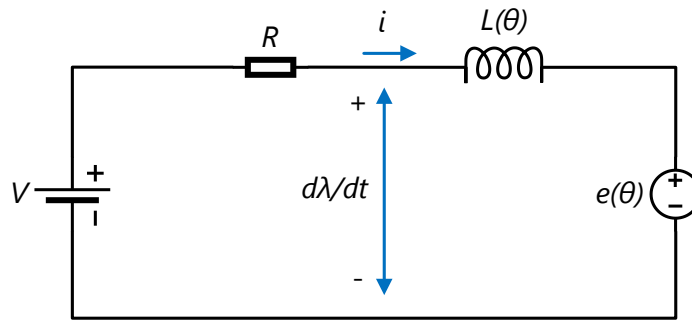
Fig. 2.11: SRM equivalent circuit.

To determine the power conversion procedure of the SRM, the voltage equivalent equation can be multiplied by the phase current on both sides:

$$iV = i^2R + iL(\theta)\frac{di}{dt} + i^2\frac{dL(\theta)}{d\theta}\omega. \tag{2.23}$$

The second right most term is expanded using the product rule and can be expressed in (2.24). The final term in the expanded equation remains, as the inductance is a time varying parameter, and the speed term is substituted using (2.21) to form (2.25).

$$iL(\theta)\frac{di}{dt} = \frac{d}{dt}\left(\frac{1}{2}L(\theta)i^2\right) - \frac{1}{2}i^2\frac{dL(\theta)}{d\theta}\frac{d\theta}{dt} \qquad (2.24)$$

$$iL(\theta)\frac{di}{dt} = \frac{d}{dt}\left(\frac{1}{2}L(\theta)i^2\right) - \frac{1}{2}i^2\frac{dL(\theta)}{d\theta}\omega \qquad (2.25)$$

To obtain the SRM power equation in its final form as shown in (2.26), (2.25) is substituted into (2.23). The total electrical input power iV is converted into three main components: electrical, magnetic, and mechanical power going from left to right on the right-hand side of (2.26). The electrical power is dissipated as copper losses in the form of heat. The magnetic power is stored in the magnetic core material of the SRM as magnetic field energy. The air gap power is used to produce torque.

$$iV = i^2R + \frac{d}{dt}\left(\frac{1}{2}L(\theta)i^2\right) + \frac{1}{2}i^2\frac{dL(\theta)}{d\theta}\omega \qquad (2.26)$$

The torque of an SRM is expressed in (2.27), which is extracted from the power equation of the SRM, and the torque expressed is from the linear operating region of the SRM. The current component is squared, showing that torque is independent of the current direction.

$$\tau = \frac{1}{2}i^2\frac{dL(\theta)}{d\theta} \qquad (2.27)$$

In (2.28), the SRM torque expression is shown for the saturation region. The torque production in the saturation region relies on the co-energy component. In an

SRM, the torque production improves when the SRM operates in the saturation region.

$$\tau = \frac{\partial W_c}{\partial \theta}\bigg|_{i=cont.} \tag{2.28}$$

2.2 – Static Characterization and Operational Principles

In an SRM, the torque and the flux-linkage are functions of the rotor position due to the salient nature of the SRM and their nonlinear dependency to the phase current magnitude. The static characterization consists of determining electromagnetic torque, phase voltage, and flux linkage of the SRM for various phase currents and rotor position. This is done by providing incremental constant current magnitudes to a single phase of an SRM with the rotor completing one electrical cycle to generate the saturation profile of the core material. This approach considers that mutual coupling is negligible in an SRM.

The flux linkage as a function of rotor position is shown in Fig. 2.12 for the 4-phase 8/6 SRM when a constant 14 A is applied to a single phase. In the unaligned position, the distance between the stator and rotor pole is the largest. As the rotor pole moves towards the stator pole, the reluctance of the magnetic circuit reduces and the phase flux linkage increases. The aligned position results in the largest flux linkage. The flux linkage profile also changes depending on the phase current magnitude. A higher phase current will incrementally increase the flux linkage profile. The flux linkage will not increase by a constant increment as the phase current increases due to the saturation of the core as shown in Fig. 2.13(a).
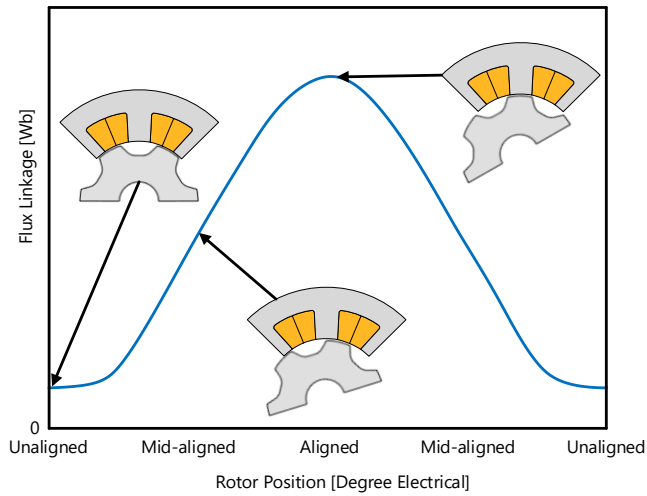
Fig. 2.12: 8/6 SRM flux linkage in relation to the rotor position.
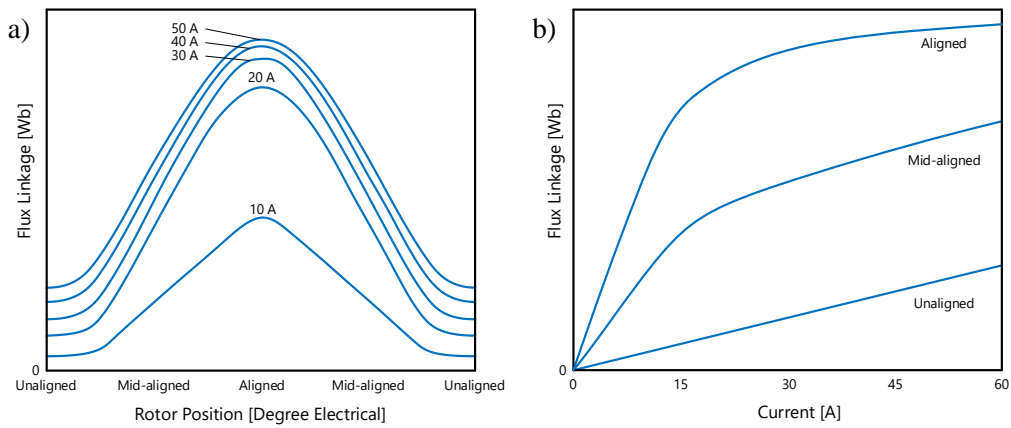
Fig. 2.13: 8/6 SRM (a) flux linkage in relation to rotor position for current increments (b) flux linkage in relation to current for different rotor positions.

The flux linkage can also be plotted as a function of the current with different rotor position increments, shown in Fig. 2.13(b). In the unaligned rotor position the flux linkage increases linearly with current due to the large airgap. At the aligned rotor position, the flux linkage is non-linear as the current increases due to the smaller airgap offering the lowest magnetic reluctance and higher effective permeability for the magnetic circuit.

In Fig. 2.14(a), the electromagnetic torque in relation to rotor position is plotted for various current increments for a single phase. The electromagnetic torque for the motoring region occurs when the flux-linkage increases with the rotor position moving towards alignment. In the generating region the flux linkages slope is negative as the rotor position moves away from alignment. The electromagnetic torque plot is created by energizing the SRM phase with only positive current, but negative torque is also present. This demonstrates that current polarity is not correlated with torque magnitude. Instead, the rotor position and flux linkage profile influence the electromagnetic torque magnitude.
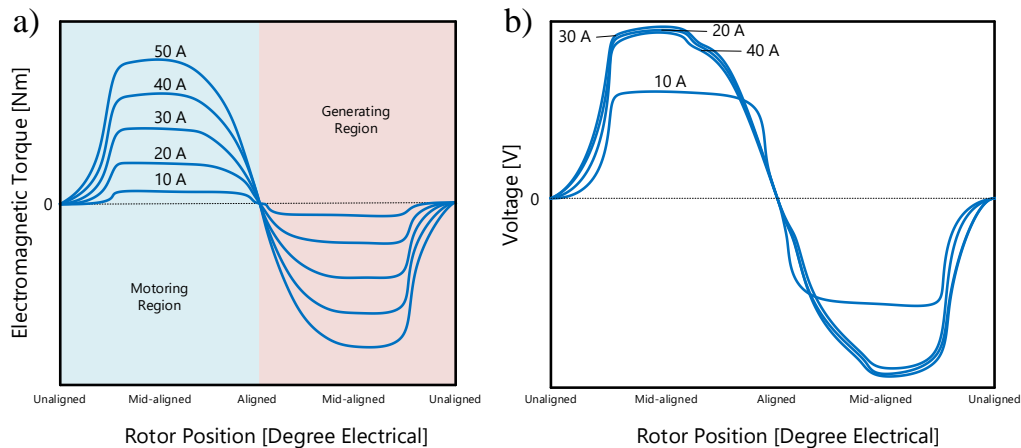
Fig. 2.14: 8/6 SRM (a) electromagnetic torque in relation to rotor position (b) phase voltage in relation to rotor position.

In Fig. 2.14(b), the static phase voltage of the SRM is also plotted by measuring the voltage across a single phase while the rotor completes one electrical cycle and constant current is provided to a single phase. The static phase voltage is also dependent on the flux-linkage profile, similar to the electromagnetic torque profile. However, the voltage is not increasing in the same way as the electromagnetic torque profile did when the supplied phase current reference

magnitude increases. In Fig. 2.14(b), after 20 A the static phase voltage remains relatively the same due to saturation. As the material saturates for the same magnitude of voltage, a higher torque magnitude is yielded, due to co-energy increasing as the material saturation increases.

2.3 – Phase Excitation

For an SRM to complete one mechanical rotation, excitation of each phase needs to occur when the flux linkage slope is positive as it corresponds with the motoring torque. To produce motoring torque, the rotor position respect to each phase is vital for the phase excitation sequence. In Fig. 2.15, a three-phase SRM's ideal inductance profiles are shown along with excitation signal and phase currents for each phase to generate mechanical rotation. In Fig. 2.15(a), the idealized flux linkage of the SRM is shown for all three phases. In Fig. 2.15(b-d) the phase excitation signals are shown for each phase. As the goal is to achieve motoring torque, it can be observed each corresponding phase is excited only when the flux linkage has a positive slope. In Fig. 2.15(e), the phase currents are shown for each phase due to the individual phase excitation. Focusing specifically on phase number 1, the excitation signal is triggered to the *ON* state at t_1, this is also known as the turn-on angle (θ_{on}). At t_3, the excitation signal for phase 1 is turned to *OFF*, this is known as the turn-off angle (θ_{off}). The excitation period occurs for phase 1 when the flux linkage has a positive slope.
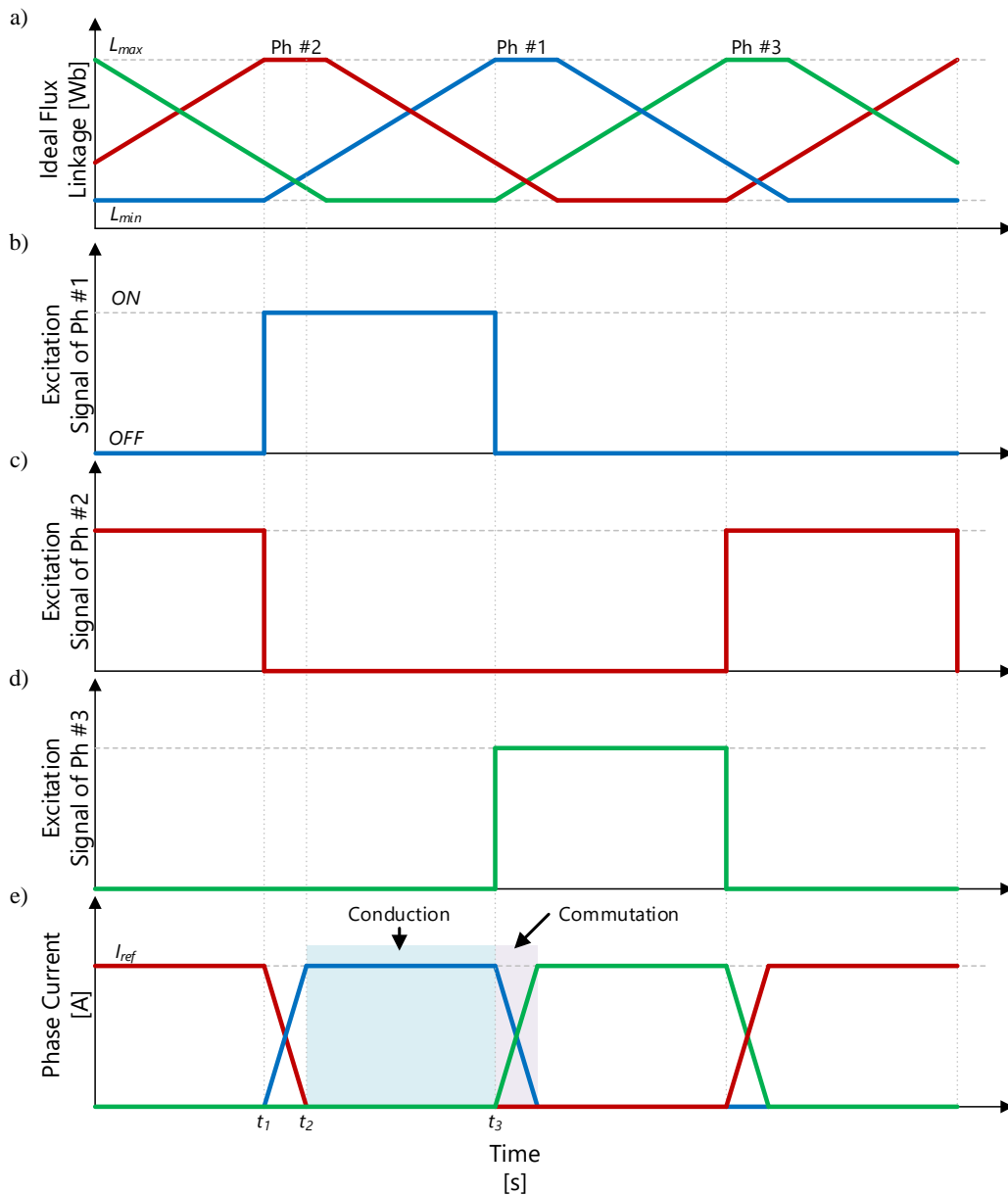
Fig. 2.15: 3-phase SRM excitation signals using ideal flux linkage.

When observing the phase currents at points t_1 and t_3 the phase current does not change instantly due to the induced voltage. For higher speed operation, to counteract the effects of the induced voltage, the turn-on and turn-off angles can be advanced to build the current in the phase. For continuous rotation, as phase 1 is being de-energized another phase should begin to be energized to provide

continuous torque. In Fig. 2.15(b) and (d), at point t_3 phase 1 is de-energized and phase 3 begins to be energized to provide current. At this point two phases are conducting for the same interval. This is referred as commutation.

2.4 – Asymmetric Bridge Converter Topology

Phase excitation is carried out by power converters. Due to SRMs unique excitation requirement a specific topology is used for excitation of individual phases. An asymmetric bridge converter shown in Fig. 2.16 is commonly used to provide phase excitation. It is composed of two legs per phase, with a diode and switch in each leg. The asymmetric bridge convertor also allows each phase to be isolated from one another allowing for operation of the motor under certain fault conditions. As discussed earlier, the SRMs torque production is independent on the phase current direction. This results in the asymmetric bridge drive (ASD) only producing unidirectional current.
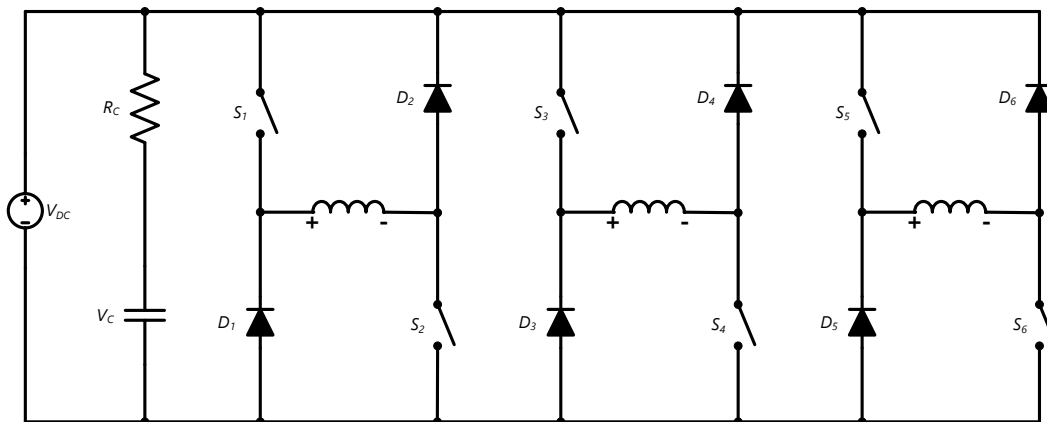
Fig. 2.16: 3-phase asymmetric bridge converter with DC-link capacitor and capacitor electric serial resistance.

There are three distinct modes in which the ASD operates and they are depicted in Fig. 2.17 for a single phase. In the first mode in Fig. 2.17(a), both

switches S_1 and S_2 are *ON*. This results in the DC-link V_{DC} being applied to the SRM phase windings, and the phase current rises and corresponds to the t_1 point in Fig. 2.15. The second operating mode is when both switches S_1 and S_2 are *OFF* and the diodes D_1 and D_2 conduct. This results in negative DC-link V_{DC} being applied across the phase voltage as the energy stored in the phase forward biases the two diodes D_1 and D_2. This mode corresponds to point t_3 in Fig. 2.15. This results in the phase current begins to reduce until it reaches zero. When the phase current reaches to zero, the diodes turn off. In the final mode of the ASDs operation, one switch is *OFF* and the other one is *ON*. In Fig. 2.17(c), switch S_1 is *OFF* and switch S_2 is *ON*. This is referred as the freewheeling mode, in which the SRM phase coil is isolated from the DC-link and the phase current decays in motoring mode due to the resistance of the phase windings, diode, and switch. All three modes are used in conjunction to control the phase current of an SRM as shown in Fig. 2.18.
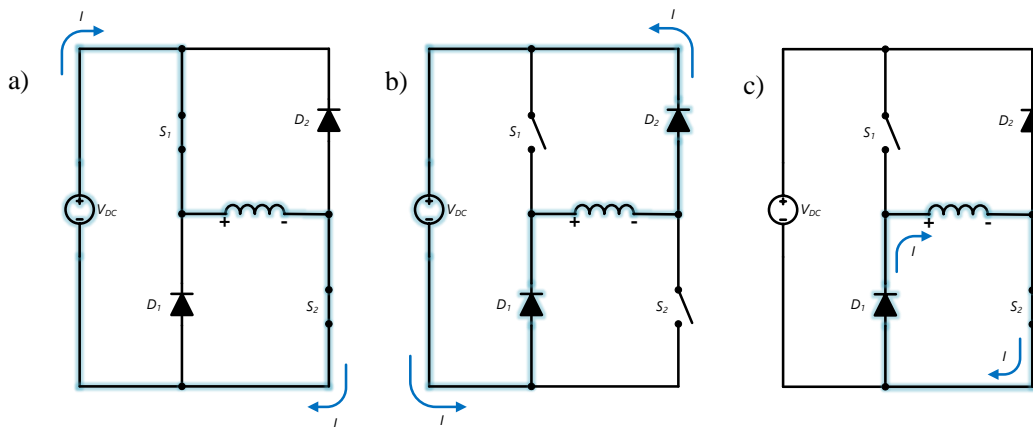
Fig. 2.17: Three modes of single phase ASD (a) Mode 1 (b) Mode 2 (c) Mode 3.
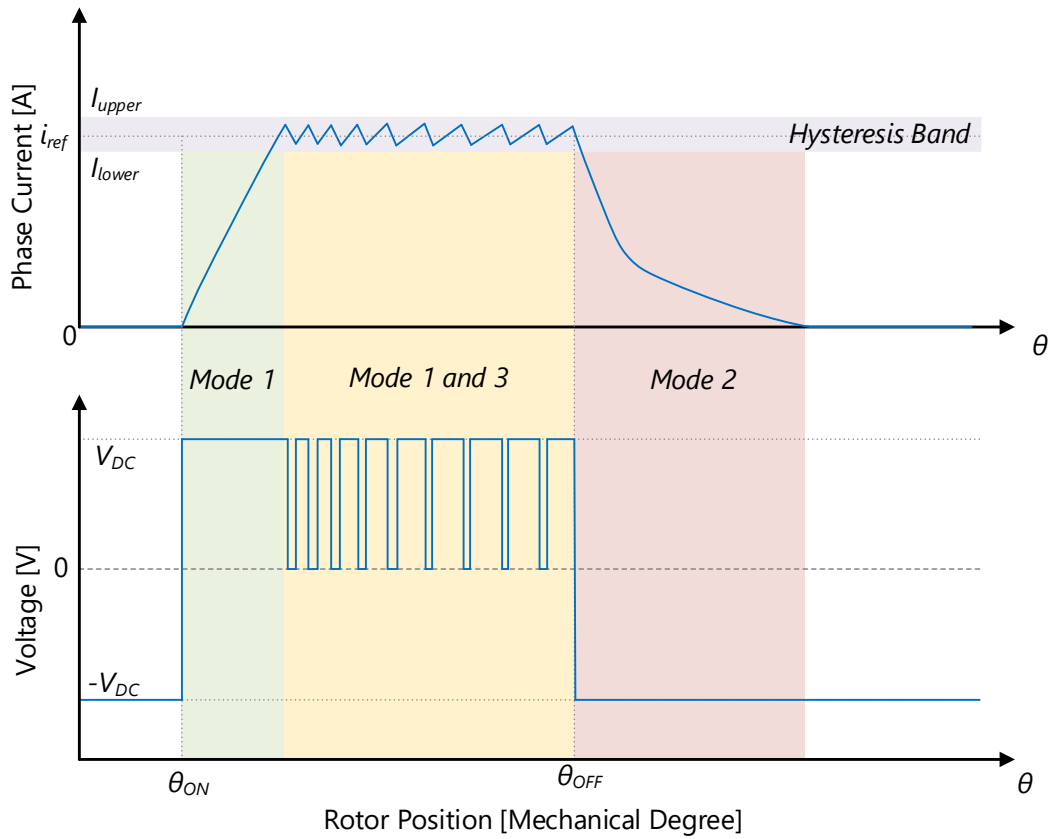
Fig. 2.18: Hysteresis control for a single phase.

2.5 – Conclusion

In this chapter the fundamental electromagnetic principles used in an SRM are discussed along with the energy conversion process. The concept of co-energy is introduced and the nonlinear characteristics of an SRM are discussed. The static characteristics of the machine are obtained in terms of flux linkage, induced voltage, and electromagnetic torque. Basic control and phase excitation sequence of an SRM are investigated to produce torque using an asymmetric bridge converter.

Chapter 3. Switched Reluctance Machines in Motoring and Generating Mode of Operation

This chapter focuses on the generating mode of operation in an SRM and outlines how different types of switching affect the mode of operation. Single pulse and current hysteresis control are also presented and compared to their equivalent generating mode counterparts.

3.1 – Operation in Generating Mode

Like other electric motor drives, the SRM can also be operated in generating mode. It can take mechanical energy from a prime mover and convert it to electrical energy. This is a vital component for a motor drive as the conversion from mechanical to electrical energy is used in generation applications such as: wind turbines, electrical generators, belt starter generators, and regenerative braking in propulsion applications. To be a key role player in transportation electrification, SRMs must be able to convert the vehicles forward kinetic energy under braking and convert it to electrical energy to be stored in the vehicle's battery. This allows the vehicle to operate far more efficiently and reduces the amount of energy lost due to heat from frictional braking.

When a phase is excited with current, rotor poles move into alignment with the excited stator pole. With the phase excited continuously the rotor stays in the aligned position, as any position before and past alignment will result in a larger magnetic reluctance due to the airgap increasing. When the rotor is aligned due to

phase excitation, an external force is required to move the rotor beyond alignment. As the external force opposes the forces exerted on the rotor pole from the magnetic field, a negative torque is applied to the prime mover drawing power from it. If the circuit is turned off at the end of the electrical cycle, the energy transferred from the prime mover to the magnetic circuit is converted into electrical energy and fed back to the power source supplying the SRM. This results in the machine behaving like a generator and is referred to as a Switched Reluctance Generator (SRG).

SRGs can convert mechanical energy into electrical energy but does so in a different way compared to machines which have an independent excitation. SRGs require phase excitation to complete the energy conversion process, during the negative slope of the inductance profile while the direction of the phase current remains the same. However, an initial phase excitation is required for magnetization of the magnetic circuit, which is drawn from the voltage supply of the SRG.

An SRM's flux-linkage, electromagnetic torque, and phase voltage profiles are shown in Fig. 3.1. Initially, the rotor is at the unaligned position. It completes one electrical cycle while rotating in the CCW direction at a constant speed and when a constant current is applied to one of the phases. To move the rotor past alignment, an external force from the prime mover needs to be applied to overcome the alignment torque. Due to the constant positive current being supplied and the rotor as it moves beyond the aligned position, the flux-linkage slope becomes negative, and the phase voltage becomes negative. The negative phase voltage implies that the source current would change its direction, and the machine generates electrical power while the phase current maintains the same polarity as in

motoring mode. Achieving this operation in practice requires proper control of the phase current in generating mode considering the flux linkage characteristics of the motor as a function of rotor position and phase current.
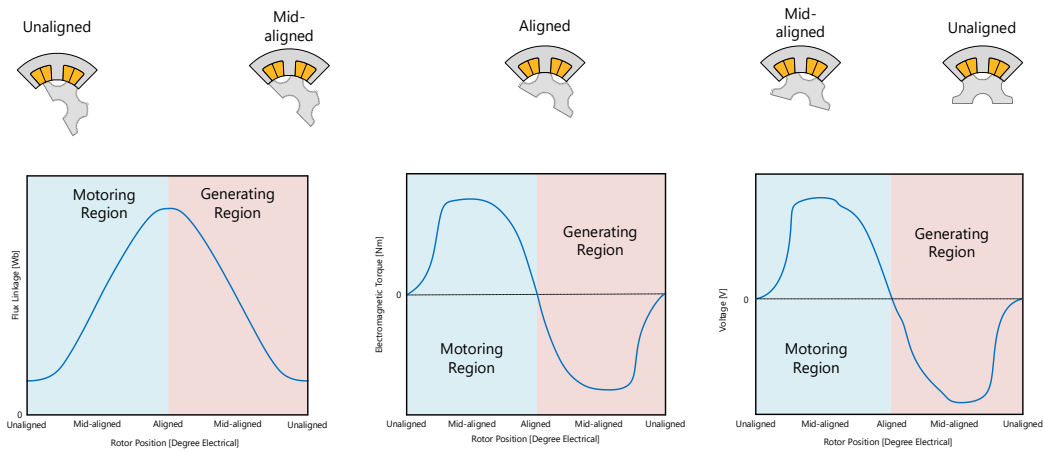
Fig. 3.1: Static characteristic profiles at different rotor positions.

3.2 – Effects of Switching

An asymmetric bridge converter is used to control the phase current of the SRM in both motoring and generating mode. The asymmetric bridge converter is capable of soft and hard-switching to control the phase current. Hard-switching involves both switches operating in conjunction to control the phase current of the SRM. Soft-switching involves the use of only one switch to control the current reference while the other switch stays in the turned off position. Both switching techniques can be used in motoring and generating mode with minor differences. In Fig. 3.2 and Fig. 3.3, both motoring and generating mode are shown for the hard and soft-switching for a single phase.

The inductance near alignment is high which results in the phase current rising much slower in generating mode when compared to motoring mode. In motor

mode, phase inductance is usually lower at the turn-on time. Similarly, in motoring

mode, during the turn-off period, the phase inductance is high resulting in the phase

current to reduce slower. In generating mode, during the turn-off period, the phase

current has a higher rate of change due to the lower phase inductance. In Fig. 3.2,

hard-switching is shown for both motoring and generating mode. The major

differences are the rise and fall in phase current during the turn-on and off periods.

When both switches are turned on, current flows from the power source to the motor

phase. In hard-switching, when both switches are turned off, $-V_{DC}$ is applied to the

motor phase. The diodes are forward biased due to the stored energy in the motor

phase resulting in the current being provided back to the supply.
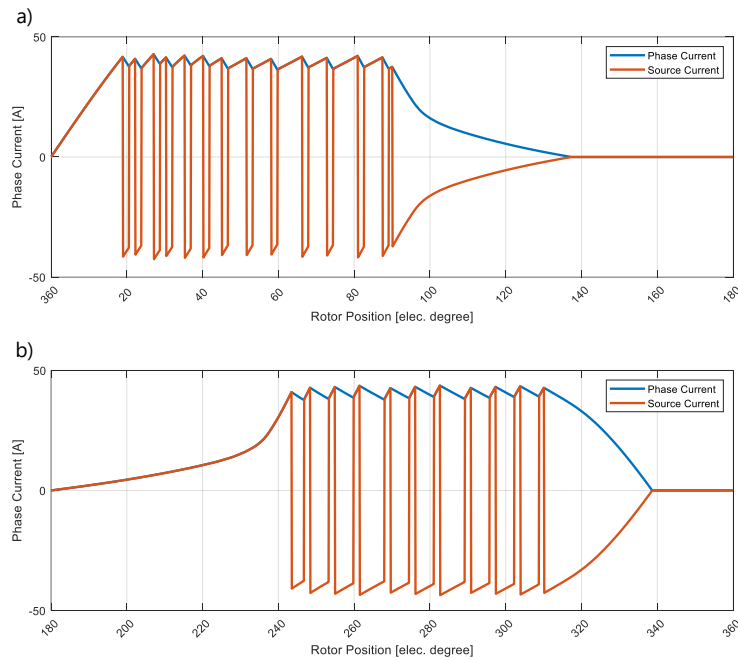
Fig. 3.2: Single phase current profiles using hard-switching in (a) motoring mode
(b) generating mode.

When the asymmetric bridge converter applies soft-switching the motoring and generating modes become drastically different from one another, as shown in Fig. 3.3. Initially, during the turn-on period, both motoring and generating modes phase currents rise, with the motoring mode phase current rising at a faster rate due to the lower phase inductance. To control the phase current to a certain reference soft-switching is applied by turning on one switch and keeping the remaining switch in the off position; hence the phase current freewheels. During the freewheeling component in motoring mode, the phase current reduces due to the energy being dissipated over the switch, diode, and the phase resistance of the machine. When compared to hard-switching, soft-switching has only one switch remaining off which results in a much slower rate of change in the phase current due to 0 V being applied as opposed to $-V_{DC}$ in hard switching.

In generating mode when soft-switching is applied, the phase current begins to rise. This is opposite of what happens in motoring mode, in which the phase current reduces during the freewheeling phase. It can be observed that during freewheeling, the phase current begins to rise at a faster rate as compared to when both switches were on and V_{DC} was applied to the motor phase during initial excitation. In generating mode, during free-wheeling period, the phase current increases because the rate-of-change of flux linkage does not oppose the current [30]. At the end of the conduction period both switches are turned off, and current is supplied back to the source.
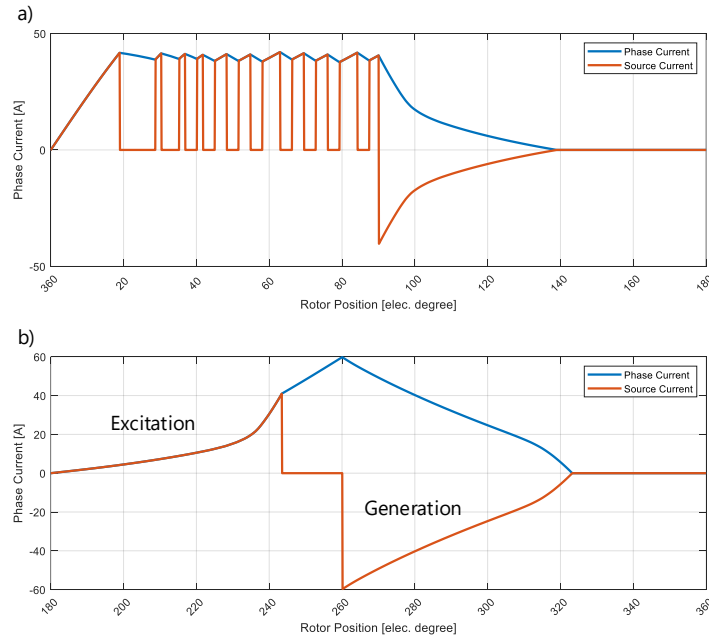
Fig. 3.3: Single phase current profiles using conventional soft-switching in (a) motoring mode (b) generating mode.

3.3 – Single Pulse Mode

One of the simplest schemes to operate an SRM is single pulse mode. In one electrical cycle the switches are turned on and off only once. This control scheme is most effective at higher speeds as the induced phase voltage become higher than the input voltage. In single pulse mode, at the beginning of the conduction period both switches in the asymmetric bridge converter are turned on, resulting in the SRG to draw power from the source and the phase current rises. Shortly after, both switches are opened, and the SRG supplies current back to the power source.

Despite single pulse mode of operation having relatively simpler current control, the conduction period can be varied to achieve different phase current profiles. When single pulse mode is utilized in generating and motoring modes, the

turn-on and turn-off periods result in the magnitude of the phase current changing.

In Fig. 3.4(a), an SRM in motoring mode using single pulse mode has the turn-on

angle varied from 0 to 20 degrees electrical, resulting the peak phase current to

change. Despite the turn-off angle occurring at 120 degrees electrical, the phase

current demagnetization occurs at different periods, because of the difference in the

peak current. An earlier turn-on angle results in a higher phase current magnitude

and a longer duration of phase demagnetization. In Fig. 3.4(b), an SRM in motoring

mode has a fixed turn-on angle and varied turn-off angle. With the turn-on angle

being fixed at 0 degree electrical, all cases have the same phase current peak

magnitude. The turn-off angle being varied from 100 to 120 degrees electrical only

results in phase demagnetization period changing. The sooner the turn-off angle the

earlier the phase demagnetized.
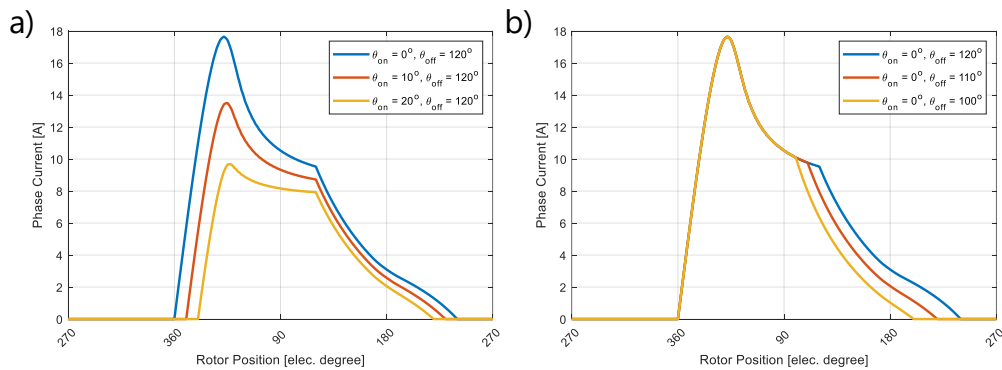
Fig. 3.4: Single pulse in motoring mode with (a) turn-on angle varied (b) turn-off angle varied.

In Fig. 3.5(a), similar analysis is shown for generating mode using single

pulse mode. The turn-on angle varies from 180 to 200 degrees electrical, and the

turn-off angle is fixed at 280 degrees electrical. The phase current magnitude

increases with the earlier turn-on angle and the phase current demagnetizes at a later

42

period despite having the same turn-off angle. In Fig. 3.5(b), an SRG with single pulse mode control has its turn-on angle fixed and the turn-off angle varied. When the turn-on angle is fixed at 180 degrees electrical and the turn-off angle is varied from 260 to 280 degrees electrical, the SRG phase current magnitude and phase current demagnetization change. A later turn-off angle results in a higher phase current magnitude and, hence, longer period for the phase current to demagnetize.
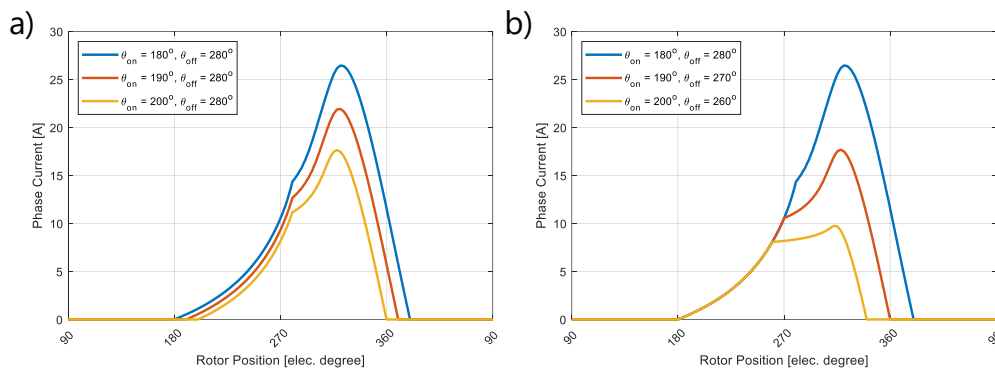
Fig. 3.5: Single pulse in generating mode with (a) turn-on angle varied (b) turn-off angle varied.

In generating mode using single pulse control, when the turn-off angle is varied the phase current peak magnitude increases unlike the motoring mode. This occurs in generating mode due to the induced voltage not opposing the voltage source polarity. The phase current continues to rise in generating mode as it is assisted by the induced voltage polarity. In generating mode both the turn-on and off angles vary the phase current magnitude, which presents challenges in control of the SRG, specially at higher speeds. When using single pulse mode in generating mode, especially for generation to an isolated load where the voltage is determined by the SRG operation, additional consideration needs to be taken for load variations due to the phase current rising with the assistance of the induced phase voltage.

3.4 – Comparing Motoring and Generating Mode Control

In this chapter, the performance of a 4-phase 8/6 SRM is compared using single pulse and conduction angle control. Key information such as induced voltage, total electromagnetic torque, and phase current are observed to draw comparisons.

In Table 3.1, the mechanical and electrical properties of the 4-phase 8/6 SRM are provided. The motor is controlled using a 4-phase asymmetric bridge converter like the one shown in Fig. 2.16 supplied with 300 V DC-link.

Table 3.1: 4-phase 8/6 SRM properties.

Parameter	Value
Number of phases	4
Number of stator poles (N_s)	8
Number of rotor poles (N_r)	6
Airgap	0.3 mm
Stack height	90 mm
Rated speed	6000 RPM
Phase resistance	0.076 Ω
DC-link voltage	300 V
Rated power	5.2 kW

3.4.1 – Single Pulse Mode

Single pulse mode involves applying a singular pulse every electrical cycle for all the phases. The electrical conduction region in which the pulses are applied dictate whether the motor is in motoring mode or generating mode. Single pulse mode of operation is best used in high-speed operation so that the phase current does not increase rapidly beyond the maximum current limit of the motor.

The conduction angles are selected for motoring mode, then are either shifted by 180 degrees electrical or mirrored along the aligned position (180 degrees electrical) to obtain generating mode conduction angles. This is done to show how motoring and generating modes compare for the same conduction period using single pulse mode. A sample of the shifted and mirrored conduction angles are shown in Fig. 3.6.
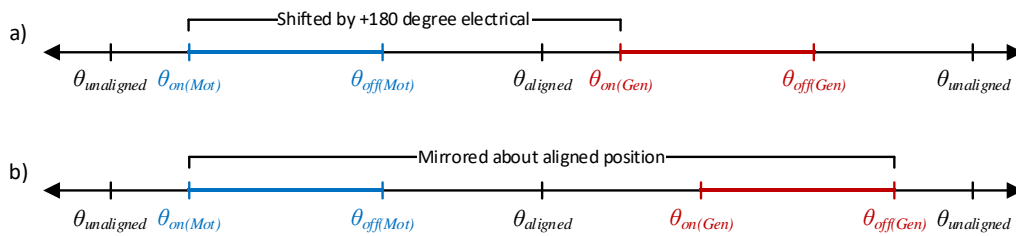
Fig. 3.6: Comparing motoring and mode using (a) shifted conduction angles (b) mirrored conduction angles.

3.4.1.1 – Single Pulse Mode Early Conduction

In Fig. 3.17, the 8/6 SRM is operated at 8000 rpm in motoring mode using single pulse control. The conduction angles were selected to be early in the motoring region (Case 1). The turn-on and turn-off angles were selected as 10 and 90 electrical degrees, respectively. As the turn-on angle is applied, the phase current begins to rise until the induced voltage becomes larger than the DC-link voltage around 40 degrees electrical. At 90 degrees the turn-off angle, negative DC-link voltage is applied to demagnetise the phase.

Next the conduction angles of 10 and 90 degrees were shifted by 180 degrees electrical to observe how the machine would behave in generating mode with a similar conduction period. In Fig. 3.8, single pulse is applied at 190 to 270 degrees electrical (Case 2). After the conduction period begins, positive DC-link

voltage is applied to the phase for excitation. The induced voltage is negative as the machine operates in the generating region of the electrical cycle. During the initial excitation period, as the induced voltage is smaller than the DC-link voltage, the phase current begins to increase. At the turn-off angle, negative DC-link voltage is applied to the phase. When the magnitude of the induced voltage is larger than the phase voltage after the turn-off angle, the phase current continues to rise, but with a smaller slope. This is opposite to the motoring mode of operation. In motoring mode of operation, when the magnitude of the induced voltage is higher than the phase voltage, the phase current reduces. Around 305 degrees electrical, the magnitude of the induced voltage becomes smaller than the DC-link voltage, resulting in the phase demagnetizing and phase current reducing.

In Fig. 3.9, the single pulse motoring mode early conduction angles were mirrored along the aligned position. Hence, conduction angles of 270 and 350 degrees electrical are applied for generating mode (Case 3). It can be observed that after the conduction begins, the phase current starts to rise as the induced voltage is smaller than the DC-link voltage. But there is a noticeable difference in this case as compared to the case in Fig. 3.8. As the conduction occurs much later in the generating mode region in Fig. 3.9, the induced voltage is more negative as compared to the case in Fig. 3.8. This results in a higher rate-of-change of the phase current. At 350 degrees electrical, negative DC-link voltage is applied to demagnetise the phase. But, as the demagnetization of the phase current extends beyond the unaligned position, which is the motoring region, the induced voltage

becomes positive and aids in the phase current demagnetizing more rapidly, unlike

in generating mode with shifted conduction angle case in Fig. 3.8.
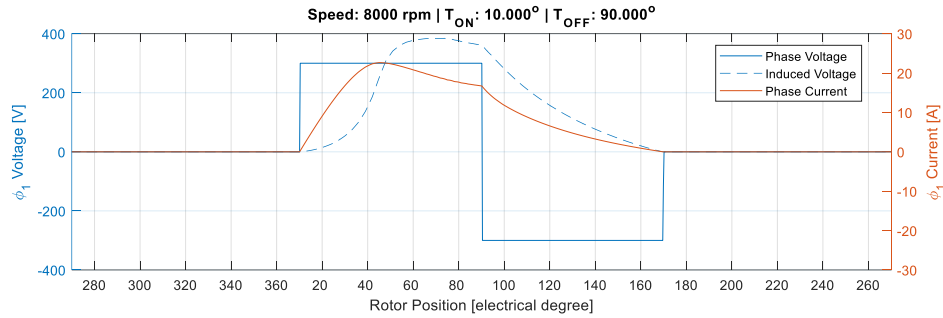
Fig. 3.7: Single pulse control using early motoring conduction (Case 1).
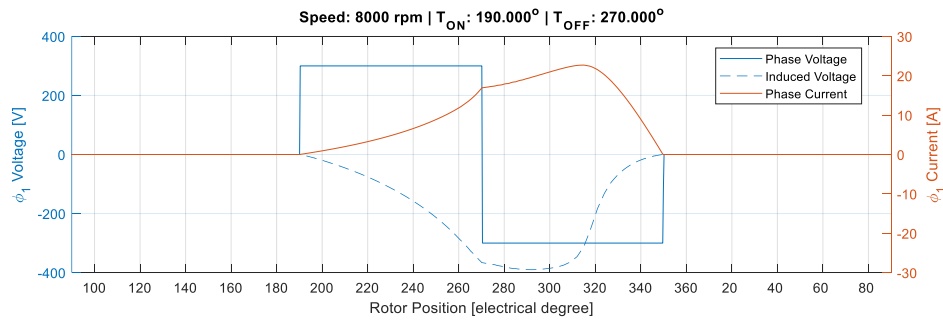
Fig. 3.8: Single pulse control using shifted generation conduction (Case 2).
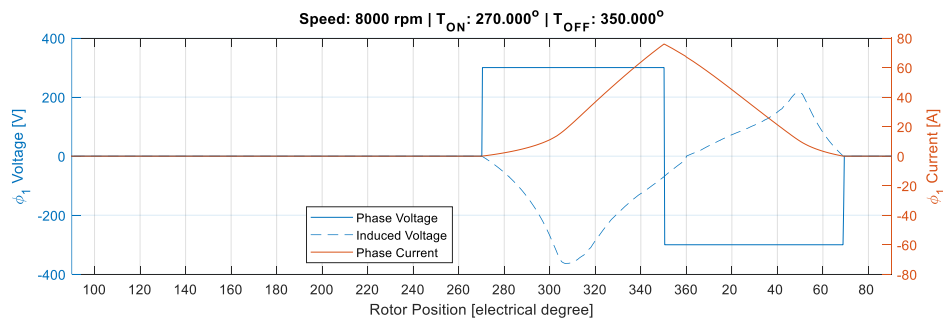
Fig. 3.9: Single pulse control using mirrored generation conduction (Case 3).

The phase currents have been compared for a 4-phase 8/6 SRM at 8000 rpm

with early conduction in motoring mode (Fig. 3.7), shifted conduction in generating

mode (Fig. 3.8), and mirrored conduction in generating mode (Fig. 3.9). This

difference in conduction region influences the torque production and quality as

47

well. In Fig. 3.10, the torque waveform is plotted for motoring mode with early conduction. It can be observed that each phase contributes to the total phase torque, and significant torque ripple is present due to the conduction period and commutation (Case 1). In Fig. 3.11, the torque waveform is plotted for the case where the motoring conduction angles which are shifted by 180 degrees electrical to obtain the generating mode conduction angles (Case 2). The torque is now negative. When Fig. 3.10 and Fig. 3.11 are compared, it can be observed that the torque waveforms are similar in shape but are mirrored along the y-axis and then mirrored by the x-axis. Essentially in this case the two waveforms are similar in behaviour, similar absolute average torque of 3.6 Nm, and a similar torque ripple.

In Fig. 3.12, the torque waveform is plotted for generating mode conduction angles when the motoring conduction angles are mirrored in reference to the aligned position. In this case (Case 3), due to the delayed conduction period, the demagnetising tail current ends up in the motoring mode region. This tail current results in positive torque, reducing the absolute average torque, and contributing to torque ripple.
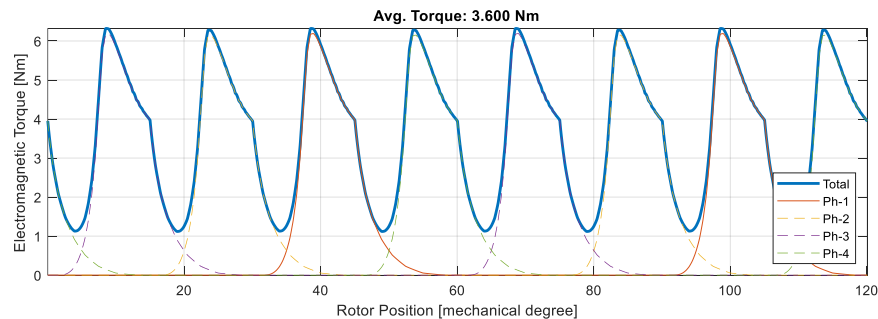
Fig. 3.10: Torque production for early motoring mode conduction (Case 1).
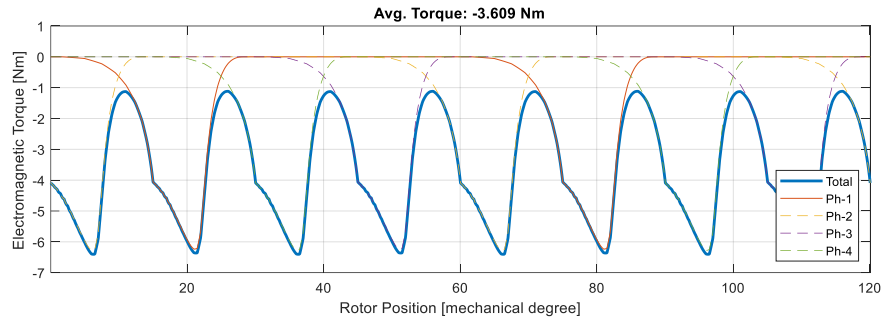
Fig. 3.11: Torque production for shifted generating mode conduction (Case 2).
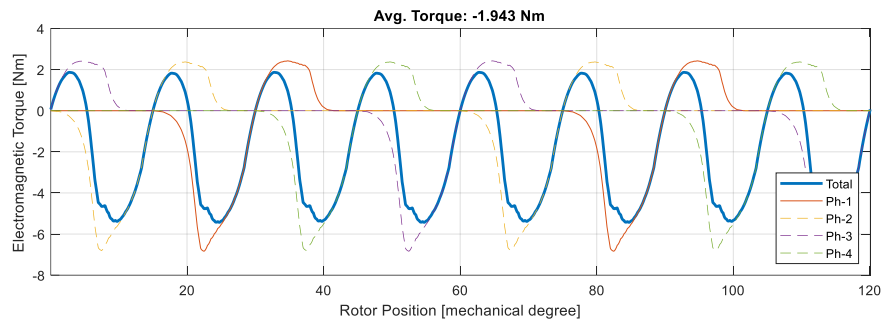
Fig. 3.12: Torque production for mirrored generating mode conduction (Case 3).

In Table 3.2, the torque and source current attributes are shown for the 8/6 SRM with single pulse mode. It can be observed that the motoring (Case 1) and shifted generating (Case 2) case have a similar behaviour for the average torque and source current. But when the motoring mode conduction angles are mirrored (Case 3), the absolute average torque is much lower due to the positive torque. Also, in the mirrored case, the source current.

Table 3.2: Simulation results with early motoring conduction using single pulse control.

Conduction at 8000 rpm		Average torque [Nm]	Phase current RMS [A]	Average source current [A]
Case 1	$\theta_{on} = 10°$ $\theta_{off} = 90°$	3.6	5.1	10.2
Case 2	$\theta_{on} = 190°$ $\theta_{off} = 270°$	-3.6	5.1	-9.8
Case 3	$\theta_{on} = 270°$ $\theta_{off} = 350°$	-1.9	14.0	-4.3

3.4.1.2 – Single Pulse Mode Delayed Conduction

In all the three cases presented earlier the generating mode conduction angles were calculated from motoring mode. In the next cases, single pulse at 8000 rpm is utilized for the same 8/6 SRM but with the motoring conduction occurring later. The subsequent generating angles are then derived by shifting and mirroring the motoring mode conduction angles to observe the difference in phase current and torque behaviour.

In Fig. 3.13, the turn-on and turn-off angles are 60 and 140 degrees, respectively. Hence, the conduction period occurs much later in motoring region. Due to the delayed conduction, the induced voltage rises much quicker and the phase current cannot increase to the value which was observed in Case 1 in Fig. 3.7. The induced voltage is proportional to the speed; hence, the rate of change in flux linkage. As the speed and the conduction interval is the same for Case 1 and Case 4, the difference in induced voltage can be attributed to rate of change in flux linkage. Additionally, the relative difference between the magnitudes of DC-link voltage and induced voltage in each case also effects the rate of change of current.

In Fig. 3.13 in Case 4, the difference between the induced voltage and phase voltage is smaller and it occurs late in the conduction interval. Hence, the phase current rises marginally. Besides, due to the delayed conduction interval, the tail current persists into the generating region and the induced voltage becomes negative. This impacts the torque quality.

In Fig. 3.14, the late motoring conduction intervals in Case 4 are shifted by 180 degrees electrical to obtain the generating mode conduction intervals. In Case 5, the turn-on angle is 240 degrees electrical and turn-off angle is 320 degrees electrical. In Case 5, phase current rises rapidly after the turn-on as compared to Case 2. This is because the induced voltage becomes negative rapidly due to the negative rate of change in flux linkage. In Fig. 3.14, the induced voltage begins to decrease prior to the turn-off angle compared to Fig. 3.8 for Case 2. After the turn-off angle is applied, the phase current magnitude decreases as the magnitude of the induced voltage is smaller than the DC-link voltage. In Case 2 in Fig. 3.8 with earlier conduction period in generating mode, the phase current kept increasing after the turn-off angle due to the difference in the magnitudes of the induced voltage and DC-link voltage. The later conduction in Case 5 results in a turn-off angle closer to the unaligned position, which results in the demagnetization of the phase current extending to the motoring region.

In Fig. 3.15 (Case 6), the late motoring mode conduction period was mirrored along the aligned position. The turn-on and turn-off angles obtained in this case were 220 and 300 degrees electrical, respectively. In Case 6, the phase current begins to rise due to the induced voltage and DC-link relation. But the peak phase

current value in Case 6 is smaller than the one in Fig. 3.14 for Case 5 with shifted conduction angles for generating mode. This can be explained by observing the magnitude of the induced voltage relative to the phase voltage. In Case 6 in Fig. 3.15, the induced voltage remains smaller than the DC-link voltage later into the conduction interval when compared to Case 5 with earlier generating conduction angles. Also, in Case 6 in Fig. 3.15, the magnitude of the induced voltage is larger than the DC-link voltage after the turn-off angle. This results in the phase current to increase for a short interval. Once the magnitude of the induced voltage becomes smaller than the DC-link voltage, the phase current begins to reduce, and the phase demagnetises. Similar to the shifted generation case (Case 5) in Fig. 3.14, the phase current conducts within the motoring region for a short interval in Case 6 in Fig. 3.15. Due to the earlier conduction interval by 20 degrees electrical for the mirrored angles in Case 6, the phase is demagnetised sooner compared to the shifted angles in Case 5. This has a smaller effect on the average torque and ripple.
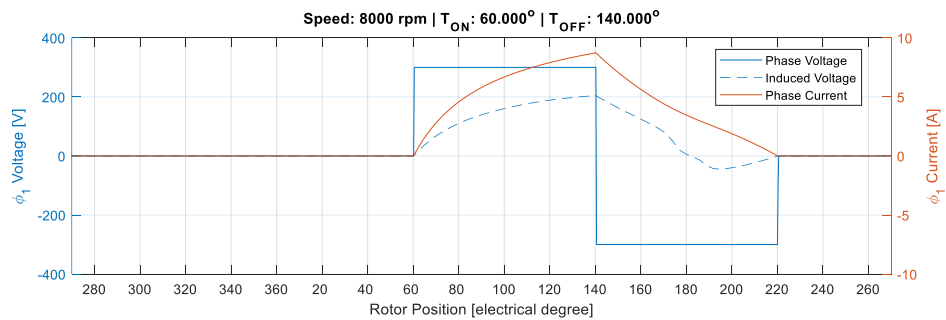
Fig. 3.13: Single pulse control using late motoring mode conduction (Case 4).
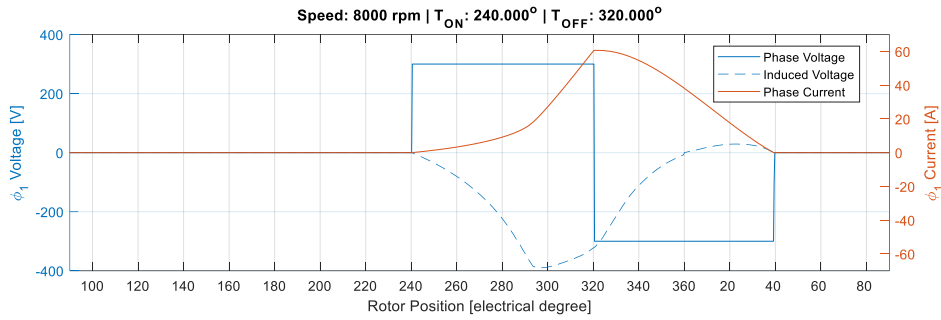
Fig. 3.14: Single pulse control using shifted generation conduction (Case 5).
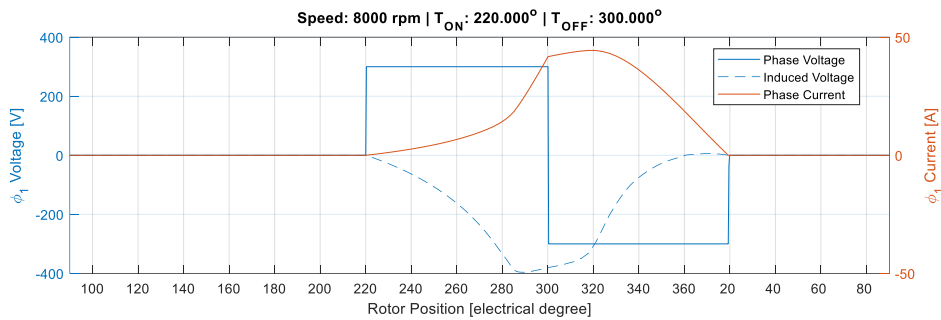
Fig. 3.15: Single pulse control using mirrored generation conduction (Case 6).

In Fig. 3.16, the phase and total torque is plotted for the late motoring mode conduction interval (Case 4) at 8000 rpm using single pulse operation. Due to the later conduction in motoring mode, the phase current did not rise substantially, resulting in the average torque being much smaller than Case 1 in Fig. 3.10, when the phase excitation occurring earlier in Case 4.

In Fig. 3.17, the torque waveform for Case 5 is shown where the generating mode conduction angles are obtained by shifting the motoring mode conduction angles in Case 4 by 180 degrees electrical. Unlike Case 4 motoring mode, in Case 5 generating mode with delayed conduction period a significant torque magnitude is present due to the phase current being assisted by the induced voltage. Due to the delayed conduction period the resulting tail current in each phase produces a positive torque magnitude opposing the desired negative torque magnitude.

53

In Fig. 3.18, the phase and total torque is shown for the mirrored generation case for late conduction (Case 6). In this case, the slightly earlier generating mode conduction period results in less tail current compared to Case 5 and, hence, less opposing torque being generated.
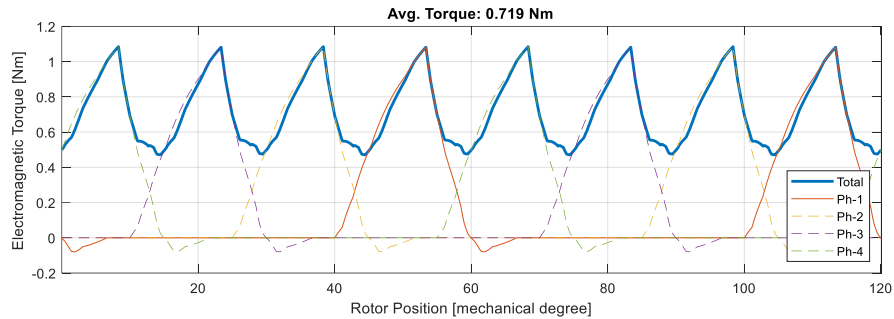
Fig. 3.16: Torque production for late motoring mode conduction (Case 4).
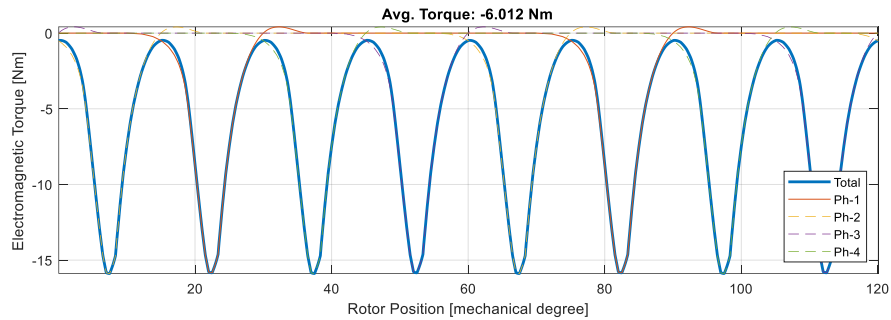
Fig. 3.17: Torque production for shifted generating mode conduction (Case 5).
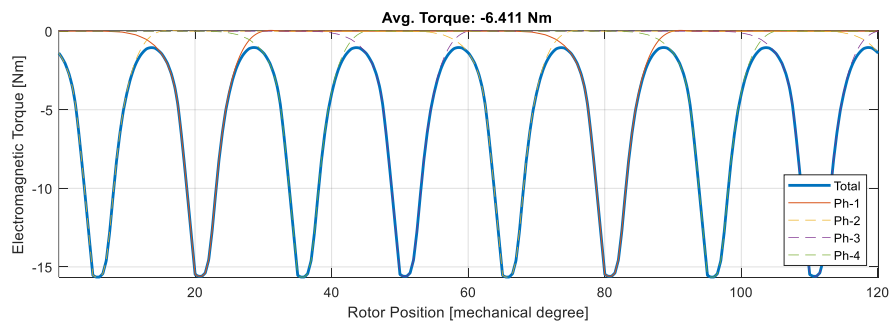
Fig. 3.18: Torque production for mirrored generating mode conduction (Case 6).

In Table 3.3, the torque and source current results for the three conduction intervals with late conduction are summarized. With the late conduction interval

motoring mode case, the phase current had a smaller magnitude as compared to Case 1. This results in a smaller average torque, subsequently a smaller average source current being drawn from the power source. When the late motoring conduction period is shifted by 180 degree in Case 5, the resulting average torque is -6 Nm and an average of 16 A is supplied back to the source. The torque ripple is significant due to the nature of the pulse control scheme. However, when the motoring conduction angles mirrored around the aligned position (Case 6), it results in a slightly earlier conduction period in generating mode. This results in a slightly higher absolute average torque and a smaller ripple than the shifted generation case (Case 5). This is because in Case 6 there is a much smaller phase current which overlapped into the motoring region resulting in positive torque. Additionally, the mirrored conduction angle (Case 6) case had the highest amount of source current supplied back to the DC-link for all cases discussed so far (Cases $1 - 6$).

Table 3.3: Simulation results with late motoring conduction using single pulse control.

Conduction at 8000 rpm		Average torque [Nm]	phase current RMS [A]	Average source current [A]
Case 4	$\theta_{on} = 60°$ $\theta_{off} = 140°$	0.719	2.2	2.0
Case 5	$\theta_{on} = 240°$ $\theta_{off} = 320°$	-6.0	11.6	-16.0
Case 6	$\theta_{on} = 220°$ $\theta_{off} = 300°$	-6.4	9.1	-17.4

From observing motoring and generating mode using single pulse control, it is obvious that the selection of conduction angles is not as simple as shifting or mirroring between the two. Due to the non-linear characteristic of an SRM, unique

consideration needs to be given to operate the SRM in generating mode to maximize the source current while minimizing torque ripple.

Single pulse mode of operation can only be utilized at high speeds as the phase current is not controlled in this mode of operation. With lower speeds, the phase current rises uncontrollably. To observe the differences in motoring and generating mode at lower speeds, an alternative control scheme needs to be utilized, which is discussed in the next sections.

3.4.2 – Current Control – Hard-switching

In this section motoring mode is compared with generating mode using a hysteresis controller with hard switching. Unlike single pulse control, current control can operate at lower motor speeds with the hysteresis controller either with hard or soft-switching.

In Table 3.4, the simulation parameters used to compare generating and motoring mode are presented for the hard-switching case. At 4000 rpm, the current is controllable by the hysteresis controller as the induced voltage is smaller than the DC-link voltage. The conduction intervals are fixed to 110 degrees electrical for both motoring and generating modes. The generating angles were obtained by shifting and mirroring the motoring angles in the same convention as in the single pulse control study in sub-section 3.4.1.

Table 3.4: Current control simulation parameters.

Parameter	Value	
Speed	4000 rpm	
Current reference	20 A, 2 % hysteresis band	
Motoring early conduction (Case 7)	$\theta_{on} = 10°$	$\theta_{off} = 120°$
Motoring late conduction (Case 8)	$\theta_{on} = 60°$	$\theta_{off} = 170°$
Generating early conduction (Case 9)	$\theta_{on} = 190°$	$\theta_{off} = 300°$
Generating late conduction (Case 10)	$\theta_{on} = 240°$	$\theta_{off} = 350°$

In Case 7, hard-switching is applied in motoring mode with early conduction angles of 10 and 120 degrees electrical at 4000 rpm. As the turn-on angle is close to the unaligned position, the phase current rises quickly to 20 A reference, due to the low magnetic circuit inductance. Once the current reaches to the upper band of the hysteresis controller, in hard-switching mode, both switches are turned off to apply negative DC-link voltage to reduce the phase current. The hysteresis controller continues to keep the phase current within the hysteresis band until the rotor position for the turn-off angle is achieved. At the turn-off angle, both switches in the converter are turned off and negative DC-link voltage is applied to demagnetise the phase. During conduction, it can be observed in Fig. 3.19 that the switching intervals become less frequent to control the phase current as the rotor moves to the aligned position. Higher induced voltage and phase inductance near the aligned position results in a current with a smaller rate of change.

In Fig. 3.20 (Case 8), the current waveform is shown for motoring mode with later conduction angles of 60 and 170 degrees electrical at 4000 rpm using hard-switching. Due to the later conduction, which is closer to the aligned position,

the magnetic circuit inductance is higher. This results in the induced voltage magnitude becoming large quickly relative to the DC-link voltage after the conduction starts. The later conduction results in the phase current to build much slower as shown in Fig. 3.20, when compared to the early conduction case in Fig. 3.19. This results in the phase current not being in the hysteresis band for a long time. Once the turn-off angle is applied at 170 degrees electrical in Fig. 3.20, again due the high magnetic circuit inductance, the current decreases slowly resulting a significant tail current and extends the conduction to the negative torque region.
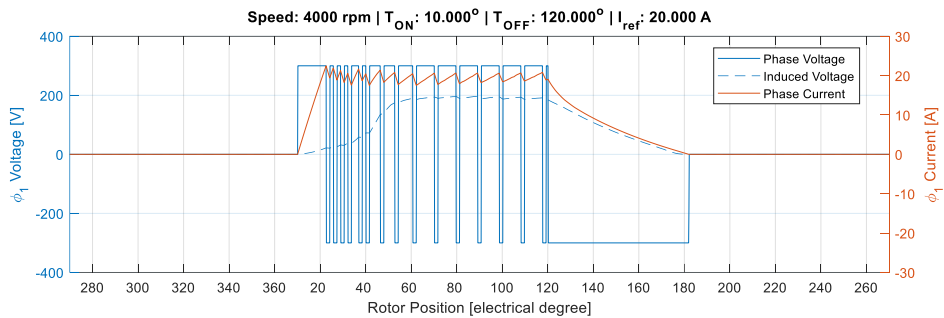
Fig. 3.19: Phase current waveform using hard-switching current control for early motoring mode conduction (Case 7).
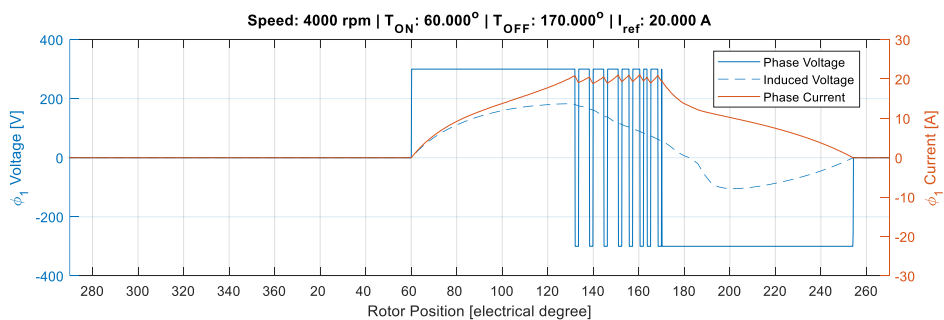
Fig. 3.20: Phase current waveform using hard-switching current control for late motoring mode conduction (Case 8).

In Fig. 3.21, the torque ripple due to the hysteresis controller using hard switching can be observed for the early conduction motoring mode case. However,

the largest torque ripple is attributed from the commutation region. The torque ripple can be reduced if the conduction angles are selected specifically to do so.

The average torque magnitude is affected due to the delayed conduction angles of 60 and 170 degree electrical in Case 8 as shown in Fig. 3.22. In the phase torque, it can be observed that each phase torque component takes time to rise, this results in an excessively long commutation period with a reduced hysteresis interval. Further negative phase torque is produced, due to the tail current trailing into the generating mode region. This results in a smaller average torque and higher torque ripple than the one observed in the early motor conduction angle case (Case 7) in Fig. 3.21.
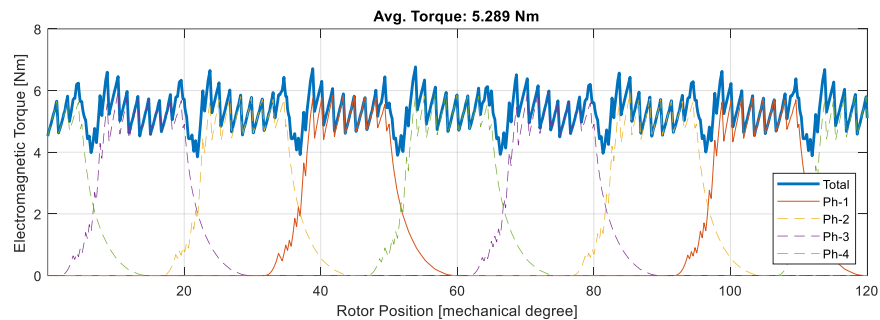
Fig. 3.21: Torque waveform using hard-switching current control for early motoring mode conduction (Case 7).
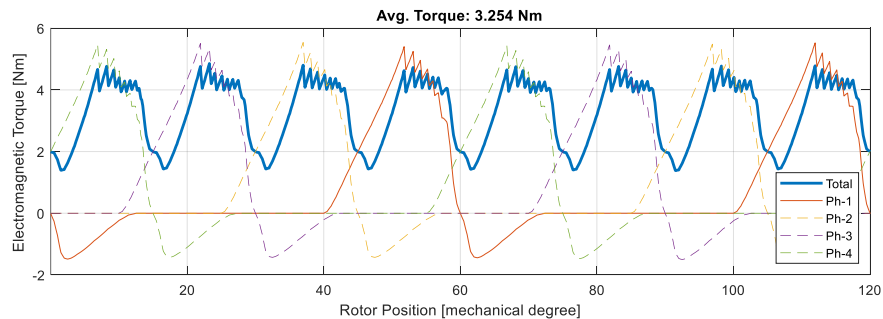
Fig. 3.22: Torque waveform using hard-switching current control for late motoring mode conduction (Case 8).

Next, Case 9 is analyzed with early generating mode conduction angles of 190 and 300 degree electrical at 4000 rpm as depicted in Fig. 3.23. At the turn-on angle, the induced voltage becomes negative and, due to the higher inductance near the aligned position, the phase current takes a longer time to increase. At the turn-off angle, the phase current decreases rapidly due to induced voltage magnitude decreasing rapidly relative to the DC-link voltage magnitude. In hard-switching, to reduce the phase current, both switches are turned-off, for a longer period in the early conduction generation case.

The generation conduction is analyzed at 4000 rpm with the conduction angles of 240 and 350 degree electrical as shown in Fig. 3.24. Once the turn-on angle is applied, the phase current beings to increase but has a faster rise time. This is because, with the delayed conduction, the magnetic circuit inductance is much lower at the phase turn-on. Similar to the early motoring conduction case in Fig. 3.19 (Case 7), the switching frequency is increasing as the rotor moves closer to unalignment.
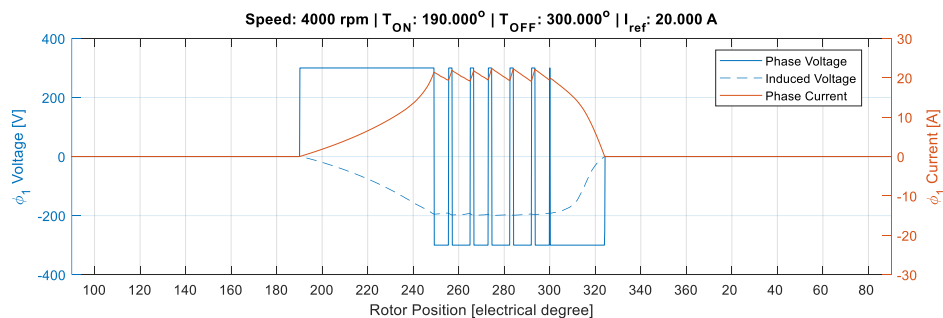
Fig. 3.23: Phase current waveform using hard-switching current control for early generating mode conduction (Case 9).
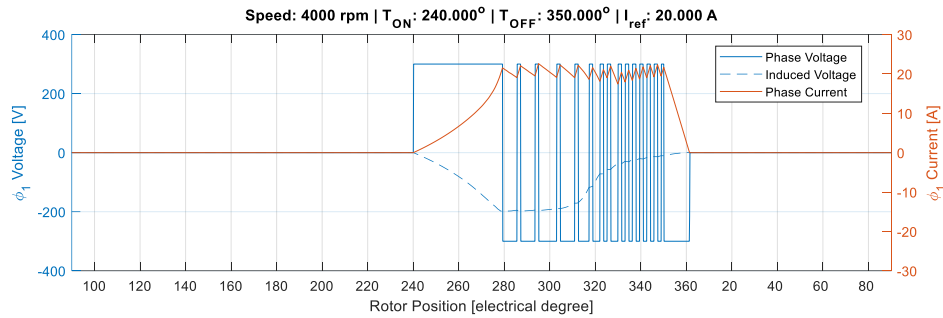
Fig. 3.24: Phase current waveform using hard-switching current control for late generating mode conduction (Case 10).

In Fig. 3.25, the phase and total torque are plotted for generating mode with early conduction period. It can be observed that the torque takes longer to build up after the turn-on angle due to the smaller rate of change in the phase current. After the turn-off angle is applied the torque reaches to zero relatively quickly. The slow torque response adds to the torque ripple during commutation. Similar to the motoring current control cases, the torque ripple due to commutation can be improved with specific conduction angles.

In Fig. 3.26, the phase and total torque are plotted for generating mode with late conduction period. There is no positive torque generation as there is no tail current decaying into the motoring region. The only significant source of torque ripple is from the commutation region, and like all cases before, it can be minimized by selecting conduction angles that minimize the commutation region.
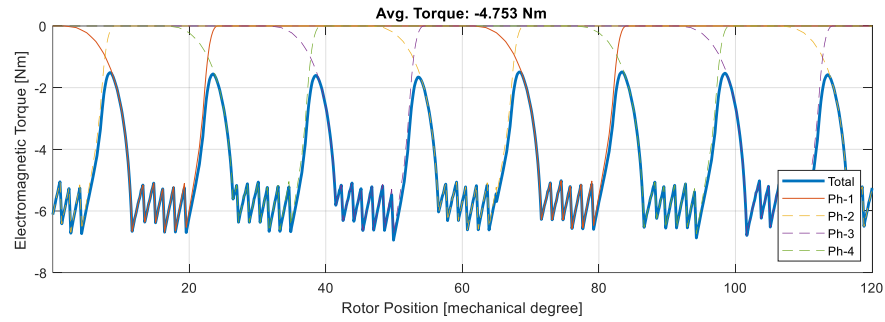
Fig. 3.25: Torque waveform using hard-switching current control for early motoring mode conduction (Case 9).
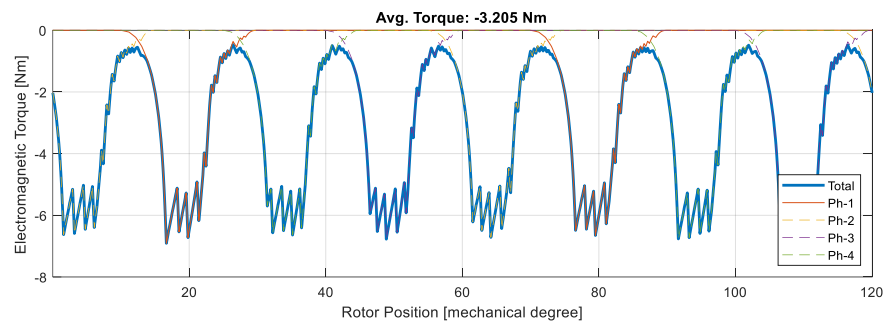
Fig. 3.26: Torque waveform using hard-switching current control for late generating mode conduction (Case 10).

In Table 3.5, the average torque and source current are shown for all the late and early conduction regions for motoring and generating mode. The highest average torque and smallest torque ripple was observed when early conduction was applied in motoring mode (Case 7). The largest negative torque was also observed in early generating mode with the smallest torque ripple (Case 9). Interestingly, the largest torque ripple observed was for the generating mode late conduction (Case 10) and was largely attributed from the commutation region, as the torque production became marginal near the aligned position (Fig. 3.24 and Fig. 3.26).

Table 3.5: Simulation results for current control using hard-switching.

4000 rpm at 20 A current reference		Average torque [Nm]	Phase current RMS [A]	Average source current [A]
Case 7	$\theta_{on} = 10^\circ$ $\theta_{off} = 120^\circ$	5.3	6.9	7.6
Case 8	$\theta_{on} = 60^\circ$ $\theta_{off} = 170^\circ$	3.3	6.5	4.8
Case 9	$\theta_{on} = 190^\circ$ $\theta_{off} = 300^\circ$	-4.8	5.1	-6.4
Case 10	$\theta_{on} = 240^\circ$ $\theta_{off} = 350^\circ$	-3.2	5.2	-4.2

3.4.3 – Current Control – Soft-switching

In Section 3.4.2, current control was used with hard-switching, but soft-switching is used more often to control the phase current in SRM drives. The key difference in soft-switching is that during the conduction period, the motor phase is short circuited by turning on one switch and turning off the other switch of the asymmetric bridge converter as shown in Fig. 2.17(c). In (3.1), the hysteresis control conditions for hard-switching are shown for motoring mode:

$$V_{ph}(k) = \begin{cases} 0 & excitation\ signal \leq 0 \cap i_{ph} \leq 0 \\ -V_{DC} & excitation\ signal \leq 0 \cap i_{ph} > 0 \\ -V_{DC} & excitation\ signal > 0 \cap i_{ph} \geq I_{upper} \\ +V_{DC} & excitation\ signal > 0 \cap i_{ph} < I_{lower} \\ V_{ph}(k-1) & excitation\ signal > 0 \cap I_{upper} > i_{ph} \geq I_{lower} \\ 0 & otherwise. \end{cases} \quad (3.1)$$

where $V_{ph}(k)$ is the phase voltage application, and $V_{ph}(k-1)$ is the previous phase voltage. In (3.2), the hysteresis control conditions for soft-switching are shown for motoring mode.

$$V_{ph}(k) = \begin{cases} 0 & excitation\ signal \leq 0 \cap i_{ph} \leq 0 \\ -V_{DC} & excitation\ signal \leq 0 \cap i_{ph} > 0 \\ 0 & excitation\ signal > 0 \cap i_{ph} \geq I_{upper} \\ +V_{DC} & excitation\ signal > 0 \cap i_{ph} < I_{lower} \\ V_{ph}(k-1) & excitation\ signal > 0 \cap I_{upper} > i_{ph} \geq I_{lower} \\ 0 & otherwise. \end{cases} \quad (3.2)$$

There are benefits to using soft-switching when compared to hard-switching in motoring mode. The rate-of-change of phase current can be lower using soft-switching since zero voltage is applied as the phase voltage in soft-switching instead of negative DC-link voltage in hard-switching. This results in a lower switching frequency, resulting in the torque ripple within the conduction region to improve. In soft-switching, during hysteresis control, only one switch is operated instead of two. This can help reducing both conduction and switching losses.

3.4.3.1 – Current Control using Soft-switching at Low-speed

Similar to the hard-switching hysteresis control cases, the motoring and generating performance are compared using soft-switching at 4000 rpm using the condition angles presented in Table 3.1. The effects of hard and soft-switching are also compared for the same conduction angles.

In Fig. 3.27, the phase current is shown for motoring mode with early conduction angles of 10 and 110 degrees electrical using soft-switching. As compared to hard-switching case (Case 7) in Fig. 3.19, soft switching results in a smoother current waveform during the conduction period.

In Fig. 3.28, late motoring conduction angles of 60 and 170 degree electrical are used with soft-switching. As compared to the hard-switching case (Case 8) in Fig. 3.20, the current waveform is similar with a smaller switching frequency in the conduction interval.
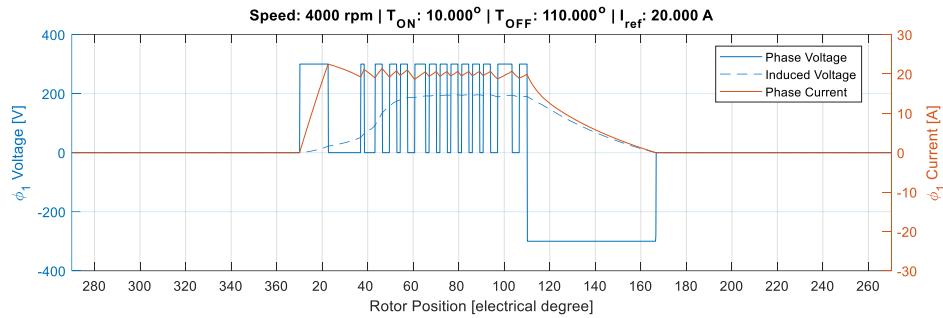
Fig. 3.27: Phase current waveform using soft-switching current control for early motoring mode conduction (Case 11).
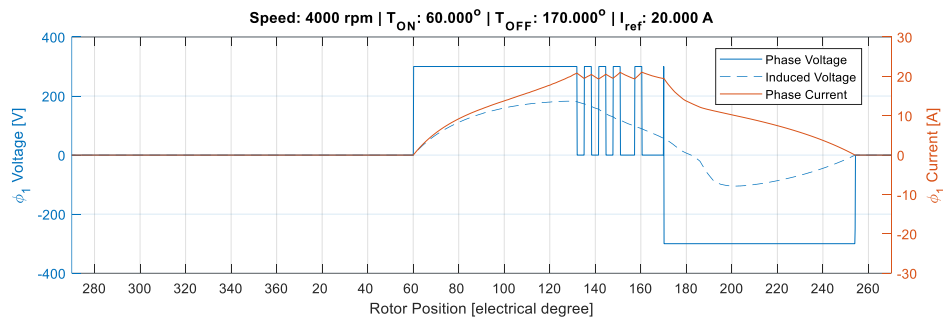
Fig. 3.28: Phase current waveform using soft-switching current control for late motoring mode conduction (Case 12).

In Fig. 3.29, the phase and total torque are plotted for early motoring conduction using soft-switching. Compared hard-switching with the same conduction angles (Case 7 in Fig. 3.21), the average torque is 7.5 % smaller, but the torque ripple is also slightly lower. Essentially, soft-switching and hard-switching have very similar performance when observing torque waveforms, as the only difference is due to the change in switching frequency during conduction. When using soft-switching in motoring mode, the average source current draw is 7.0 A. Soft-switching resulted in a 7.9 % decrease in source current draw, as compared to hard-switching.

In Fig. 3.30, the torque waveforms are plotted for late motoring conduction. Soft-switching results in a very small reduction in average torque and torque ripple

when compared to hard-switching (Case 8 in Fig. 3.22). Essentially, the torque performance was unchanged between the two switching modes. As for the source current, when using soft-switching and hard-switching the current drawn was the same. However, the harmonics from soft-switching are expected to be smaller in magnitude due to the source current in soft-switching experiencing a smaller change in magnitude compared to hard-switching.
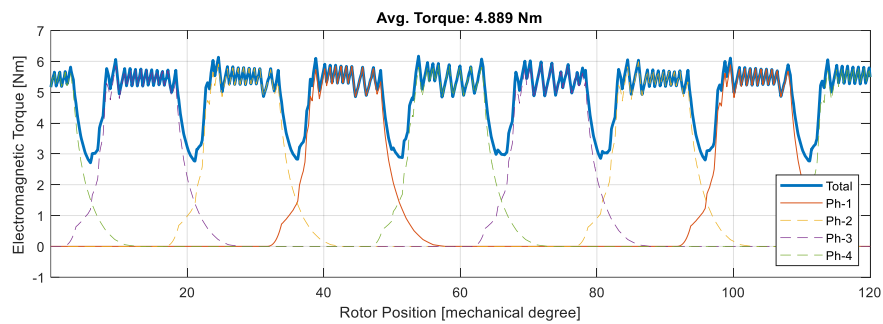
Fig. 3.29: Torque waveform using soft-switching current control for early motoring mode conduction (Case 11).
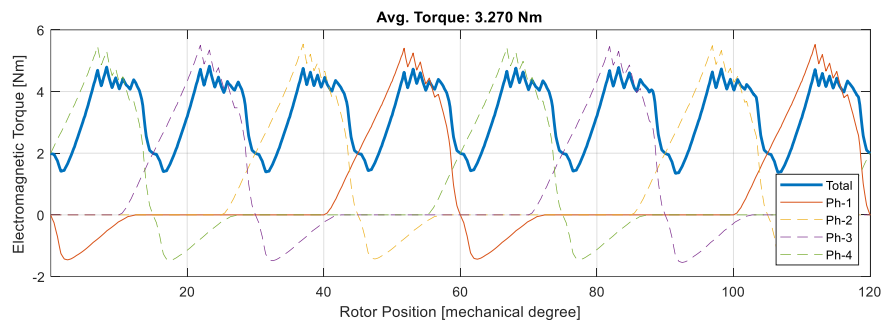
Fig. 3.30: Torque waveform using soft-switching current control for late motoring mode conduction (Case 12).

In Fig. 3.31, the same soft-switching control in (3.2) as in the motoring mode is applied for early generation using conduction angles of 190 and 300 degree electrical at 4000 rpm. After the turn-on angle is applied, the phase current begins to rise. When the phase current reaches the upper hysteresis band, the asymmetric bridge converter short circuits the phase, as per soft-switching requirements. In

generating mode, the shorted phase results in the phase current to rise with a larger slope rather than decrease as it would in motoring mode. This is because, in generating mode, when zero phase voltage is applied, the induced voltage is negative. As the induced voltage is smaller than phase voltage, using (3.3) and (3.4), the resulting rate-of-change of phase current is positive. Thus, the phase current increases. Once, the turn-off angle is applied, negative DC-link voltage is applied to the phase. As the magnitude of the induced voltage is smaller than the magnitude of the phase voltage, the phase current reduces. This shows that the soft-switching in motoring mode cannot be applied in generating mode; otherwise it results in uncontrolled peak current. For soft-switching to work in generating mode, some modifications need to be applied for current regulation.

$$\frac{V-\varepsilon}{L} = \frac{di}{dt} \tag{3.3}$$

$$\varepsilon = i\frac{\partial L(\theta)}{\partial \theta}\omega_r \tag{3.4}$$
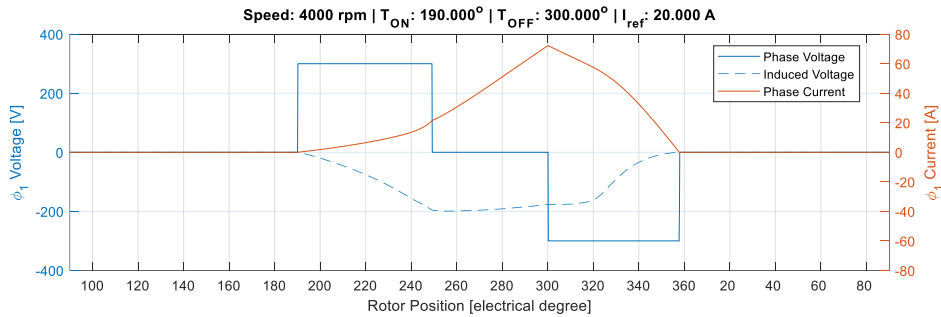
Fig. 3.31: Phase current waveform using the same soft-switching control in motoring mode for early generation mode conduction.

In (3.5), a modified hysteresis controller is presented to control the phase current with soft-switching in generating mode. The main difference is that when the phase current is higher than the upper hysteresis band, negative DC-link voltage

is applied rather than zero. When a negative DC-link voltage is applied, as the induced voltage magnitude is lower than the phase voltage magnitude, especially at lower speed operation, the phase current reduces. As the phase voltage is negative, the phase current is supplied to the source. However, at higher speeds the magnitude of the induced voltage can be greater than the DC-link voltage, resulting in the phase current to increase, depending on the rotor position and phase current magnitude.

In soft-switching in motoring mode of operation, when the phase current is smaller than the lower hysteresis band, positive DC-link voltage is applied to increase the phase current. In soft-switching for generating mode operation in (3.5), freewheeling mode is applied where the phase winding is short-circuited. This results in the magnitude of the induced voltage being smaller than the phase voltage. The phase current rises. However, since the phase winding is not connected to the source, no power supplied or drawn from the source. The rise of the phase current is due to the power drawn from the prime mover.

With hysteresis control model in (3.5), the only time current is drawn from the power source is during the initial phase excitation where positive DC-link voltage is applied across the phase winding. This is essential, as an SRM does not have an independent source of excitation and it needs to draw the initial excitation from the source, For the remainder of the hysteresis control, only zero and negative DC-link voltage is applied. In generating mode, when the SRM phase is free wheeling, the phase current rises by drawing mechanical power from the prime mover. Once the SRM phase is connected across negative DC-link the phase current

is supplied back to the power source. With the generating mode soft-switching hysteresis controller, more source current should be supplied back to the power source to improve the generation capability of the SRM.

$$V_{ph}(k) = \begin{cases} 0 & excitation\ signal \leq 0 \cap i_{ph} \leq 0 \\ -V_{DC} & excitation\ signal \leq 0 \cap i_{ph} > 0 \\ -V_{DC} & excitation\ signal > 0 \cap i_{ph} \geq I_{upper} \\ 0 & excitation\ signal > 0 \cap i_{ph} < I_{lower} \\ V_{DC}^* & excitation\ signal > 0 \cap i_{ph} < I_{lower}\ * \\ V_{ph}(k-1) & excitation\ signal > 0 \cap I_{upper} > i_{ph} \geq I_{lower} \\ 0 & otherwise. \end{cases} \quad (3.5)$$

Used for initial excitation.

In Fig. 3.32, the hysteresis control conditions in (3.5) are used for early generation conduction angles of 190 and 300 degree electrical. By using the newer hysteresis controller conditions once the phase current reaches the upper hysteresis band, the SRM phase is supplied by negative DC-link voltage to reduce the phase current. When the phase current reaches the lower hysteresis band, the SRM phase is short circuited and, since to the induced voltage is smaller than the phase voltage, the current begins to rise. Once the turn-off angle is achieved, the SRM phase is demagnetized.

In Fig. 3.33, the soft-switching hysteresis conditions in (3.5) are used to control the phase current in generating mode with later conduction angles of 240 and 350 degrees electrical. Similar, to the case before the phase current is controlled within the hysteresis band.
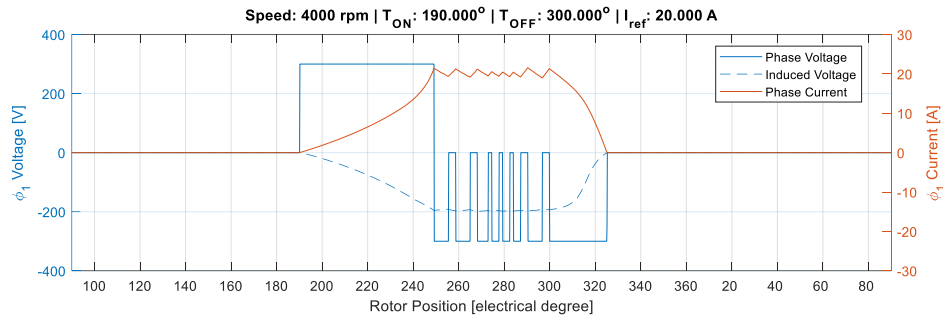
Fig. 3.32: Phase current waveform using soft-switching current control for early generation mode conduction (Case 13).
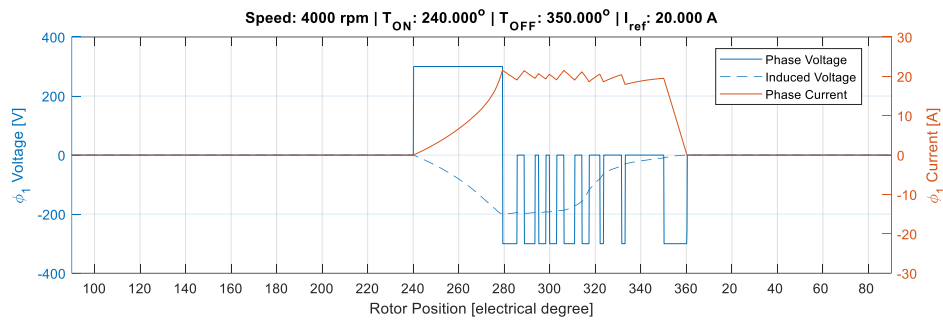
Fig. 3.33: Phase current waveform using soft-switching current control for late generation mode conduction (Case 14).

In Fig. 3.34, the torque waveforms are plotted for the generating mode with early conductions. By using the new hysteresis conditions the phase current is controlled using soft-switching. As a result, the torque is also controlled and does not rise uncontrollably. When comparing the total torque from generating mode using hard-switching the average torque using soft-switching reduced by 4.2 %, and the torque ripple remains similar. Soft-switching does not affect the torque production capability significantly, and it can be improved by selecting specific conduction angles to reduce the torque ripple due to commutation.

In Fig. 3.35, the phase and total torque is plotted for late generation conduction while using the new soft-switching control. Essentially, the torque performance was unchanged for the same conduction angles.
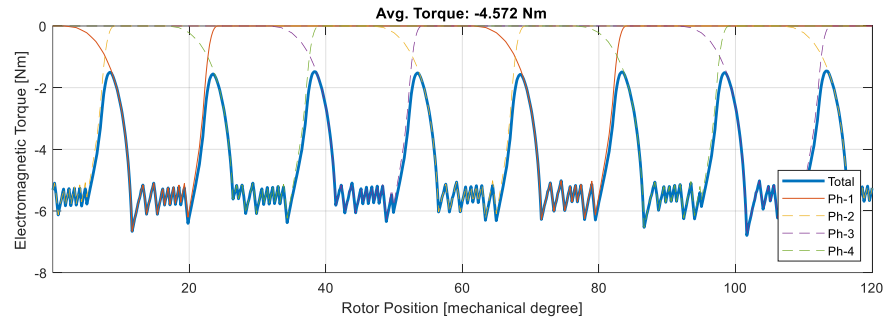
Fig. 3.34: Torque waveform using soft-switching current control for early generation mode conduction (Case 13).
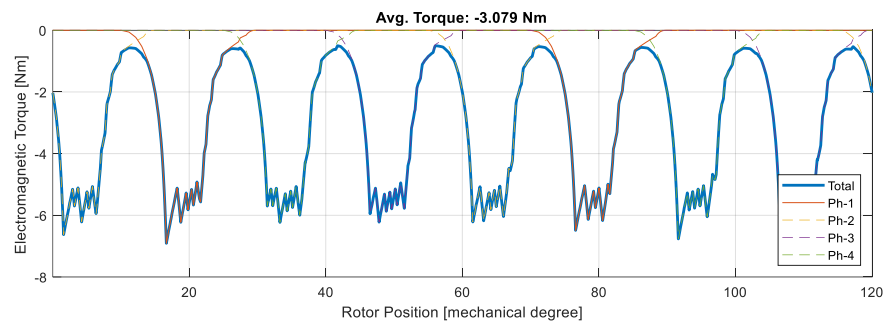
Fig. 3.35: Torque waveform using soft-switching current control for late generation mode conduction (Case 14).

When soft-switching used in generating mode, the source current supplied to the power source is expected to be different when compared to the hard-switching case. When comparing the source current using soft and hard-switching during early generating conduction (comparing Case 13 and Case 9), there was a slight reduction in the source current when using soft-switching. In Fig. 3.36 and Fig. 3.37, the source current using hard-switching and soft-switching is shown for early generation conditions. When observing the hard-switching source current, source current is drawn during the conduction period, but the source current draw interval is very small within the hysteresis band. While using soft-switching, the freewheeling intervals are larger but does not draw current from the source. This difference in operation results in small difference in the average source current

waveforms for hard and soft-switching cases. However, there are differences in the instantaneous source current waveforms. The soft-switching case has far less switching, which requires less filtering and potentially a smaller capacitance. Furthermore, with soft-switching conduction, the switching losses can be reduced as only one switch conducts to control the phase current.
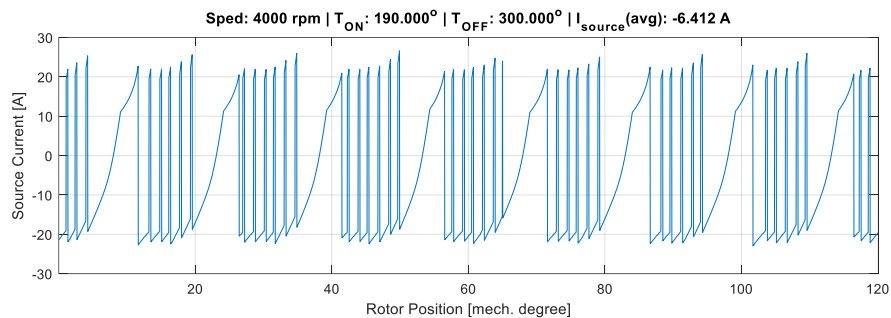
Fig. 3.36: Source current using hard-switching for early generation (Case 9).
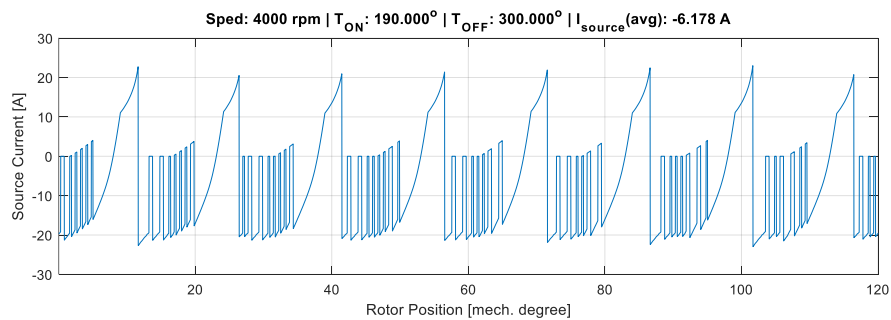
Fig. 3.37: Source current using soft-switching for early generation (Case 13).

In Fig. 3.38 and Fig. 3.39 the source current is plotted for the same late generation conduction angles of 240 and 350 degree electrical for hard (Case 10) and soft-switching (Case 14). Similar source current behaviour is observed when comparing late generation conduction. The hard-switching case supplied back slightly higher source current compared to soft-switching.
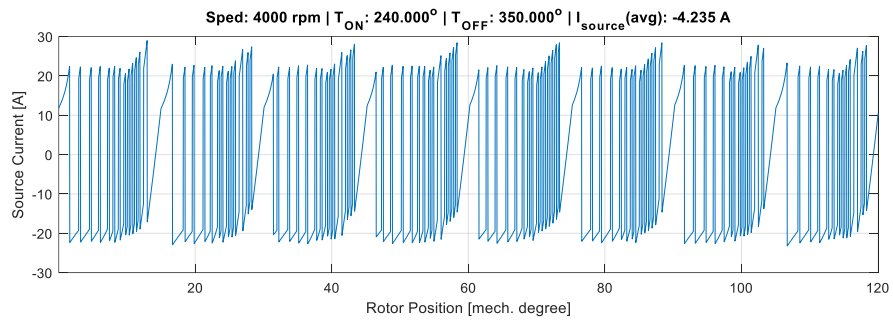
Fig. 3.38: Source current using hard-switching for late generation (Case 10).
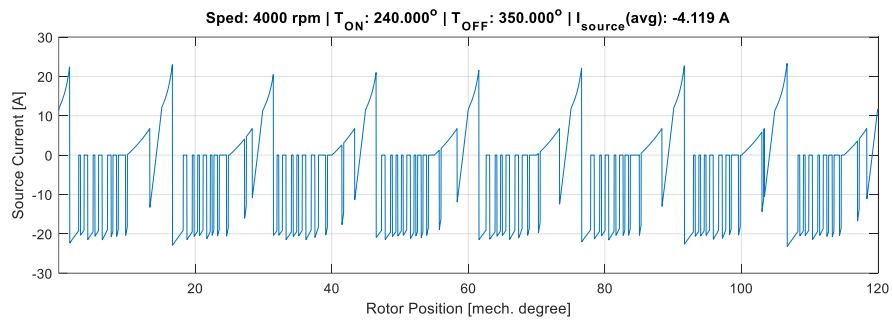
Fig. 3.39: Source current using soft-switching for late generation (Case 14).

3.5 – Conclusion

In conclusion, the SRM can be controlled in motoring mode as well as generating mode using single pulse control and current control. The single pulse control is effective when operating at high speeds. The current control scheme in motoring and generating mode uses the same hysteresis control conditions when using hard-switching. The hysteresis control conditions need to be modified for the controller to operate in generating mode with soft-switching. Different considerations need to be given for generating mode when selecting conduction angles to maximize the performance. Motoring and generating modes can behave differently despite the inductance profiles are symmetric and mirrored around the aligned position. Furthermore, as the rotor speed increases beyond the base speed of the motor the phase current cannot be controlled by the hysteresis controller using hard or soft-switching.

Chapter 4. Optimization Objectives to Improve Generating Mode Performance

In this chapter the conduction angles for the asymmetric bridge converter are selected using an optimizer. The principal purpose is to determine the specific optimization objective parameters to improve the performance in generating mode as opposed to motoring mode, which has different requirements. The 4-phase 8/6 SRM from Chapter 3 is used for the optimization.

4.1 – Optimization of Conduction Angles

The classical control in a switched reluctance machine requires the selection of conduction angles and the current reference for a given operating condition. Selecting conduction angles can be based on different objectives and constraints. As it will be presented in this chapter, these objectives might differ in motoring and generating mode of operations for performance improvement.

The selection of the conduction angles for the control of an SRM can be accomplished by maximizing or minimizing specific fitness functions using an optimization algorithm. For SRMs, the average torque, RMS value of torque ripple, and RMS value of phase current can be the objectives used for the motoring mode region. The average torque can be determined using:

$$T_{avg} = \frac{1}{\theta_2 - \theta_1} \int_{\theta_1}^{\theta_2} T(\theta) d\theta \qquad (4.1)$$

where T_{avg} is the average torque, $T(\theta)$ is the instantaneous rotor torque at a specific rotor position, and θ_1 and θ_2 are rotor positions representing the start and end of

one complete electrical cycle. The RMS value of torque ripple (ΔT_{RMS}) and RMS

value of phase current (I_{RMS}) are defined in (4.2) and (4.3), respectively;

$$\Delta T_{RMS} = \sqrt{\frac{1}{\theta_2 - \theta_1} \int_{\theta_1}^{\theta_2} (T(\theta) - T_{ave})^2 d\theta} \tag{4.2}$$

$$I_{RMS} = \sqrt{\frac{1}{\theta_2 - \theta_1} \int_{\theta_1}^{\theta_2} I^2(\theta) d\theta} \tag{4.3}$$

where $I(\theta)$ is the instantaneous phase current for a given rotor position. These

optimization objectives can also be configured as a relation of one another to be

used in a single fitness function. For example, the average torque ripple and RMS

value of phase current can be configured as T_{avg} / I_{RMS} to optimize for maximum

torque per ampere representing the motor efficiency.

The optimizer can also be provided with linear and non-linear constraints.

The conduction angle selection is a linear constraint:

$$\begin{bmatrix} 1 & -1 \\ -1 & 1 \end{bmatrix} \begin{bmatrix} \theta_{on} \\ \theta_{off} \end{bmatrix} < \begin{bmatrix} -\frac{360}{m} \\ \frac{360k}{m} \end{bmatrix} \tag{4.4}$$

where k is an arbitrary positive constant used to configure the upper boundary of

conduction. A non-linear constraint can be a limit on the RMS phase current:

$$I_{RMS} \leq I_{RMS_{Contriant}} \tag{4.5}$$

where $I_{RMS_{Contriant}}$ is the user defined RMS phase current constraint.

There is a magnitude of optimizers available to be used to improve specific

aspects of the SRMs dynamic performance. One such optimizer is the Genetic

Algorithm (GA) optimizer. The GA optimizer selects working conditions using

natural selection. The optimizer starts with random working conditions, and the

user can define the starting population size. All the working conditions are then evaluated for specific fitness functions and constraints. The working conditions are selected using their fitness function value to produce offspring that combine their parent's attributes. The optimizer re-evaluates to produce new offspring until the working conditions do not deviate any further, and the solution converges. To ensure that a local optimal point is not found, mutations are introduced randomly to vary the offspring. The genetic algorithm can be used for single objective or multi-objective optimization. In a single objective case, the performance of fitness function is maximized or minimized; for example, the average torque can be maximized. This will possibly lead to other performance characteristics detreating, such as the torque ripple and phase current increasing. Multi-objective optimization can be used to optimize for a magnitude of objectives and find various working conditions, known as a Pareto front. The user can then manually select the working condition that favour a specific objective.

4.2 – Optimization to Maximize Absolute Average Torque and Minimize Torque Ripple Using Current Control

In an SRM drive, typical objectives that are used to determine the conduction angles in motoring mode of operation are maximizing the average torque and minimizing the RMS value of torque ripple. These objectives are targeted in motoring mode to achieve a high torque output and smoother operation with lower torque ripple. In this section, these objectives are applied both for motoring and generating modes, to observe how they impact the performance in

generating mode of operation. For this purpose, the objectives are selected to maximize the absolute value of average torque and minimize the RMS value of torque ripple. The optimizer is supplied with various speed and current reference cases to determine various working conditions, and a torque-speed map is developed for motoring and generating modes.

4.2.1 – Motoring Mode

For the motoring mode cases, the average torque is maximized, and the torque ripple is minimized. The constraints for the optimization are shown in (4.6).

$$
\begin{aligned}
-90^o \leq \theta_{on} \leq 90^o \\
90^o \leq \theta_{off} \leq 180^o \\
\theta_{off} - \theta_{on} \geq 90^o \\
\theta_{off} - \theta_{on} \leq 180^o \\
I_{RMS} \leq 60 \ A
\end{aligned}
\tag{4.6}
$$

The turn-on angle is constrained between -90 and 90 degrees electrical, and the turn-off angle is constrained between 90 and 180 degrees electrical. Hence, the minimum conduction interval is 90 degrees electrical, and the maximum conduction interval is 180 degrees electrical. The phase current is constrained to 60 A_RMS. The optimizer finds working conditions for speeds from 500 rpm to 8000 rpm with 500 rpm intervals. The current reference is varied from 0 to 50 A with a 5 A step interval.

In the first case hard-switching current control is used. As a multi objective optimizer is utilized, a Pareto front is obtained for the two objectives. When selecting the working conduction angles for a specific operating point from the Pareto front, the absolute average torque production is prioritized as, it was

observed that the torque ripple objective does not vary significantly for the given motor characteristics.

In Fig. 4.1(a), the contour plot for the RMS value of the torque ripple is shown. As the average torque increases, the RMS value of torque ripple increases. This is because the higher torque demand requires a larger conduction interval, which also increases the torque ripple, shown in Fig. 4.1(e). Also, as the average torque increases a higher phase current is drawn to meet the torque demand. In Fig. 4.1(c) and (d), the turn-on and turn-off angle contours are shown. As the speed increases, both the turn-on and turn-off angles are advanced by occurring earlier than the unaligned and aligned position, respectively. But the increase in torque does not result in the conduction angles to advance.

In Fig. 4.2, the torque-speed envelope is shown for motoring mode using soft-switching current control. The exact same hysteresis band and current sampling conditions as the hard-switching are used. In Fig. 4.2(a), the RMS torque ripple is plotted. Similar to the hard-switching case in Fig. 4.1(a), the torque ripple increases as the average torque increased. The phase current contour also increases as the average torque increases, shown in Fig. 4.2 (b). In Fig. 4.2(c) and (d), the turn-on and turn-off angle contours are shown for soft-switching. Similar to the hard-switching case, as the rotor speed increases the conduction angles advanced and the conduction interval increases as the average torque increases, shown in Fig. 4.2(e). The torque-speed envelope for soft-switching is similar to that of hard-switching.
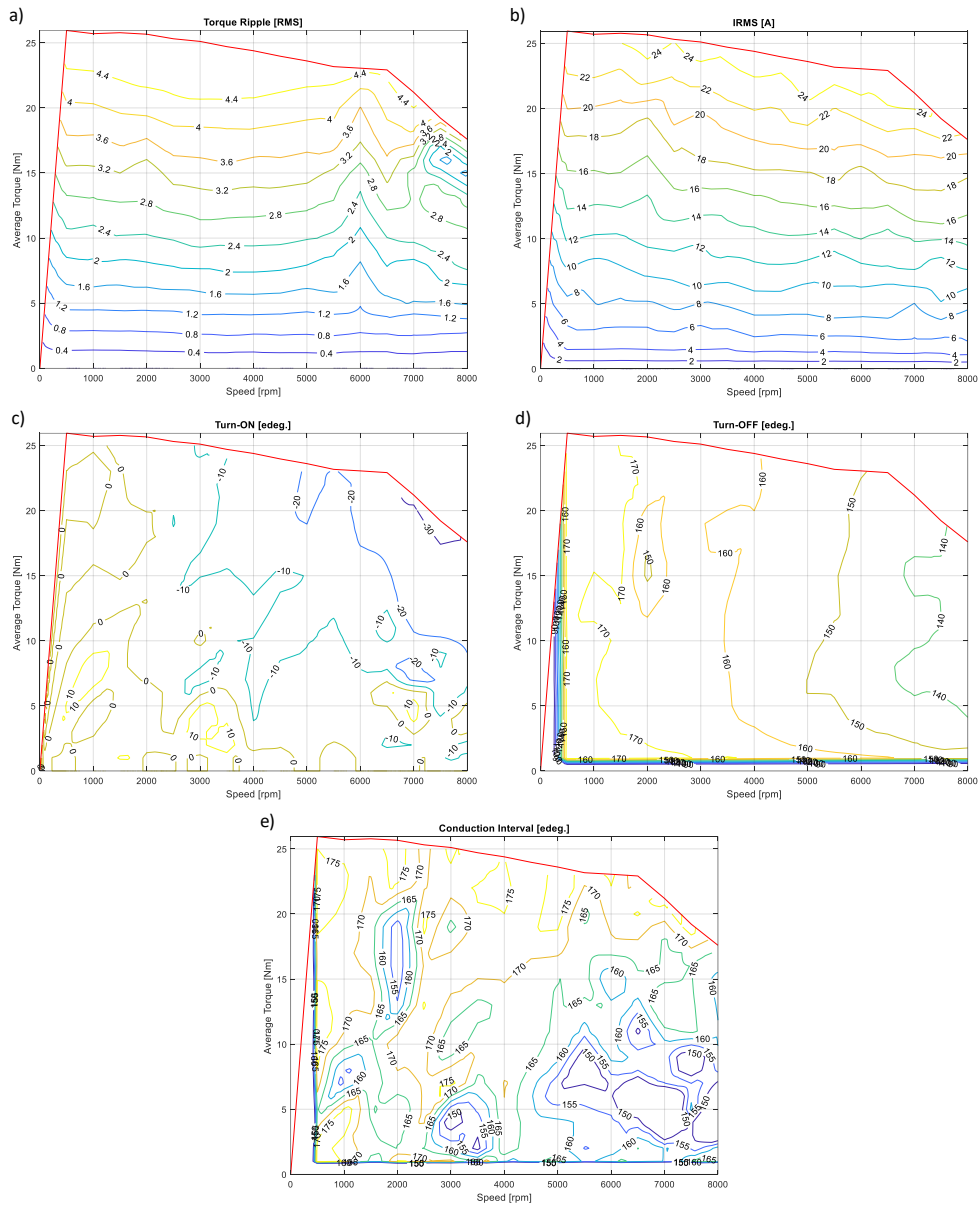
Fig. 4.1: Torque-speed characteristic of an 8/6 SRM in motoring mode using hard-switching with the average torque maximized and torque ripple minimized: (a) torque ripple RMS contour, (b) phase current RMS contour, (c) turn-on angle contour, (d) turn-off angle contour, (e) conduction interval contour.
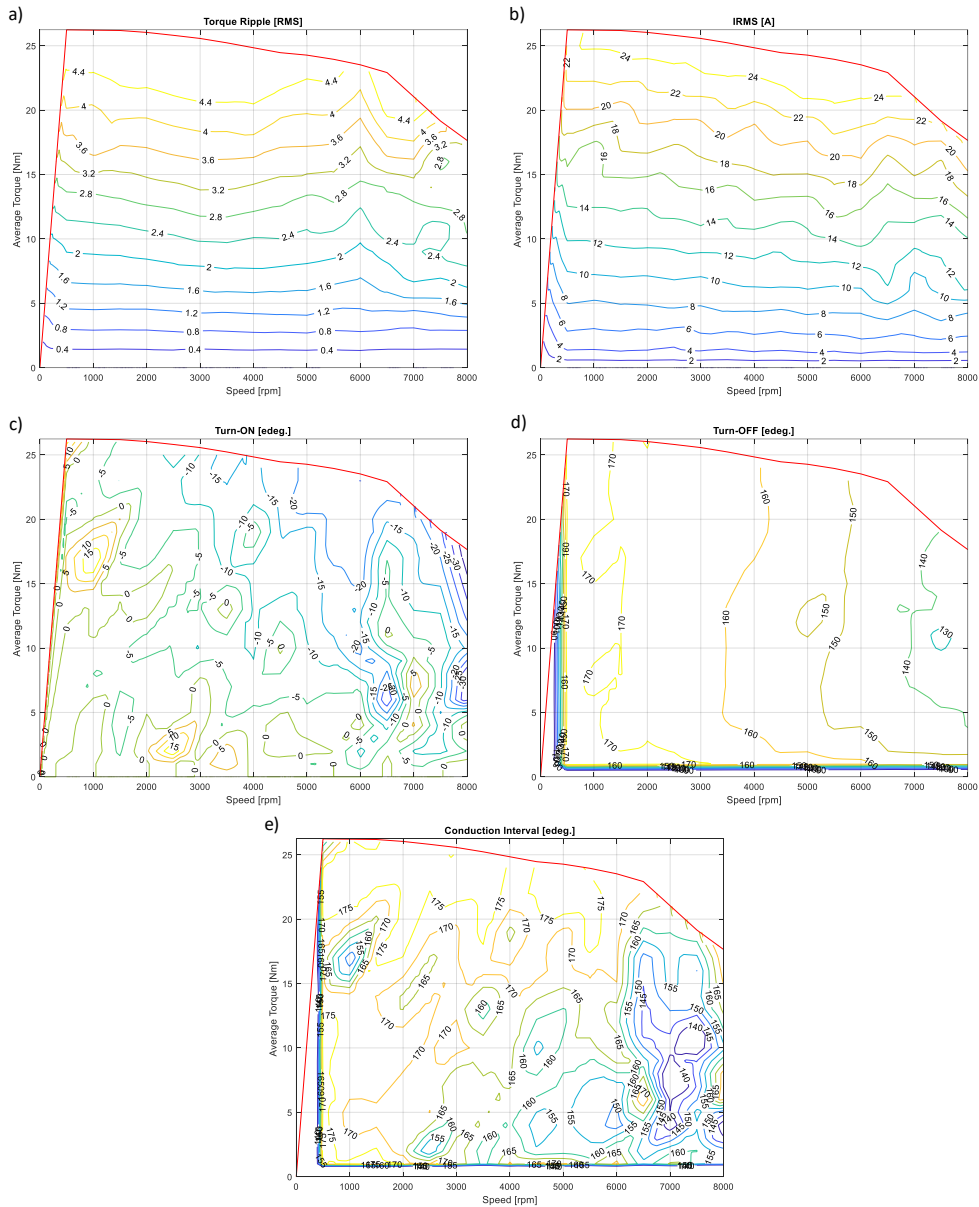
Fig. 4.2: Torque-speed characteristic of an 8/6 SRM in motoring mode using soft-switching with the average torque maximized and torque ripple minimized: (a) torque ripple RMS contour, (b) phase current RMS contour, (c) turn-on angle contour, (d) turn-off angle contour, (e) conduction interval contour.

4.2.2 – Generating Mode

For the generating mode cases, the torque ripple is minimized similar to the motoring mode of operation. Since the torque should be negative in generating mode, the average torque is minimized unlike the motoring mode of operation. The constraints for the optimization are shown in (4.7).

$$
\begin{aligned}
90^o &\leq \theta_{on} \leq 270^o \\
270^o &\leq \theta_{off} \leq 360^o \\
\theta_{off} - \theta_{on} &\geq 90^o \\
\theta_{off} - \theta_{on} &\leq 180^o \\
I_{RMS} &\leq 60\ A
\end{aligned}
\qquad (4.7)
$$

The turn-on conduction angle is constrained between 90 and 270 degrees electrical, and the turn-off conduction angle is constrained between 270 and 360 degrees electrical. The conduction interval and current constraints are kept the same as the motoring mode.

In Fig. 4.3, generating mode with hard-switching is used to optimize the conduction angles. As the absolute average torque increases, the RMS value of torque ripple also increases as shown in Fig. 4.3(a). When the torque-speed characteristics for motoring and generating modes are compared, it can be observed that there is a difference between the torque envelopes. In Fig. 4.1 motoring mode, torque tends to reduce with speed after the base speed of 6000 rpm. In Fig. 4.3 generating mode, torque does not reduce after 6000 rpm. This is because, at the higher speeds in generating mode, the magnitude of the induced voltage is higher than the DC-link voltage. When both voltages are negative, the larger magnitude of the induced voltage supports the phase current to rise, which draws more torque from the prime mover. This is shown in Fig. 3.40 for single pulse mode of operation

at 8000 rpm. It can be observed that after the turn-off angle, the phase current keeps rising because the magnitude of the induced voltage is higher than the magnitude of the DC-link voltage.

In Fig. 4.3(c) and (d), the optimized turn-on and off angles are shown for generating mode using hard-switching current control. Like the motoring case using hard-switching in Fig. 4.1(c) and (d), as the rotor speed is increased the conduction angles advance to produce the same average torque. In generating mode, the conduction angle advancement is done by the turn-on and off approaching the unaligned and aligned position, respectively. However, the motoring turn-on angle only advances from 10 to -30 degrees electrical, which is smaller than the generating turn-on conduction angle advancing from 170 to 90 degrees electrical. As presented in Fig. 3.5(a) and (b), in generating mode, both the turn-on angle and turn-off angle impacts the peak value of the phase current in single-pulse mode of operation. This results in different contours for conduction angles in motoring and generating modes despite similar objectives were used. This also reflects to the torque ripple contour in generating mode. As shown in Fig. 4.3(a), at speed higher than 4000 rpm and average torque larger than -15 Nm, the RMS value of torque ripple begins to decrease from 3.2 Nm to less than 1.6 Nm in generating mode. In Fig. 4.3(e), the conduction interval for the hard-switching generating case is larger than 175 degrees electrical for majority of the torque-speed envelope. This larger conduction interval reduces the torque ripple magnitude but also contributes to an increase in the copper loss as the RMS value of phase current is being maximized.
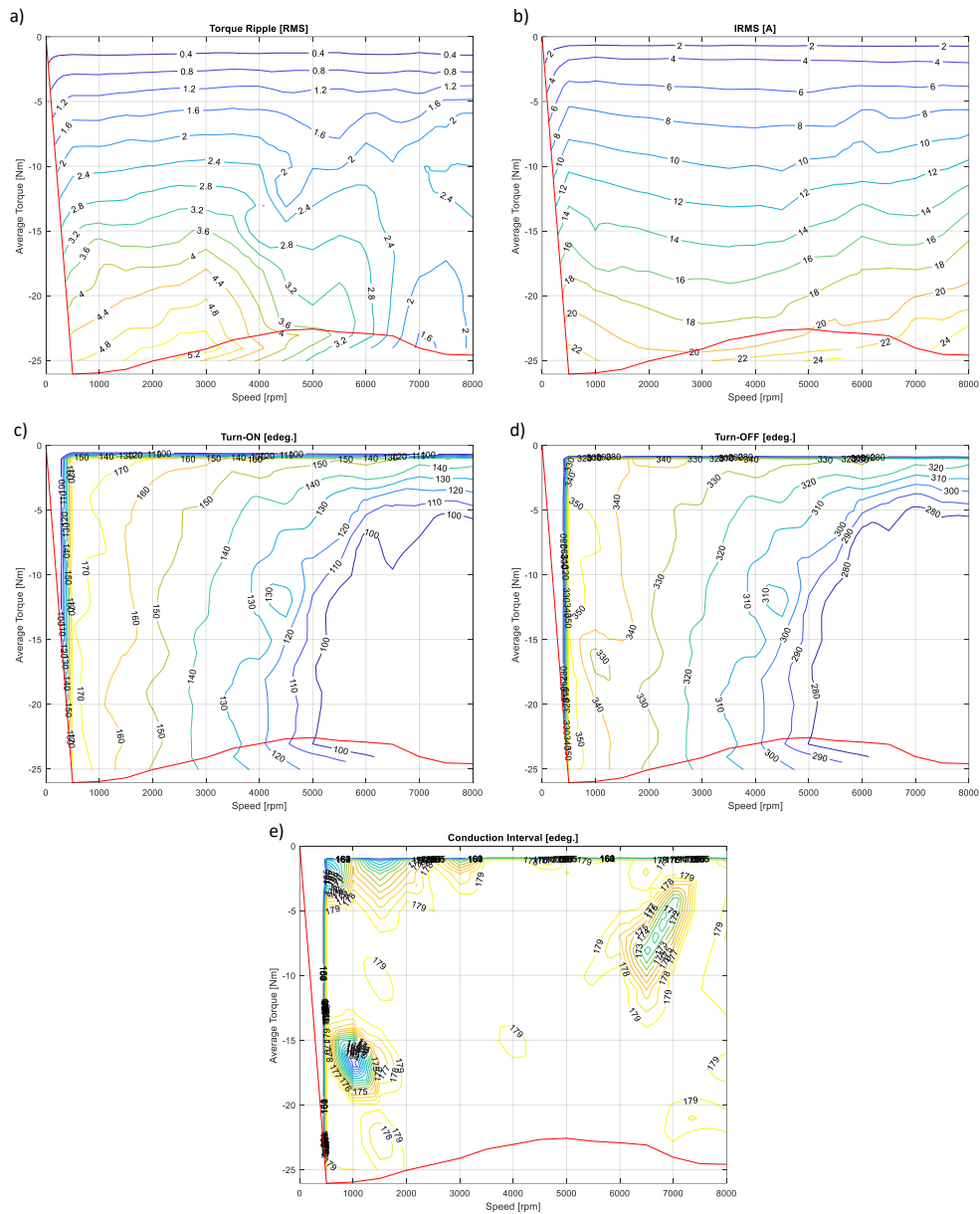
Fig. 4.3: Torque-speed characteristic of an 8/6 SRM in generating mode using hard-switching with the absolute average torque maximized and torque ripple minimized: (a) torque ripple RMS contour, (b) phase current RMS contour, (c) turn-on angle contour, (d) turn-off angle contour, (e) conduction interval contour.
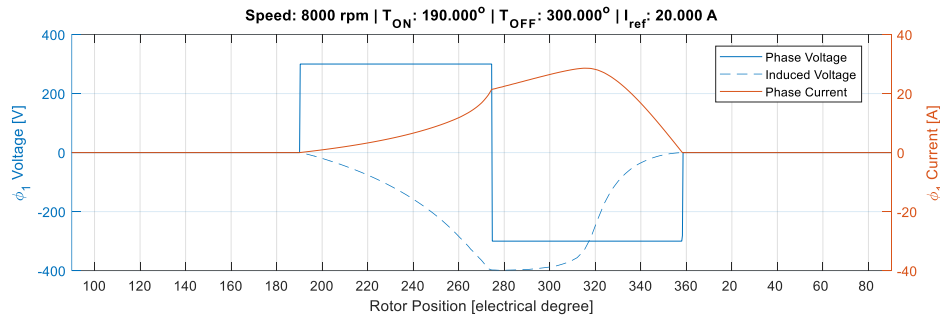
Fig. 4.4: Phase current waveform using hard or soft-switching current control at high speed in generation mode.

In Fig. 4.5, the torque-speed contours are shown for generating mode when using soft-switching current control. The torque-speed envelope is similar for both the soft and hard-switching cases in generating mode. The RMS torque ripple increases as the absolute average torque increases, shown in Fig. 4.6(a). But when compared to hard-switching in Fig. 4.3(a) for the same torque-speed points, the RMS torque ripple in the soft-switching case is slightly lower. When the conduction angle contours are compared for soft-switching (Fig. 4.5(c) and (d)) and hard-switching (Fig. 4.3(c) and (d)), it can be observed that the contours are largely similar. The slight differences in the conduction angle contours results in the difference in torque ripple for these two cases. In Fig. 4.5(b), the phase current observed in soft-switching is similar in magnitude for majority of the points observed in hard-switching generating mode. Only at speeds higher than 6000 rpm the soft-switching case has marginally lower phase current by 0.5 to 1 A. Similar to the hard-switching case, the soft-switching conduction interval is also larger than 175 degrees electrical for majority of the torque-speed envelope.
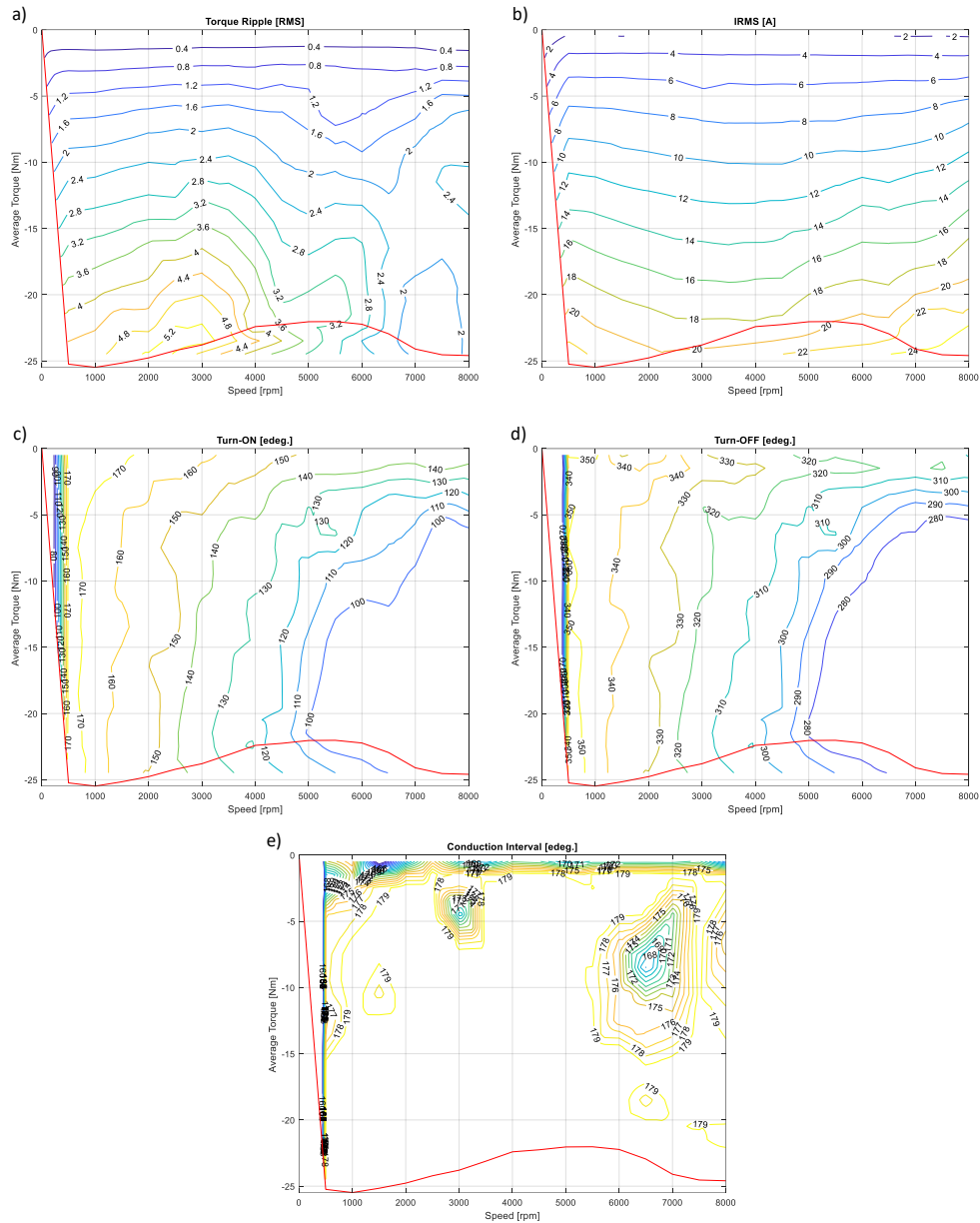
Fig. 4.5: Torque-speed characteristic of an 8/6 SRM in generating mode using soft-switching with the absolute average torque maximized and torque ripple minimized: (a) torque ripple RMS contour, (b) phase current RMS contour, (c) turn-on angle contour, (d) turn-off angle contour, (e) conduction interval contour.

Maximizing the absolute value of average torque and minimizing the torque ripple using multi-objective optimization to select the conduction angles does not specifically improve the generating mode performance as the objectives are more

specific to the motoring mode operation. It can be concluded that the optimization objectives need to be updated to specifically improve the generating mode performance, by maximizing the amount of power sent back to the source.

4.3 – Selecting Optimization Objectives Specific to Generating Mode Operation

To determine optimization objectives to improve generating mode performance, an exhaustive search needs to be carried out first. In this section, generating mode is explored using soft-switching, with the hysteresis controller presented in (3.5). Moving forward, similar analysis is not conducted for hard switching, as the performance of hard and soft-switching has been mostly similar for the objectives explored so far. Besides, soft-switching can help improve current harmonics, and reduce the conduction and switching losses.

The exhaustive search for conduction angles is conducted for a selected current reference and rotor speed. Then, all potential turn-on and turn-off conduction angles are investigated to map out the specific objectives to be explored. For the exhaustive search, an additional model constraint needs to be considered for generating mode. In the optimization constraints for generating mode in (4.7), the turn-off angle is limited from 180 to 360 degree electrical. Ideally, the generating mode turn-off constraint might need to be expanded to ensure that delayed conduction does not improve generating mode capability. In Section 4.2, it was observed that both the motoring and generating mode optimizations advance the conduction period at higher speeds. This makes sense specifically for motoring

mode as higher speed operation results in higher induced voltage, which results in lower rate of change of current and, hence, lower peak current. In generating mode, as the rotor speed increases, the magnitude of the induced voltage becomes higher than the magnitude of the DC-link voltage after the turn-off angle is applied as shown in Fig. 4.4. Unlike the motoring mode, this results in an increase in the rate of change in current. For this reason, extending the conduction angle constraints can help verify whether generating mode can take advantage of delayed conduction especially for high-speed operation. Therefore, the exhaustive search is completed using (4.8), and the minimum and maximum conduction interval constraints in (4.7) of 90 and 180 degrees electrical are removed.

$$90^o \leq \theta_{on} \leq 270^o$$
$$270^o \leq \theta_{off} \leq 450^o \qquad (4.8)$$

The exhaustive search is done for soft-switching current control for generating mode at 5000 rpm with a current reference of 20 A, as shown in Fig. 4.6. The exhaustive simulation contours plots show the conduction angles along with shaded regions indicating turn-on and off angle combinations that exceed the constraints in (4.7).

Fig. 4.6(a) shows the average torque contour as a function of turn-on and turn-off angles for the exhaustive search. The highest absolute average torque is when the turn-on angle is between 90 and 125 degrees electrical and turn-off angle is near the unaligned position (360 degrees electrical). Also, the highest absolute average torque is in the region where the conduction interval is larger than 180 degrees electrical. Fig. 4.6(b) shows the torque ripple RMS contour. The highest

torque ripple occurs around when the turn-on angle is 245 degrees electrical and turn-off angle is around 315 degrees electrical. The highest RMS torque ripple occurs in a region where the conduction period is less than 90 degrees electrical. In Fig. 4.6(c), the average source current contour is shown. The highest average source current provided back to the supply occurs at the same point where the highest absolute average torque occurs.
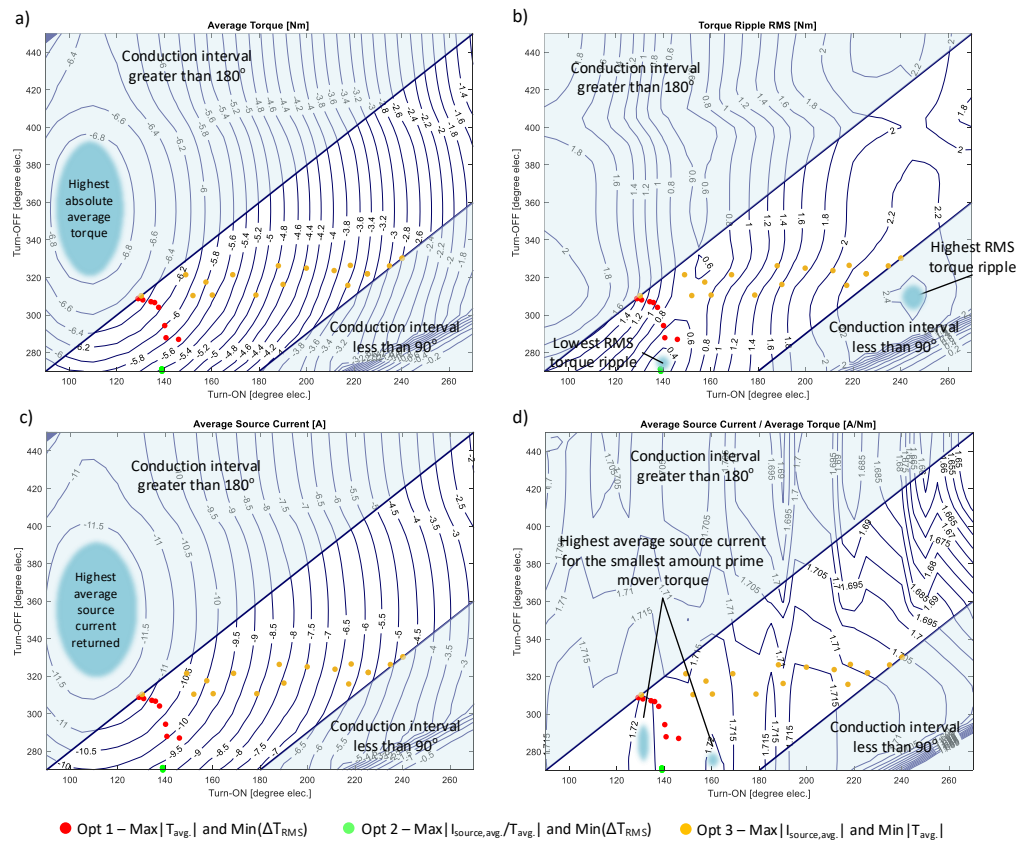
Fig. 4.6: Exhaustive simulation result at 5000 rpm and 20 A reference using soft-switching current control in generating mode with: (a) average torque, (b) torque ripple RMS, (c) average source current, (d) average source current per torque.

An additional measurement contour is plotted by combining the average source current divided by the average torque, as shown in Fig. 4.6(d). This was done to minimize the total number of optimization objectives from three to two. By

using the average source current divided by the average torque as the first objective

and torque ripple RMS as the second objective, the optimizer can consider all three

objectives but not independently.

In generating mode, it is essential to improve the amount of power supplied

to the source for the smallest absolute average torque drawn from the prime mover.

This generating specific objective is different to the objectives used in motoring

mode such as maximum average torque per phase current RMS. The new

generating specific optimization objective can be expressed as:

$$Obj_4 = \frac{I_{source,avg}}{T_{avg}}$$
(4.9)

where $I_{source,avg}$ is the average source current, and T_{avg} is the average torque. From

Fig. 4.6(d), it can be seen that Obj_4 is maximum at the early turn-on and turn-off

angles and does not occur at the points where the absolute average torque and

source currents are maximum. The region where the maximum absolute average

torque and source current occur is where the conduction interval is larger than 180

degrees electrical as shown in Fig. 4.6(a) and (b). However, in Fig. 4.6(d), the

maximum value of Obj_4 appears in a region where the conduction interval is within

the constraints presented in (4.7). Additionally, the minimum RMS value of torque

ripple occurs relatively close to where Obj_4 is maximum. This implies that, if a

multi-objective optimization is to be used involving Obj_4 and torque ripple, a much

smaller Pareto front can be created.

In Fig. 4.6, there are scatter points on all exhaustive search contour plots to

show the trends for different optimization objectives. The red points (Opt 1)

represent conduction angles when the multi-objective optimization is carried out for the objectives: (i) maximizing the absolute average torque and (ii) minimizing the torque ripple. These objectives are similar to the motoring mode of operation. For the red points, the conduction constraints in (4.8) are utilized which enable delaying the turn-off angle beyond unaligned position. When observing the optimization results in Fig. 4.6(a) and (b) shown with the red points, the turn-on and turn-off angles are distributed between the two regions where the absolute average torque is maximized and torque ripple is minimized, confirming the optimizer is functioning correctly.

In Fig. 4.6, the green points (Opt 2) represent the new generating-mode-specific optimization objectives: (i) maximizing the average source current per absolute average torque and (ii) minimizing the torque ripple. With these objectives, the results are far more concentrated to one set of conduction angles. When observing the green points in Fig. 4.6(b) and (d), the torque ripple is minimized while the average source current per average torque is maximized. The new optimization objectives in Opt 2 essentially extract and return the most amount of source current for the smallest absolute average torque and minimize the torque ripple while doing so. This is important in a generating scenario. For example, if an SRM is to be used as an automotive alternator, it is responsible for charging the vehicle battery using the engine power when in generating mode. It is essential that the maximum amount of power is returned to the battery while not extracting too much engine torque, as the primary goal of the engine is to provide torque for vehicle propulsion.

Selecting optimization objectives for generating mode is not trivial and does not always lead to converging solution which creates a usable Pareto front between the two selected optimization objectives. In Fig. 4.6, the orange points (Opt 3) represent conduction angle points which are obtained using optimization objectives: (i) minimizing the absolute average torque and (ii) maximizing the source current. These objectives tend to maximize the source current per average torque but in two independent objectives in a multi-objective optimization. However, the orange points in Opt 3 in Fig. 4.6 create a Pareto front between the conduction period limitation represented in (4.7) for the two objectives. Furthermore, the Pareto front is broad due to the solutions being on the polar ends of the conduction angle range making it far more difficult to chose working conduction angles. The large Pareto front is created between the two objectives consisting of 20 working conduction angle conditions and the GA optimizer's initial population size was also 20. This means that each initial point converged to a unique solution between the two objectives. However, the optimization ignores the torque ripple RMS consideration, which results in all the working conditions being selected between the two objectives to have significant torque ripple compared to the optimization results found earlier.

Notably, the source current, absolute average torque, and torque ripple all need to be considered in generating mode. As it would be a lot more challenging to find a solution from a Pareto front with three separate objectives, the most effective optimization results were obtained by maximizing the average source current per absolute average torque and minimizing the torque ripple.

4.4 – Proposed Optimization to Maximize Source Current Per Torque and Minimize Torque Ripple

In this chapter the multi-objective optimizer is used to generate conduction angles for the new objectives specific to generating mode. The optimizer maximizes average source current per average torque and minimizes torque ripple.

4.4.1 – Generating Mode using Hard-Switching with Proposed Optimization

The optimization was carried out using the same generating mode constraints but with expanded turn-off angle shown in (4.10), and for the same speed and current reference case in Section 4.2.2.

$$
\begin{aligned}
90^o &\leq \theta_{on} \leq 270^o \\
270^o &\leq \theta_{off} \leq 450^o \\
\theta_{off} &- \theta_{on} \geq 90^o \\
\theta_{off} &- \theta_{on} \leq 180^o \\
I_{RMS} &\leq 60\ A
\end{aligned}
\tag{4.10}
$$

In Fig. 4.7, torque-speed contours are shown for the proposed optimization objectives (Opt 2) using hard-switching. With the Opt 2 optimization objectives, the average torque envelope is different, when compared to the original multi-objective optimization (Opt 1) of $\max|T_{avg}|$ and $\min(\Delta T_{RMS})$ in Fig. 4.3. The constant torque region has a lower absolute average torque of -18 Nm compared to -25 Nm. This change in envelope is due to the optimizer looking for conduction angles that result in the most amount of source current sent back to the source for the smallest amount of prime mover torque. Beyond the constant torque region, the torque production begins to increase as the single pulse control begins to dominate. As it is shown was Fig. 4.4, after the turn-off angle at higher speed operation, the

magnitude of the induced voltage being higher than the magnitude of the DC-link voltage helps increase the current peak value and drawing more torque from the prime mover.

When observing Fig. 4.7(a), the RMS value of torque ripple has been greatly reduced when compared to the previous optimization objectives (Opt 1) in Fig. 4.3(a). The highest torque ripple RMS observed within the constant torque region is 1.4 Nm as opposed to the 5.2 Nm in Fig. 4.3(a). The torque ripple performance is equal or slightly higher for speeds beyond the constant torque range (higher than 6000 rpm). In Fig. 4.7(b), the phase current RMS is shown for hard-switching. As the proposed optimizer looks to reduce the absolute average torque, this results in a lower phase current RMS when compared to the previous optimization objectives (Opt 1) in Fig. 4.3(b). For example, in Fig. 4.3(b) at 5000 rpm and -15 Nm_{avg}, 14 A_{RMS} of phase current was drawn. With the proposed optimization objectives (Opt 2), 12 A_{RMS} was drawn which is a 14.28 % decrease. In Fig. 4.7(c) and (d), the turn-on and turn-off angle contours are plotted for the Opt 2 optimization objectives. As the rotor speed increases, the conduction angles advance due to the turn-on and off conductions angles approaching the unaligned and aligned positions, respectively. The conduction interval advances despite the optimizer allowing for a much wider turn-off constraint. In Fig. 4.7(e), the average source current is plotted using the new optimization objectives. The source current tends to increase with rotor speed and as more torque is used from the prime mover. Additionally, in Fig. 4.7(f) the proposed optimization objectives (Opt 2) result in the conduction interval starting from 90 degrees electrical for low-speeds and expanding to 180 degrees electrical

for high-speeds to minimize torque ripple. The older optimization objectives (Opt

1) maximized the conduction interval for the entire torque-speed range contributing

to a higher RMS value of phase current, shown in Fig. 4.3(e).
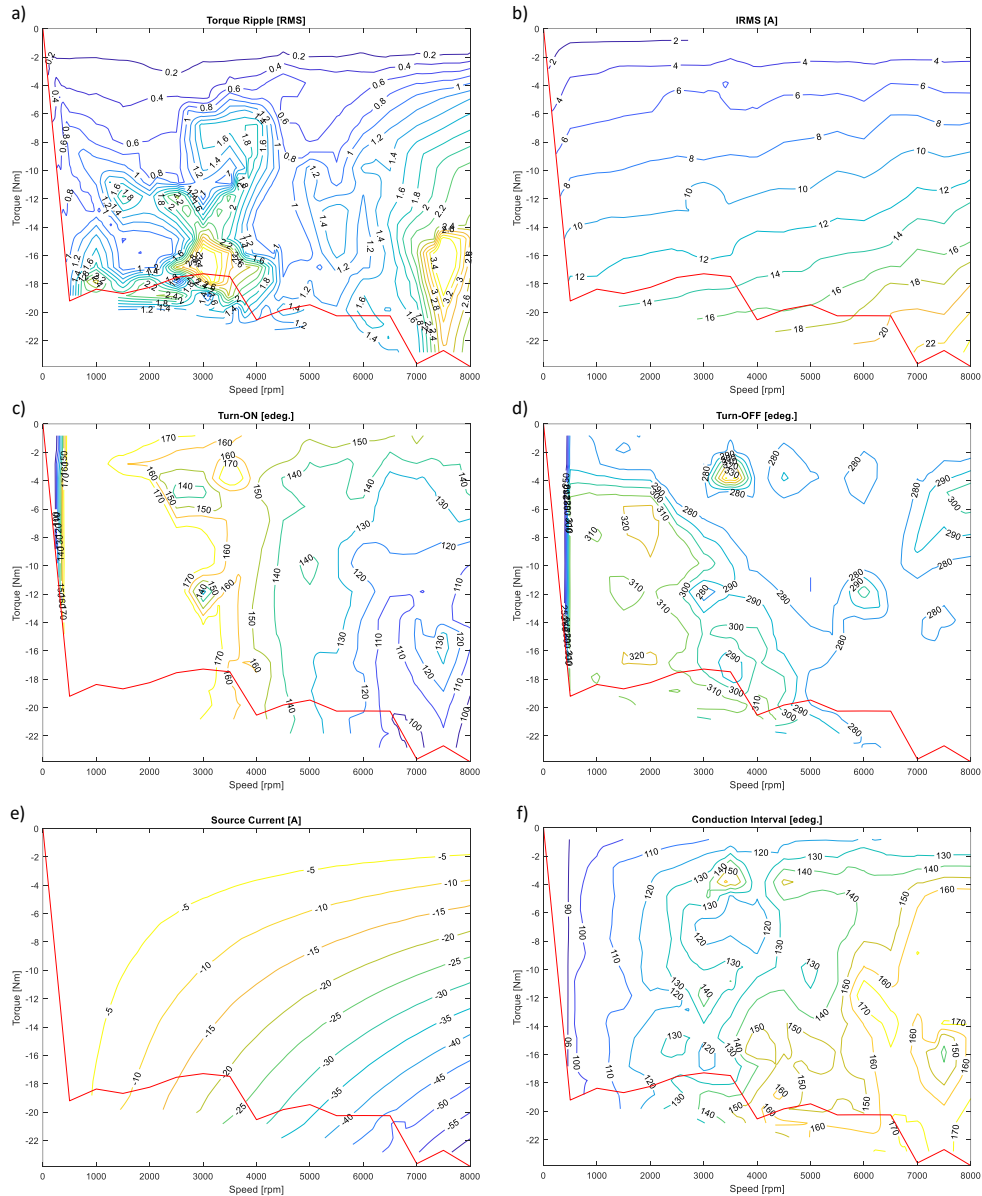
Fig. 4.7: Torque-speed characteristic of an 8/6 SRM in generating mode using hard-switching with the average source current per torque maximized and torque ripple minimized: (a) torque ripple RMS contour, (b) phase current RMS contour, (c) turn-on angle contour, (d) turn-off angle contour, (e) average source current contour, (f) conduction interval contour.

95

4.4.2 – Generating Mode Soft-Switching with Proposed Optimization

The same optimization for the objectives of maximizing average source current per average torque and minimizing RMS value of torque ripple are applied to the generating mode using soft-switching. Similar to the case for hard-switching, the soft-switching torque-speed envelope has changed when compared to the Opt 1 optimization, in Fig. 4.8(a). The maximum torque in the constant torque region is lower when compared to the older optimization (Opt 2) in Fig. 4.5(a) for the objectives of maximizing absolute average torque and minimizing RMS value of torque ripple. In Fig. 4.8(b), the phase current contours are shown. The difference between hard and soft-switching for the RMS value of the phase current is small when comparing Fig. 4.7(b) and Fig. 4.8(b). However, the RMS phase current reduced from 14 to 12 A using the proposed optimization objectives (Opt 2) compared to the old optimization objectives (Opt 1) using soft switching in Fig. 4.5(b); for the same torque-speed point of 5000 rpm and -14 Nm.

In Fig. 4.8(c) and (d), the turn-on and off contours are plotted for soft-switching using the new optimization objectives. Similar to all of the optimization cases done prior, both the turn-on and off conduction angles advance by approaching the unaligned and aligned positions, respectively. The conduction angles advance despite the proposed optimization objectives (Opt 2) using the constraints found in (4.8). The constraints expand the turn-off conduction angle range to 270 and 450 degrees electrical, allowing for a delayed conduction interval. Additionally, the Opt 2 optimization objectives do not advance turn-on and off conduction angles significantly until higher operating speeds. As opposed to Opt 1

optimization objectives, which had the conduction angles advance at lower speeds instead. This is because the maximum source current per torque and minimum torque ripple points occur around 130 and 290 degrees electrical for the turn-on and off conduction angles, as shown in Fig. 4.6(c) and (d). The proposed optimization objectives stay within that conduction region while the SRM operates in the constant torque region. This maximizes the fitness function associated with the two objectives. At higher speeds, the phase current behaviour is the same as single pulse mode due to the DC-link and induced voltage relation. This results in the optimizer to then advance the conduction angles to achieve the proposed generating specific objectives, as the earlier turn-on angle contributes to a higher current magnitude.

In Fig. 4.8(e), the average source current contours are shown using the new optimization objectives. As the absolute average torque and rotor speed increase, the source current supplied back increases. In Fig. 4.8(f), the conduction interval expands as the rotor speed increases to maintain torque ripple performance, similar to the hard-switching case. The reduction in conduction interval results in the RMS value of phase current to be lower for the Opt 2 objectives when compared to Opt 1 objectives for majority of the torque-speed envelope.
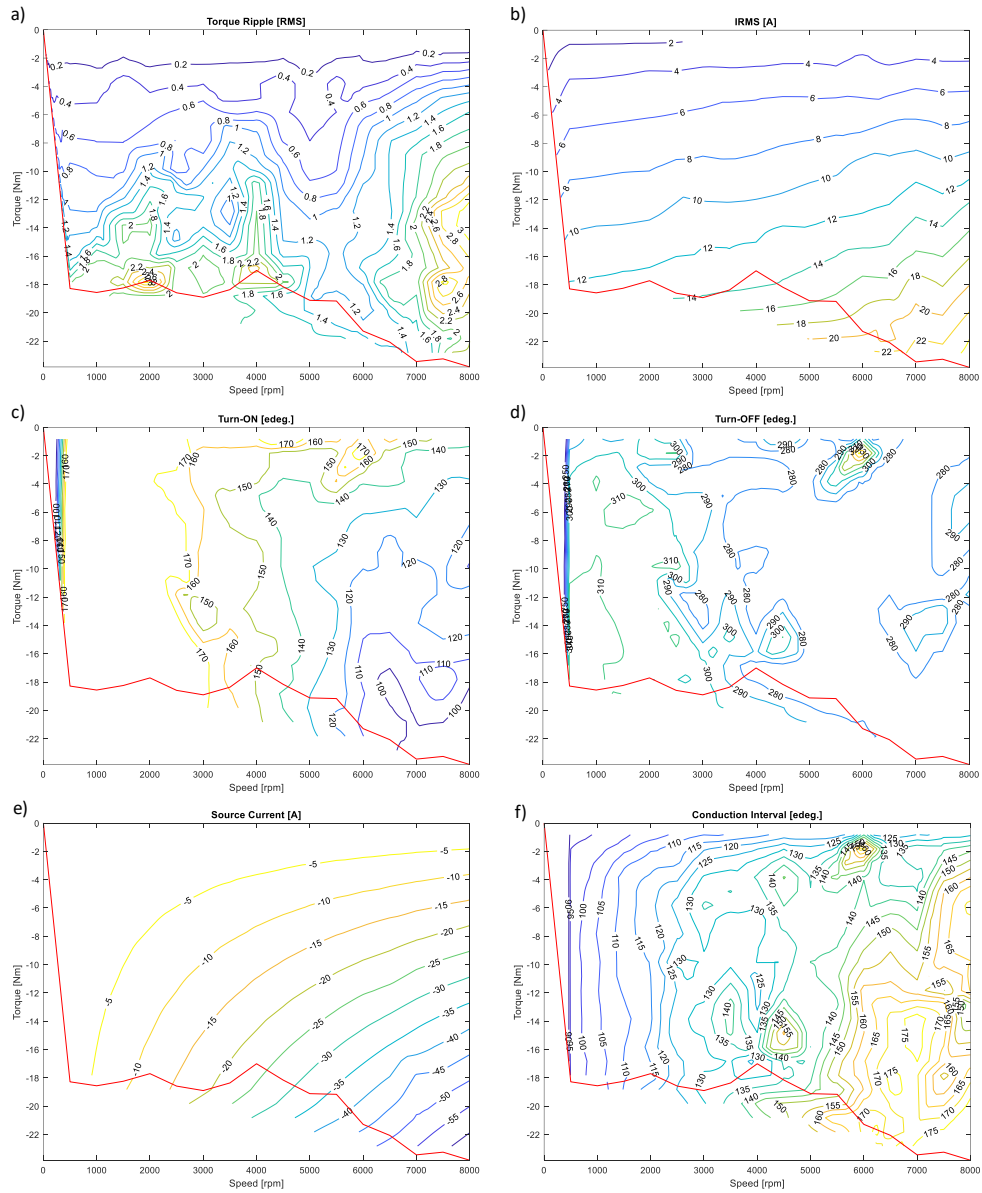
Fig. 4.8: Torque-speed characteristic of an 8/6 SRM in generating mode using soft-switching with the average source current per torque maximized and torque ripple minimized: (a) torque ripple RMS contour, (b) phase current RMS contour, (c) turn-on angle contour, (d) turn-off angle contour, (e) average source current contour, (f) conduction interval contour.

4.4.3 – Comparing Generating Mode Performance with Hard-Switching

Using the Proposed Optimization

To compare the performance and the dynamic waveforms for the proposed generating specific optimization objectives, the operating point of 20 A current reference and 4000 rpm is used in generating mode of operation.

Fig. 4.9 compares the older optimization objectives (Opt 1) of $\max|T_{avg}|$ and $\min(\Delta T_{RMS})$ to the proposed optimization objectives (Opt 2) of $\max|I_{source,avg}/T_{avg}|$ and $\min(\Delta T_{RMS})$. For Opt 1, the optimizer generates a Pareto front for the two objectives. In Fig. 4.9, two cases were selected from the Pareto front for Opt 1. The waveforms in blue show the results for Opt 1 when the objective $\max|T_{avg}|$ is given priority. The waveforms in red show the results for Opt 1 when the objective $\min(\Delta T_{RMS})$ is given priority.

In Fig. 4.9(a), the electromagnetic torque is plotted for the original multi-optimization objectives (Opt 1) and proposed multi-optimization objectives (Opt 2). Opt 1 which maximizes absolute average torque (blue line) has significant torque ripple but a higher absolute average torque magnitude when compared to the other waveforms. With Opt 2 (orange line) being closer in magnitude and ripple to Opt 1 which prioritizes torque ripple performance (red line). In Fig. 4.9(b), the proposed optimization (Opt 2) phase current matches the older optimization (Opt 1) where the torque ripple minimization was given priority (red line with bolded $\min(\Delta T_{RMS})$ objective in Fig. 4.9) which will result in a smaller phase current RMS. In Fig. 4.9(c), the source current is plotted with the proposed optimization.

a)

b)

c)
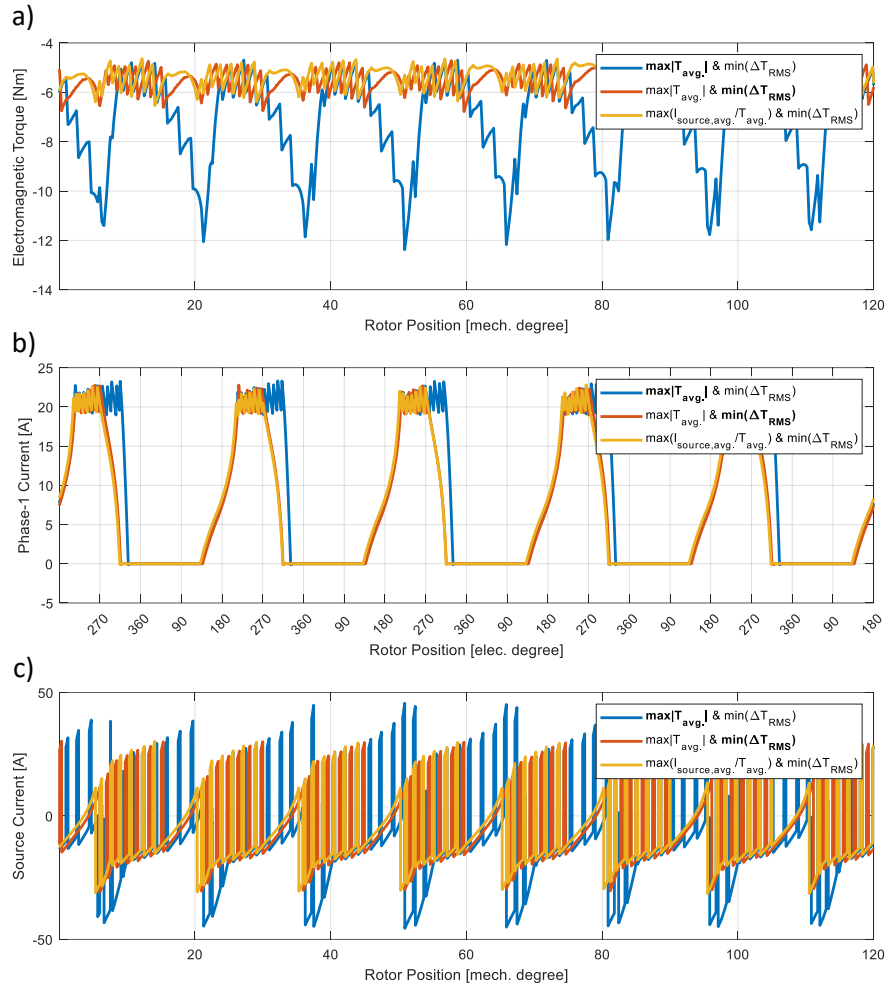
Bolded objective represents optimization results favoring a specific objective.

Fig. 4.9: Generating mode hard-switching results at 20 A and 4000 rpm for (a) electromagnetic torque (b) phase current (c) source current.

In Table 4.1, the optimization objectives of $\max|T_{avg}|$ and $\min(\Delta T_{RMS})$ are compared to the proposed optimization objectives of $\max|I_{source,avg}/T_{avg}|$ and $\min(\Delta T_{RMS})$ for 20 A current reference and 4000 rpm rotor speed. The proposed optimization improves the amount of source current per torque extracted compared to the older optimization objectives. Additionally, the proposed optimization (Opt 2) draws 3.02 % less mechanical power when compared to Opt 1 with the torque ripple objective given priority, but only results in a 1.73 % reduction in the supplied

electrical power. Furthermore, Opt 2 also has a 1.96 % reduction in the RMS phase current when compared to Opt 1 with the torque ripple objective given priority. The proposed optimization (Opt 2) finds working conduction angles with less variation when compared to the older objectives (Opt 1) which have multiple broad solutions.

Table 4.1: Comparison of optimization results at 20 A and 4000 rpm using hard switching in generating mode (bolded optimization objective is given priority).

Optimization objectives	Opt 1: $\mathbf{max}\lvert T_{avg}\rvert$ and $min(\Delta T_{RMS})$	Opt 1: $max\lvert T_{avg}\rvert$ and $\mathbf{min}(\Delta T_{RMS})$	Opt 2: $max\lvert I_{source,avg}/T_{avg}\rvert$ and $min(\Delta T_{RMS})$
RMS phase current [A]	8.034	6.479	6.606
Average torque [Nm]	-7.122	-5.532	-5.379
Torque ripple RMS [Nm]	1.892	0.413	0.369
Average source current [A]	-9.752	-7.532	-7.377
Source current per torque [A/Nm]	1.369	1.362	1.371
Average mechanical power [kW]	2.98	2.32	2.25
Average electrical power [kW]	2.971	2.260	2.221

4.4.4 – Comparing Generating Mode Performance with Soft-switching Using the Proposed Optimization

In Fig. 4.10, the original objectives of $max\lvert T_{avg}\rvert$ and $min(\Delta T_{RMS})$ are compared to the proposed optimization objectives of $max\lvert I_{source,avg}/T_{avg}\rvert$ and $min(\Delta T_{RMS})$ but for the soft-switching current control.

In Fig. 4.10(a), the proposed optimization objectives result in lower torque ripple. Additionally, it results in a solution that does not have large variation in conduction angles that transform the motor dynamic performance. The large

variation in conduction angles is shown for the $\max|T_{avg}|$ and $\min(\Delta T_{RMS})$ with

the blue and red lines. In Fig. 4.10(b), the phase current performance is shown.

Similar to the hard switching case, the proposed optimization (Opt 2) reduces the

conduction interval which reduces the RMS phase current. In Fig. 4.10(c), the

source current is plotted to compare the multi-objective optimizations. The source

current from the Opt 2 proposed optimization is equivalent to the Opt 1 older

optimization that prioritized the minimization of torque ripple.
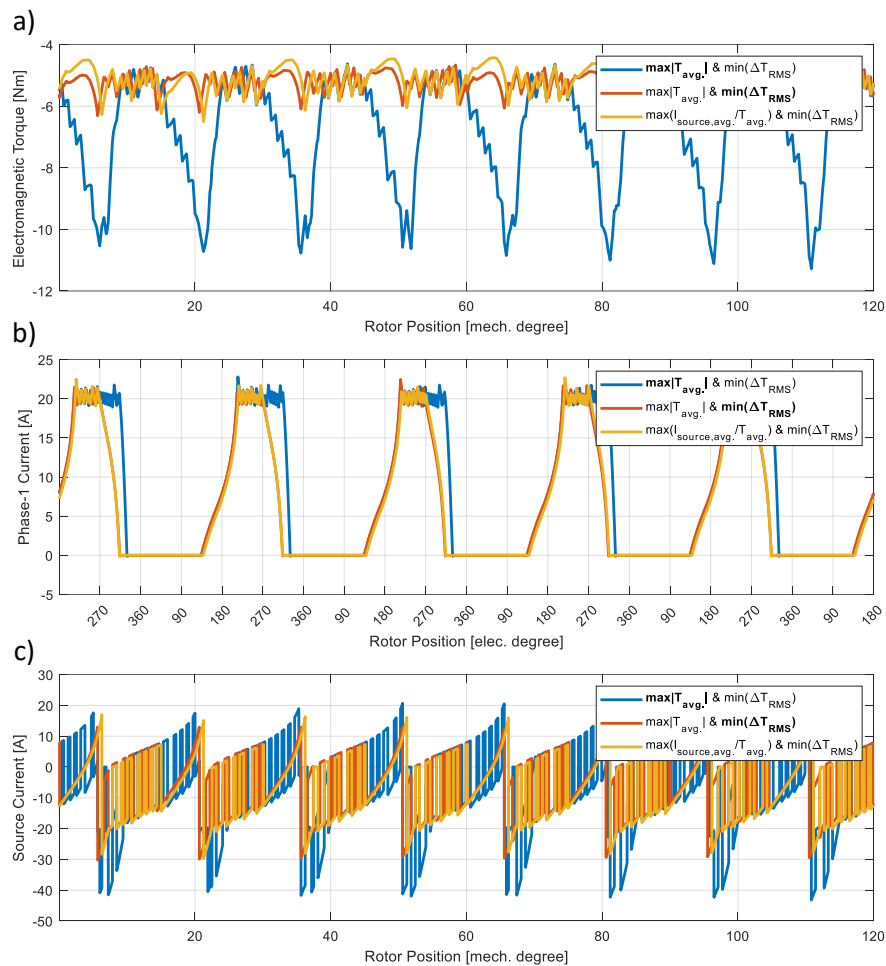
Bolded objective represents optimization results favoring a specific objective.

Fig. 4.10: Generating mode soft-switching results at 20 A and 4000 rpm for (a) electromagnetic torque (b) phase current (c) source current.

In Table 4.2, the optimization objectives of $\max|T_{avg}|$ and $\min(\Delta T_{RMS})$ are compared to the proposed optimization objectives of $\max|I_{source,avg}/T_{avg}|$ and $\min(\Delta T_{RMS})$ for 20 A current reference and 4000 rpm rotor speed. The proposed multi-objective optimization results in the highest average source current per average torque. The proposed optimization Opt 2 results in a 1.38 % reduction in the mechanical power drawn when compared to Opt 1 in which torque ripple is prioritized, and a 1.45 % reduction in the electrical power supplied. In this case, Opt 2 results in marginally less electrical power supplied, but reduces the RMS phase current by 2.36 %. Similar, to the hard-switching case the improvement is small, but the Opt 2 also converges to a smaller set of working conduction angles that specifically improve the SRM generating mode performance.

Table 4.2: Comparison of optimization results at 20 A and 4000 rpm using soft-switching in generating mode (bolded optimization objective is given priority).

Optimization objectives	Opt 1: $\mathbf{max}\|\boldsymbol{T_{avg}}\|$ and $\min(\Delta T_{RMS})$	Opt 1: $\max\|T_{avg}\|$ and $\mathbf{min}(\boldsymbol{\Delta T_{RMS}})$	Opt 2: $\max\|I_{source,avg}/T_{avg}\|$ and $\min(\Delta T_{RMS})$
RMS phase current [A]	7.815	6.365	6.215
Average torque [Nm]	-6.782	-5.198	-5.129
Torque ripple RMS [Nm]	1.781	0.275	0.380
Average source current [A]	-9.297	-7.123	-7.038
Source current per torque [A/Nm]	1.371	1.370	1.372
Average mechanical power [kW]	2.84	2.18	2.15
Average electrical power [kW]	2.786	2.144	2.113

4.4.5 – Comparing Generating Mode Performance Using the Proposed

Optimization at High-speed Operation

In Fig. 4.11, the old optimization objectives (Opt 1) of $\max|T_{avg}|$ and $\min(\Delta T_{RMS})$ to the proposed optimization objectives (Opt 2) of $\max|I_{source,avg}/T_{avg}|$ and $\min(\Delta T_{RMS})$ are compared at 8000 rpm and 20 A current reference. Also, at higher speeds the $\max|T_{avg}|$ and $\min(\Delta T_{RMS})$ optimization (Opt 1) results in a smaller Pareto front where the difference in the two variable performance is minimal, resulting in one set of conduction angles being compared to Opt 2.

In Fig. 4.11(a), the torque behaviour is shown, with the highest absolute average torque observed for the $\max|T_{avg}|$ and $\min(\Delta T_{RMS})$ case. In Fig. 4.11(b), the phase current for the two different cases is observed. With the proposed optimization objectives (Opt 2) having a phase current magnitude less than the Opt 1 objectives. In Fig. 4.11(c), the source current behaviour is shown, and the source current has no switching during conduction due to high-speed operation resulting in single pulse operation in generating mode. Both optimization cases result in the source current supplying current back to the source, and never drawing from the source in steady-state operation. This is an important factor in generating mode for an SRM at high-speeds.

In Table 4.3, the high-speed cases are compared numerically. As expected, the proposed optimization objectives of $\max|I_{source,avg}/T_{avg}|$ and $\min(\Delta T_{RMS})$ improve the generating mode performance by reducing the amount of prime mover torque extracted and minimizing the torque ripple when compared to the $\max|T_{avg}|$

and $\min(\Delta T_{RMS})$ objectives. The proposed optimization (Opt 2) also has a slightly higher average source current per average torque value despite returning marginally less source current when compared to Opt 1 objectives. Using Opt 2, the mechanical power is reduced by 13.32 % when compared to Opt 1, and the electrical power is reduced by only 13.15 %. Essentially, the mechanical power drawn is reduced but relatively less when compared to the electrical power supplied back. Additionally, the proposed optimization (Opt 2) reduces the RMS value of phase current by 19.83 % when compared to Opt 1, while generating a smaller Pareto front.
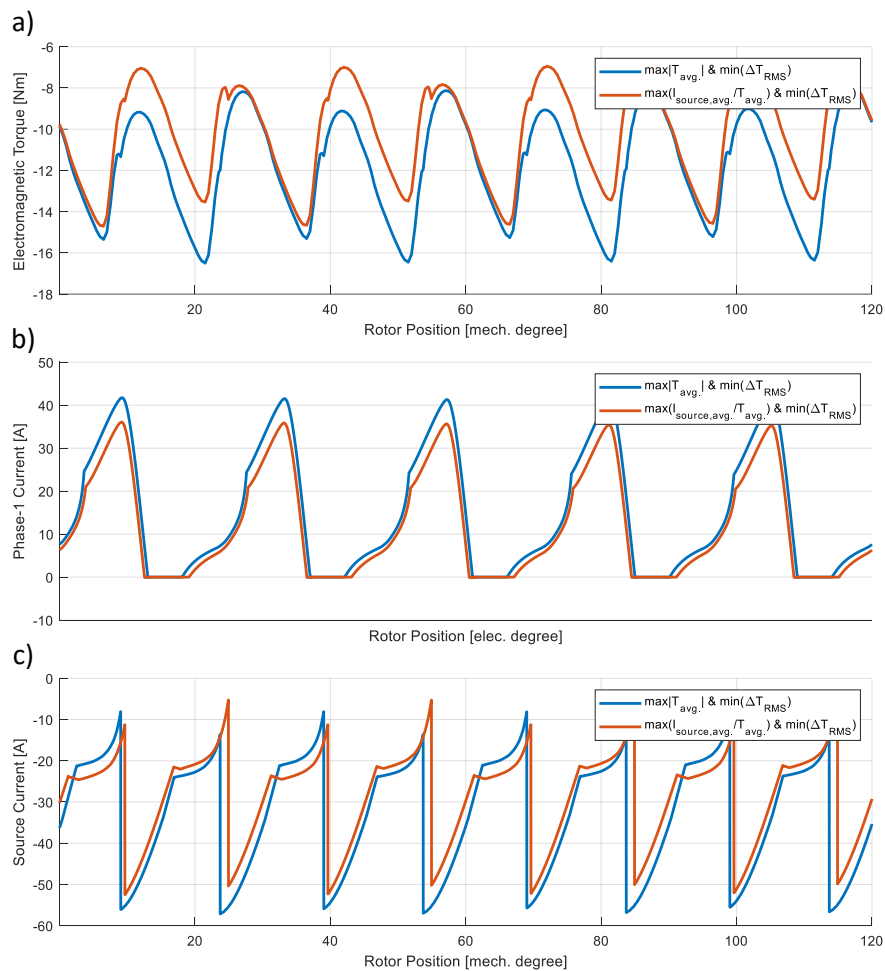
Fig. 4.11: Generating mode soft-switching results at 20 A and 8000 rpm for (a) electromagnetic torque (b) phase current (c) source current.

Table 4.3: Comparison of optimization results at 20 A and 8000 rpm using soft-switching in generating mode.

Optimization objectives	Opt 1: $\max\lvert T_{avg}\rvert$ and $\min(\Delta T_{RMS})$	Opt 2: $\max\lvert I_{source,avg}/T_{avg}\rvert$ and $\min(\Delta T_{RMS})$
RMS phase current [A]	14.730	11.808
Average torque [Nm]	-11.833	-10.252
Torque ripple RMS [Nm]	2.518	2.356
Average source current [A]	-32.637	-28.290
Source current per torque [A/Nm]	2.758	2.759
Average mechanical power [kW]	9.91	8.59
Average electrical power [kW]	9.899	8.598

4.5 – Conclusion

In conclusion, the proposed multi-objective optimization creates working conduction angles specific to the generating mode objectives. Using the exhaustive conduction angle search it was determined that three variables need to be considered for generating mode: average torque, torque ripple RMS, and source current. In generating mode applications, it is critical that the largest amount of current is supplied to the source while the smallest amount of prime mover torque is extracted. This resulted in a new optimization objective of $\max\lvert I_{source,avg}/T_{avg}\rvert$. The remaining objective is $\min(\Delta T_{RMS})$, to reduce the torque ripple. Besides the optimization objectives, the new optimizer constraints also allow for delayed conduction at the turn-off. However, this did not result in the optimizer to perform

delayed conduction because a delayed turn-off angle results in much lower average torque, lower source current, and higher torque ripple.

The $\max\left|I_{source,avg}/T_{avg}\right|$ and $\min(\Delta T_{RMS})$ objective optimization was compared to the $\max\left|T_{avg}\right|$ and $\min(\Delta T_{RMS})$ objective optimization. The proposed optimization in Opt 2 provides conduction angles with less variation in the Pareto front and improve the generating mode performance for all current references and speed ranges. The proposed optimization (Opt 2) results in the $I_{source,avg}/T_{avg}$ objective to be improved while retaining the ΔT_{RMS} performance. Additionally, the proposed optimization (Opt 2) reduces the amount of power extracted from the prime mover when compared to Opt 1, while the electrical power supplied back being marginally lower. The proposed optimization (Opt 2) also reduces the RMS value of phase current when compared to the older optimization objectives (Opt 1), which results in a reduction of copper losses.

Chapter 5. Experimental Setup and Validation

In this section, the development of an experimental dynamometer setup is presented to operate an SRM in four-quadrant operation. The experimental results in generating mode are shown with specific conduction angles using the multi-objective optimizer to improve generation mode performance.

5.1 – Experimental Setup

The experimental setup is used to perform experimental validation of the generating mode optimization scheme. The high-level diagram of the experimental setup is shown in Fig. 5.1.
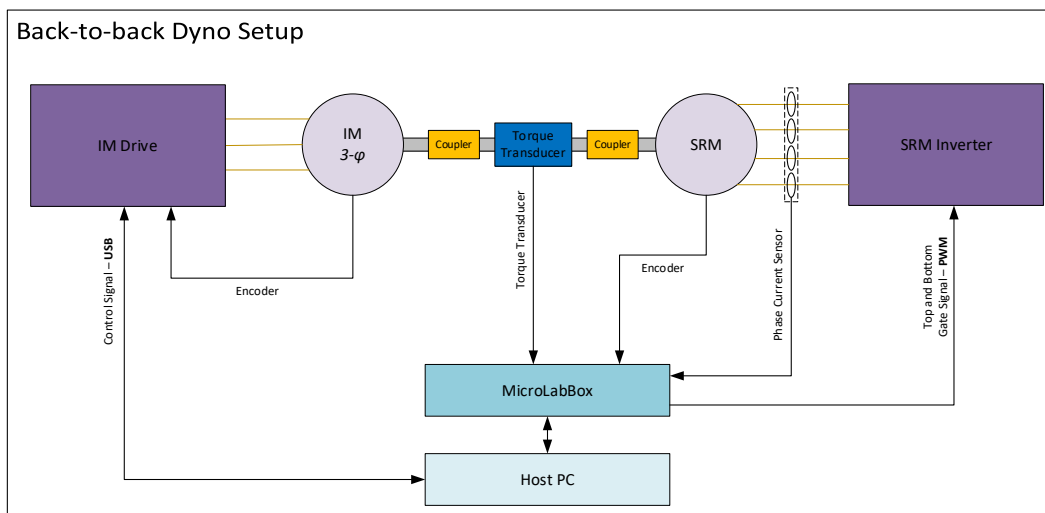
Fig. 5.1: Experimental setup high-level connection diagram.

The setup consists of an SRM and IM coupled through a torque transducer using flexible shaft coupling. The control and power conversion of the IM is provided by a dedicated industrial motor drive and an H-bridge converter for the SRMs excitation. The control of the SRM is provided by the dSpace MicroLabBox

rapid prototyping controller. The rotor position and speed of the SRM is captured by an absolute encoder, and the IMs speed is measured using an incremental encoder. All the sensor feedback is provided to the rapid prototype controller to be processed. The entire setup is completed on a T-slot table as shown in Fig. 5.2.
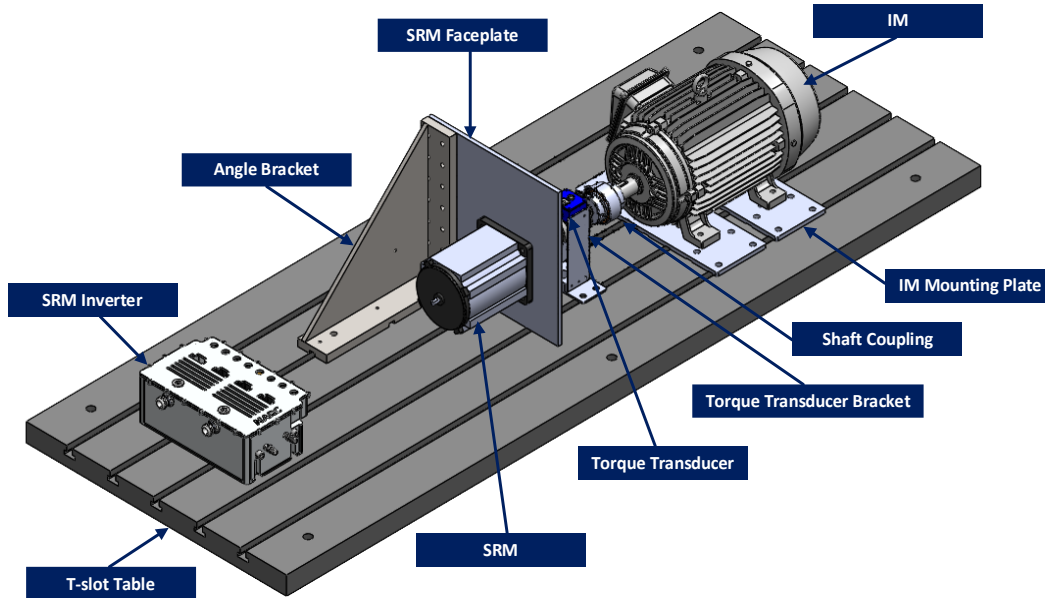
Fig. 5.2: CAD model of experimental setup.

5.1.1 – SRM and Load Induction Machine

For the experimental setup, a 3-phase SRM is used. The SRM key parameters are provided in Table 5.1. The number of rotor poles were determined by exciting a phase with constant current to each phase sequentially and stepping the rotor for one complete mechanical revolution. By counting the number of rotor steps, the number of rotor poles is determined as, constant current excitation results in the rotor to stay in the aligned position. After the experiments, it was determined that the motor has 12 stator poles and 8 rotor poles. In Fig. 5.3, the experimental SRM model is shown.

Table 5.1: Experiment SRM parameters.

Parameter	Value
Configuration	12/8
Rated Speed	2200 rpm
Voltage	60/72 V
Current	120/100 A
Torque	23.7/21.7 Nm
Number of phases	3
Max efficiency	83 %
Shaft Diameter	30 mm
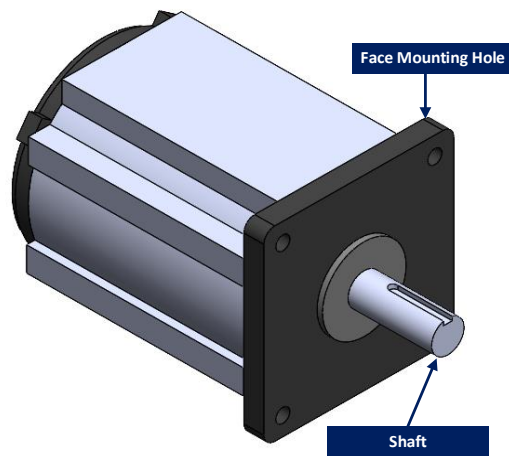
Fig. 5.3: The model of the experimental SRM with a 30 mm shaft.

The IM used in the setup is a standard NEMA frame motor. The specification provided by the manufacturer are listed in Table 5.2. The IM is manufactured by Brook Crompton under the BA2N015-3 designation. In Fig. 5.4, a model of a NEMA 254T motor is shown (not the exact motor used in the setup).

Table 5.2: Brook Crompton IM parameters.

Parameter	Value
Power	15 hp/11 kW
Number of pole pairs	2
Rated Speed	3540 rpm
Voltage	208/416 V
Current	37.7/18.9 A
Frequency	60 Hz
Number of phases	3
Max efficiency	91 %
Motor frame	NEMA 254T
Shaft diameter	1 5/8 inch
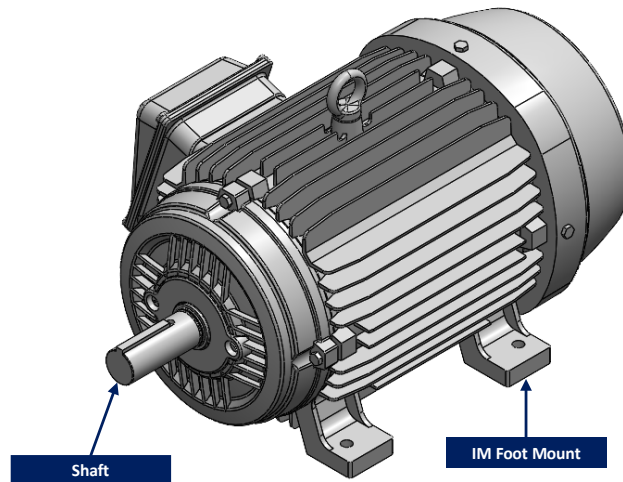
Fig. 5.4: CAD of NEMA 254T IM with 1.625-inch shaft.

Both the SRM and IM need to be mounted to the T-slot table with their shafts aligned at the same vertical height. In the case of the SRM, it has mounting holes in the axial direction on the shaft side. To mount the SRM to the T-slot table, a faceplate and angle bracket are used, as shown in Fig. 5.5. With this configuration, the shaft of the SRM is positioned at 171.45 mm from the base of the T-slot table.

Also, as the SRM used in this setup is considered as a low torque motor, only one angle bracket on one side of the faceplate is adequate. Otherwise, with higher torque motors, two angle brackets should be used on opposite ends of the faceplate. Additionally, all mounting hardware is made of A36/W44 steel as it is commonly available and has good mechanical properties (tensile strength and elongation) for general fabrication applications [31]. Also, the SRM mounting holes on the faceplate have a slightly larger thru hole tolerance to allow for some vertical and horizontal adjustment which is vital for the alignment process.
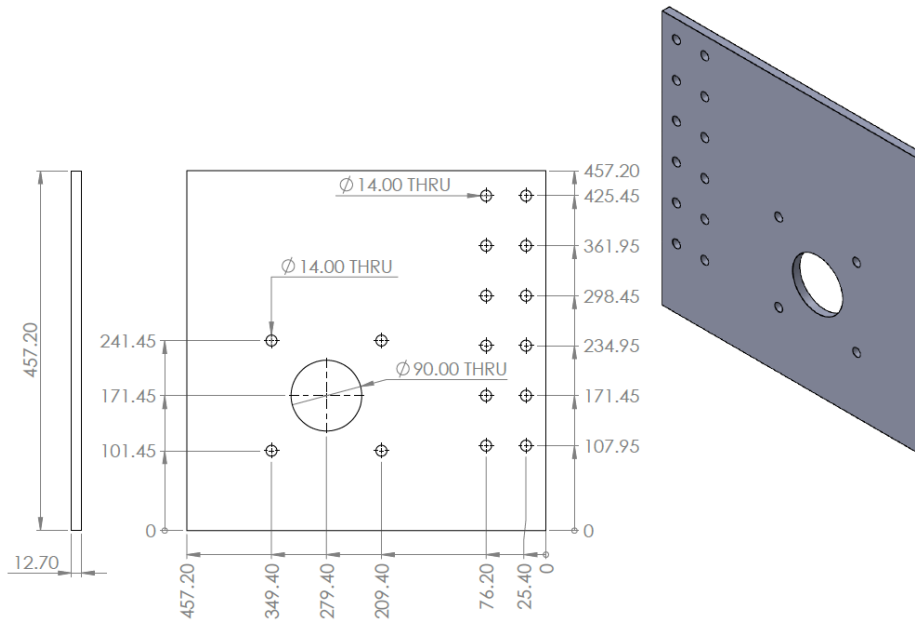
Fig. 5.5: Experiment SRM faceplate with vertical and horizontal shaft adjustment.

Similarly, the IM motor with the standard foot mount holes also need to be secured to the T-slot table. In this case, a modular mounting plate was designed to mount the IM to the T-slot table and raise the IMs shaft to the correct height. The material thickness of the IM mounting plate at 12.70 mm results in the shaft of the IM to be positioned 171.45 mm vertically from the T-slot table base. This allows

the SRM and IM shafts to be at the same vertical height relative to the T-slot table for alignment. The IM and mounting plate are shown Fig. 5.6. To mount the IM to the T-slot table, two mounting plates are needed as they are designed to be modular. With this split design, two smaller plates are needed reducing wasted material, weight, and allowing for easy shipping/handling. Two sets of additional thru hole mounting points were added to the IM plate to allow for different alignments: inline with the T-slot or between two T-slots. To aid in alignment, keyways are cut at the of bottom the IM mounting plates which are parallel with the T-slots.
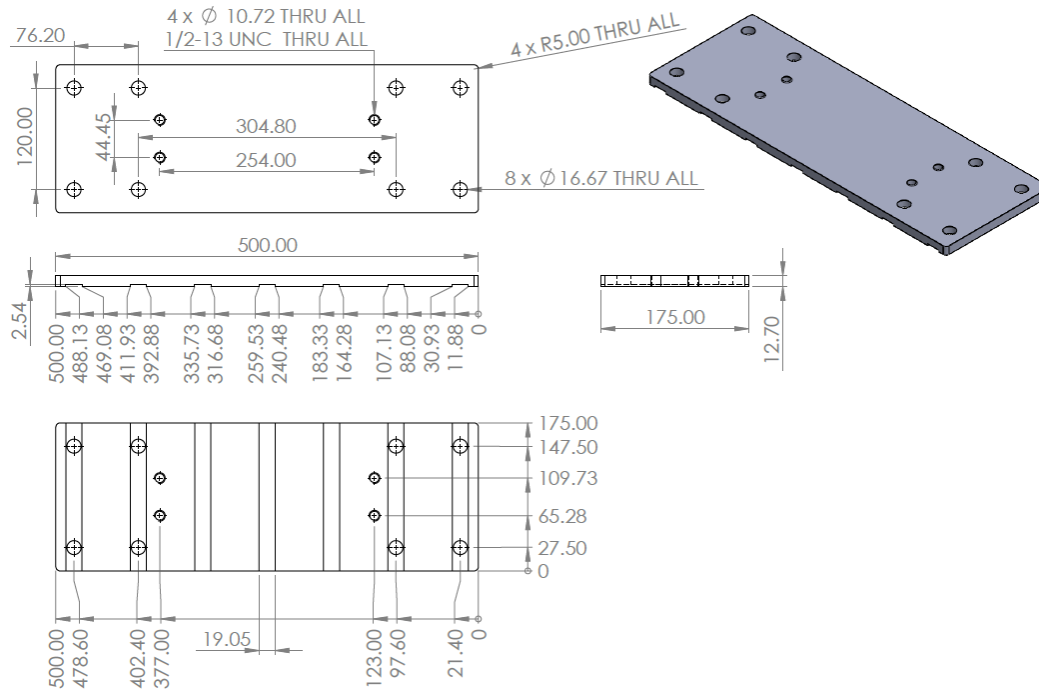
Fig. 5.6: NEMA 254T foot mount bracket with horizontal shaft adjustment.

5.1.2 – SRM Inverter and Control

The SRM is powered by an H-bridge converter for each phase. In Fig. 5.7, the topology of a single-phase H-bridge converter is shown. An H-bridge is similar to an asymmetric bridge converter, except the diagonal diodes are replaced with

switches. However, an H-bridge can be used like an asymmetric bridge converter if two of the diagonal switches are left open in each leg, as along as the switches used a free-wheeling diode. For example, by leaving S_2 and S_3 open the only conduction path is through the free-wheeling diodes of each switch.
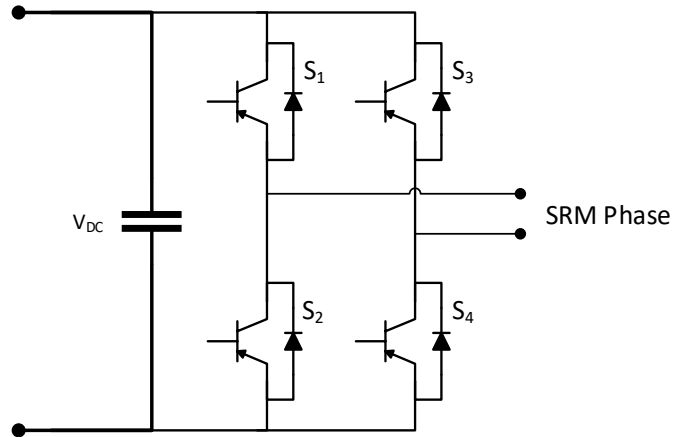
Fig. 5.7: Single phase H-bridge topology.

The SRM inverter is fed by a bidirectional DC power supply at 72 V and 120 A current limit. The SRM inverter contains DC-link capacitors internally, and each phase is connected across each H-bridge module. In Fig. 5.7, only one phase is shown but the remaining H-bridge modules are connected in parallel to the DC-link capacitors. The gating signals are provided by the dSpace MicroLabBox in the form of low voltage digital signals.

In Fig. 5.8, the CAD model of the SRM inverter is shown. For the setup, a 4-phase SRM inverter with four H-bridge power modules is used. The inverter has screw down terminals with cable glands for the SRM phases and DC-link voltage supply. Also, each power module can be interfaced from an external ribbon cable to provided power and gating signals independently. By interfacing with each

module independently, the phase isolation that the H-bridge topology is retained. This also allows for the SRM inverter to be configured for 3- or 4-phase control without any hardware modification. A pair of water and airtight quick-disconnects allow for a liquid cooling connection to be added to extract heat from the H-bridge modules and DC-link capacitors.
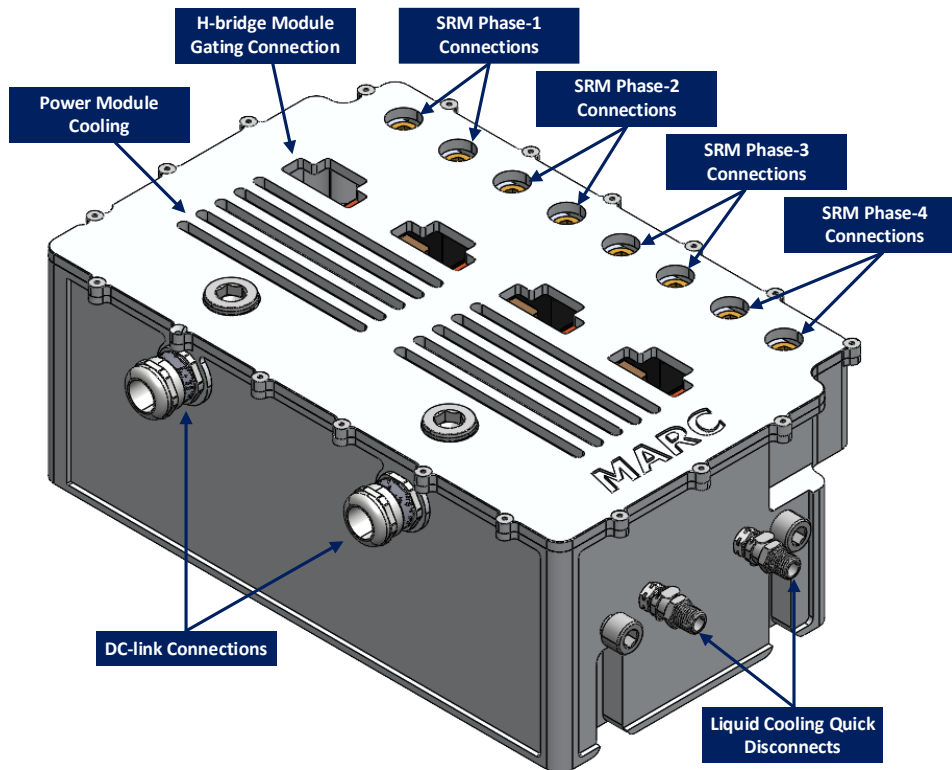
Fig. 5.8: 4-phase SRM inverter using H-bridge power modules.

In Fig. 5.9, the simple liquid cooling setup used for the SRM inverter is shown. The setup consists of a 22.7 L reservoir to carry the 50/50 water-glycol coolant. To pump the coolant throughout the inverter, a 1/40 hp 120 V_{AC} 60 Hz single phase submersible motor is used. The pump motor is cooled by the coolant it is submersed in and can operate for long periods of time with little to no maintenance. Silicon piping is used to carry the coolant to the inverter, but plastic

quick-disconnects are used to interface with the inverter. The plastic quick-disconnects only allow fluid to flow if connected, otherwise they close an internal check valve to restrict flow. This method of connection limits the potential for spills. Also, when designing the coolant loop, the number of metallic components was limited to reduce the chances of oxidization and rust accumulation.
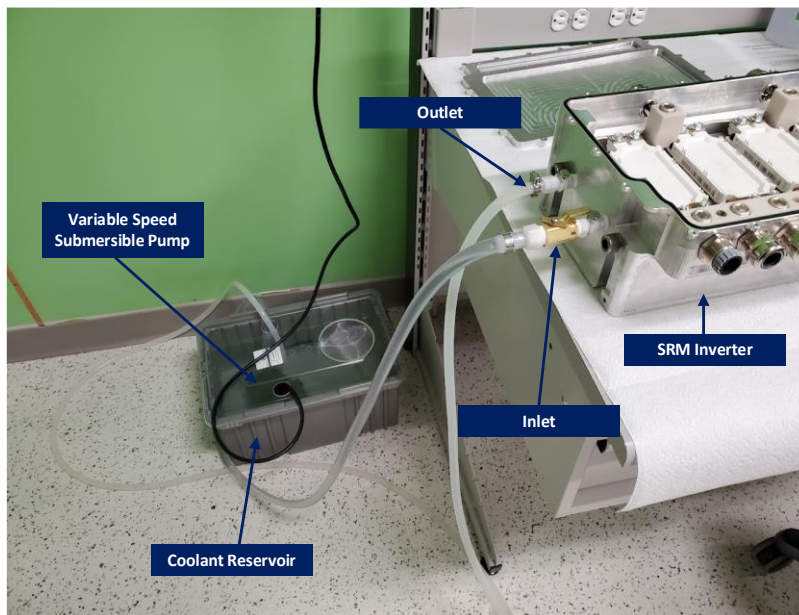
Fig. 5.9: SRM inverter liquid cooling setup.

In the current form of the liquid cooling system, heat is extracted and sent to the reservoir where it is dissipated. This method is suitable for low power setups. For higher power setups, an external heat exchanging radiator can be placed in the reservoir. This allows for improved heat extraction and provides coolant isolation from the external heat exchanging radiator.

The gating signals for the SRM inverter are provided by the dSpace MicroLabBox rapid prototyping controller. The MicroLabBox uses a Freescale P5020 dual-core processor with a 2 GHz clock. The CPU has active thermal

monitoring using a temperature sensor to protect the CPU from overheating. In Table 5.3, the CPU cache type and memory are shown. The MicroLabBox has up to 1 GB of available local RAM depending on the complexity of the real time model being deployed. The MicroLabBox has capability such as: timers, interrupts, host interfaces, USB interfaces, ethernet interface, analog-to-digital conversion, digital-to-analog conversion, bit IO, and FPGA support.

Table 5.3: dSpace MicroLabBox cache sizes.

Cache type	Cache size
L1	32 kB per core
L2	512 kB per core
L2 instruction	32 kB per core
L3	2 MB total

The control and sensor feedback processing for the SRM inverter is carried out by the dSpace MicroLabBox. Class-1 ADCs have 16-bit sampling resolution up to 1 μs and can accept a voltage range from -10 to 10 V. The Class-2 ADCs have 14-bit sampling resolution fixed at 1 ns and can accept a voltage range from -10 to 10 V. The Class-1 bit IO (GPIO) can be configured as input/output with three different voltage levels (2.5 V, 3.3 V, and 5.0 V), and software filters can be defined for each input. Class-2 bit IO (GPIO) are differential bidirectional digital signals.

The dSpace MicroLabBox is configured to read the SRM phase current sensor and torque transducer feedback using the Class 1 ADCs. The Class 1 bit IO (GPIO) are configured to provide 5 V gating signals to the SRM H-bridge modules. The MicroLabBox is configured with a sampling rate of 50 μs, or a sampling frequency of 20 kHz.

5.1.3 – Load Induction Machine and Control

The IM used in the setup is supplied and controlled by a wall mount drive capable of four-quadrant operation. The ABB ACS800-11/U11 drive consists of two back-to-back converters as depicted in Fig. 5.10. The line-side converter is responsible for taking the 3-phase AC supply and converting it to DC voltage using an IGBT-based 3-phase rectifier. Then, the DC voltage is converted back to AC using another IGBT-based 3-phase inverter. The whole drive topology is essentially an AC/AC converter which takes the 208 V phase-to-phase voltage at 60 Hz and supplies the IM with AC voltage which is amplitude adjusted and has a variable frequency.
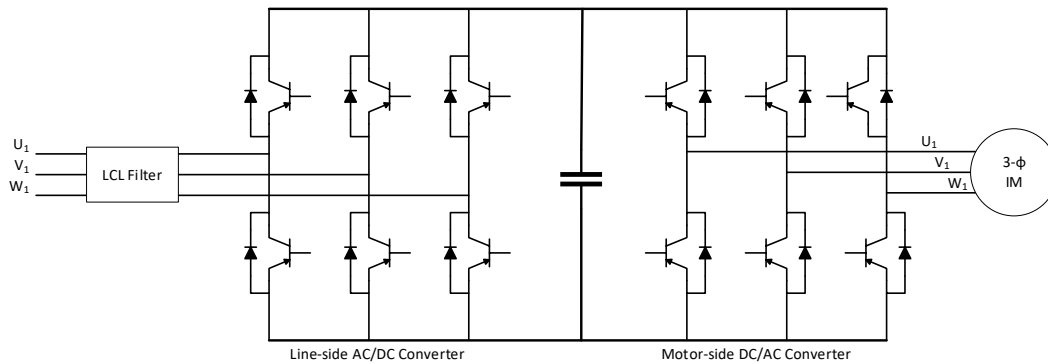
Fig. 5.10: Back-to-back converter topology used for the IM drive.

The IM drive is installed on a load bearing wall near the IM and T-slot table professionally as shown in Fig. 5.11. The IM drive is fed by 208 V 3-phase 60 Hz through a distribution board containing a lockout switch and fuses for each phase. The IM drive can be controlled using the external control panel and can also be used through an external drive communication interface via a host PC. The IM drive also processes the IMs incremental encoder data to determine speed and direction of rotation.
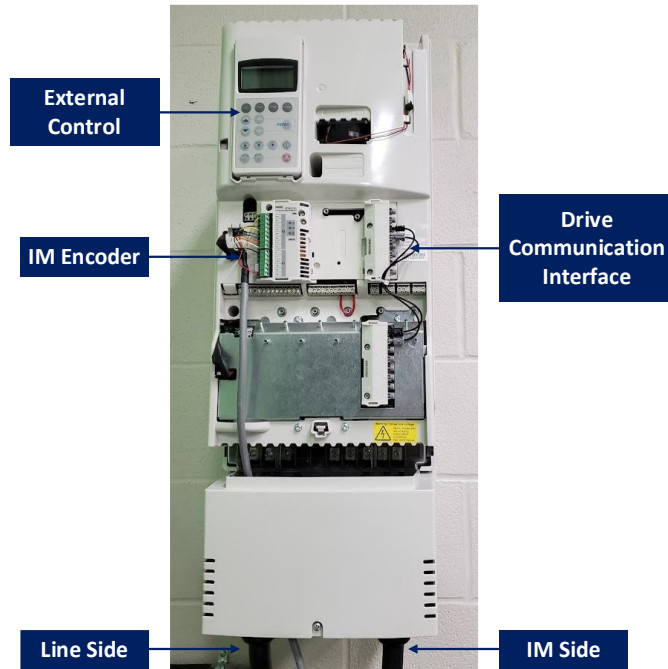
Fig. 5.11: ABB ACS800-11/U11 four-quadrant IM drive with front cover removed.

5.1.4 – Torque Transducer

The torque transducer is placed between the SRM and IM to measure the torque between the two machines. The torque transducer used for this setup is from NCTE, and the model used is Series 3000 with a round shaft. In Table 3.1, some key torque transducer characteristics are shown.

Table 5.4: NCTE torque transducer parameters.

Parameter	Value
Nominal torque (bidirectional)	250 Nm
Speed	8000 rpm
Accuracy	$\leq 0.02\%$
Axial force	7000 N
Limit transverse force	800 N
Limit bending moment	176 Nm
Analog output	-10 to 10 V
Shaft diameter	25 mm

The torque transducer used in the setup provides an analog voltage output ranging from -10 to 10 V. With any analog voltage output signal, significant noise is present which requires filtering via hardware and software. The torque transducer is capable of measuring torque from 0 to 250 Nm with an accuracy of less than 0.02 % in both the CW and CCW direction. To filter the output of the torque transducer, a 330 µF 25 V rated capacitor can be place across the torque transducer supply to suppress the high frequency noise.

In Fig. 5.12, the model and data accusation connections are shown for the torque transducer. The offset and gain values are provided from the manufacturer as a part of the calibration process. A discrete FIR filter block was implemented which uses 500 sampled torque points in the Simulink model, to improve the low torque measurements which are heavily affected by noise. The ADC gain parameter needs to be added to correctly read the ADC voltage and is specified in MircoLabBox documentation. Additionally, a torque offset is added prior to the scope to further improve the torque measurement. This is done by reading the scope data with no load and subtracting the average no-load torque observed as an offset. In Fig. 5.13, the torque transducer CAD model is shown.
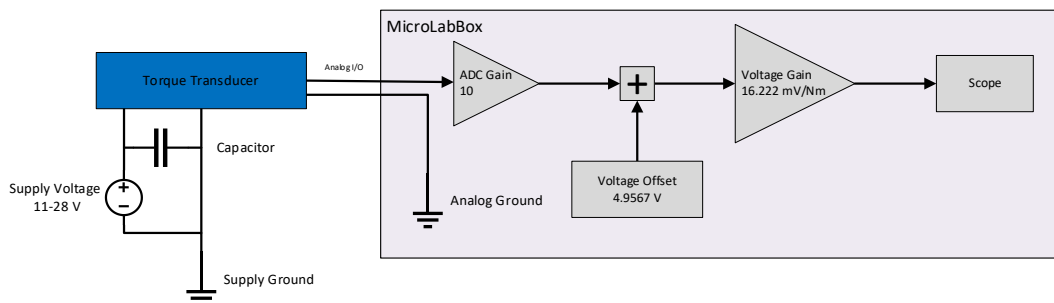
Fig. 5.12: Torque transducer connection diagram and voltage to torque conversion process.
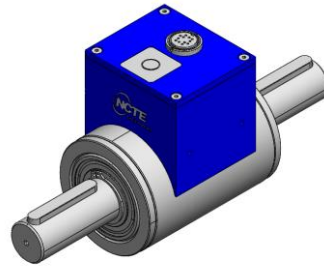
Fig. 5.13: Torque transducer form NCTE with 25 mm shaft.

Similar to the IM and SRM, the torque transducer also needs to be firmly mounted to the T-slot table. In Fig. 5.14, the torque transducer bracket is shown. The bracket is modular in terms of shaft alignment and setup configuration. The torque transducer consists of a bottom bracket which allows for the torque transducer to be mounted in line with a T-slot or between the T-slots. The bottom bracket also allows for horizontal shaft offset alignment. The side brackets mount to the bottom bracket and holds up the torque transducer to required shaft height. In this setup, a vertical shaft height of 171.45 mm is required. As the side brackets are modular, they can be replaced to achieve a different shaft height for a different setup. The side bracket mounting hole design results in ±3 mm of vertical height adjustment in the torque transducer to allow for vertical shaft alignment.
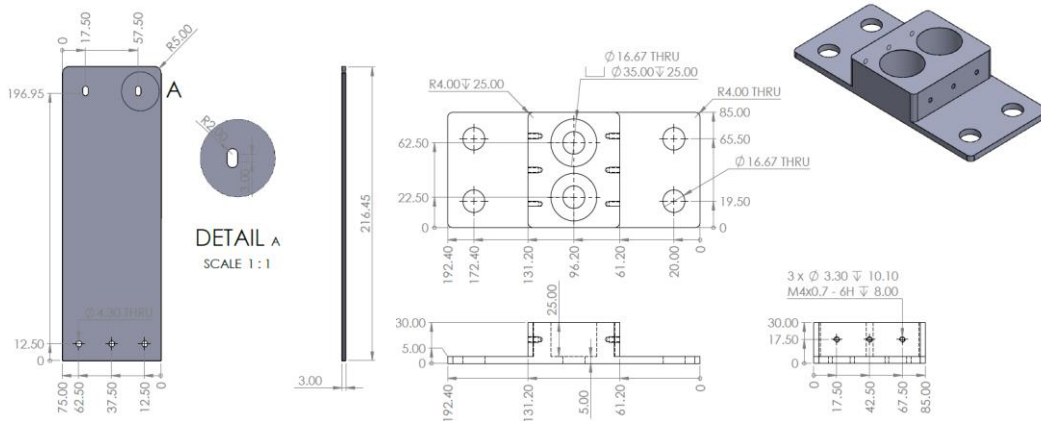
Fig. 5.14: CAD of torque transducer bracket.

5.1.5 – SRM Encoder

Measuring the SRM rotor position is vital for control, as the rotor position is used to determine the electrical rotor position. For this reason, an absolute encoder is used for the SRM and is placed at the rear shaft extension of the SRM, as shown in Fig. 5.15. The encoder used in the setup is a Sensata HS35 with gray code output with a through shaft configuration and has a frequency response of 500 kHz or rated speed of 6000 rpm. The gray output code consists of 12-bits, allowing for 4096 steps in a complete mechanical rotation, and 91 steps for an electrical cycle for an SRM with 8 rotor poles.

Once the absolute encoder is secured to the shaft extension, a reference phase is excited with continuous current, and the mechanical position is read from the encoder. An offset is added to the mechanical position calculation such that it results in a zero-degree mechanical position. By doing so, the associated electrical position is zero degree electrical for the aligned reference case and correctly calculates electrical angle for the remainder phases. If the encoder is securely mounted to the shaft, the offset does not need to be changed once set.
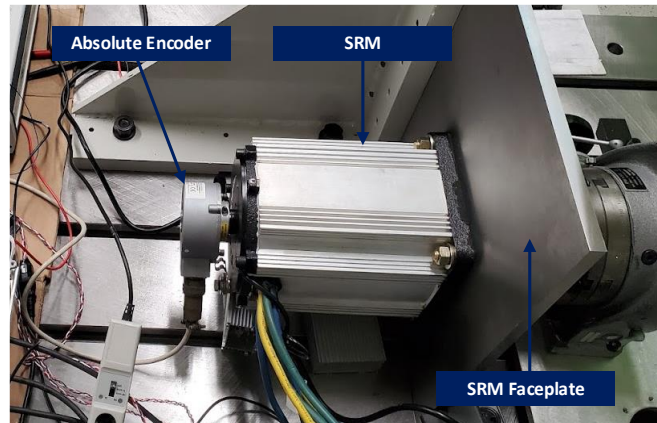
Fig. 5.15: Absolute encoder placement on the SRM.

In Fig. 5.16, the diagram for measuring the electrical angle of each phase of the SRM from the output of the absolute encoder is shown. The encoder provides 12-bit gray code which needs to be converted to binary. Once converted to binary, all the bits are added up to determine the step number using the most significant binary bit to the least significant binary bit. The direction of rotation can be changed by applying a '1' for CW and '0' for CCW, which effects the position steps signal to rise or decrease with rotation.

If the number of rotor poles is known and the SRM has perfect manufacturing tolerances, the mechanical position can be converted into to electrical position. However, for the physical SRM geometry all stator and rotor pole arc tip angle will not be the same due to manufacturing tolerances. With the encoder is firmly installed, each phase is provided with constant excitation to determine the aligned mechanical position. From the aligned mechanical position, the exact electrical position for each phase can be determined for the SRM geometry. However, the electrical positions determined with this method will only be valid if the encoder is not removed, due to the encoder offset changing.
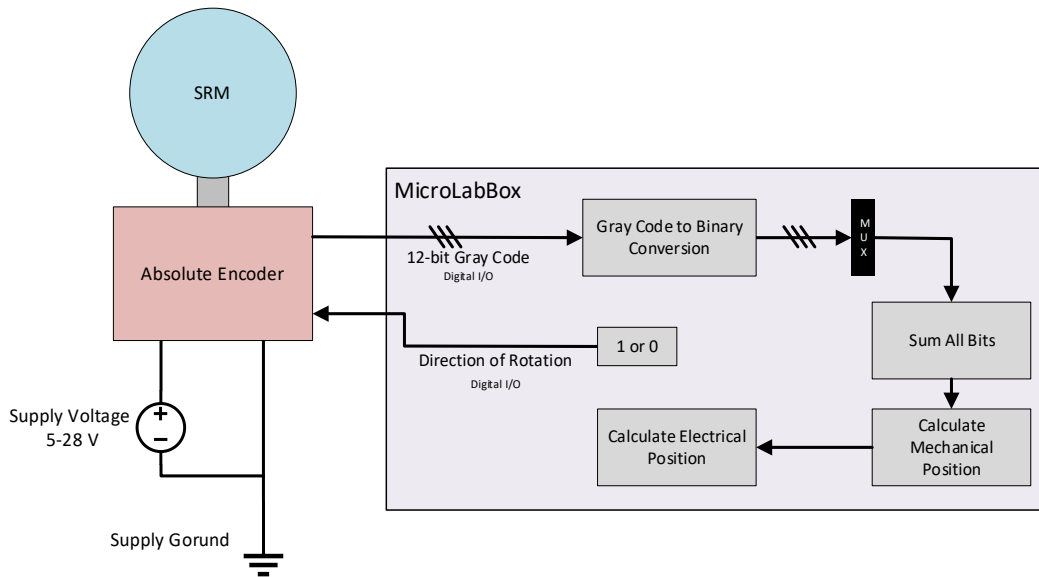
Fig. 5.16: Absolute encoder connection diagram and gray code to rotor position conversion process.

5.1.6 – Alignment and Completed Setup

Once all the components were sourced for the experimental setup: the IM, SRM, and torque transducer were aligned. Alignment began by selecting a fixed point; in this case it was the IM mounted to the T-slot table using mounting plates. The IM has the least amount of adjustability from all the other components as it lacks vertical adjustability, resulting in it being considered the fixed point. It was then placed and aligned on the T-slot table with the shaft being parallel to the length of the table. Then the torque transducer was placed on the T-slot table to be roughly aligned with the IM machine shaft, using the vertical and horizontal adjustment available from the torque transducer mount. The IM and torque transducer shafts were coupled using Atra-Flex M1 flexible couplings, as shown in Fig. 5.17.
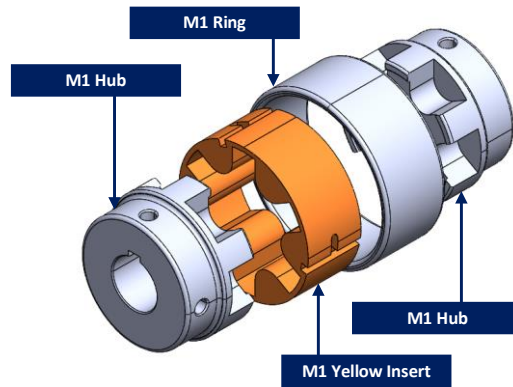
Fig. 5.17: Atra-Flex M1 flexible couplings.

Once the IM and torque transducer were coupled visually, more precise alignment was carried out by a laser shaft alignment tool, TSKA 31. In Fig. 5.18, the laser shaft alignment tool is shown with the stationary measuring unit placed on the IM shaft and movable measuring unit placed on the torque transducer shaft.
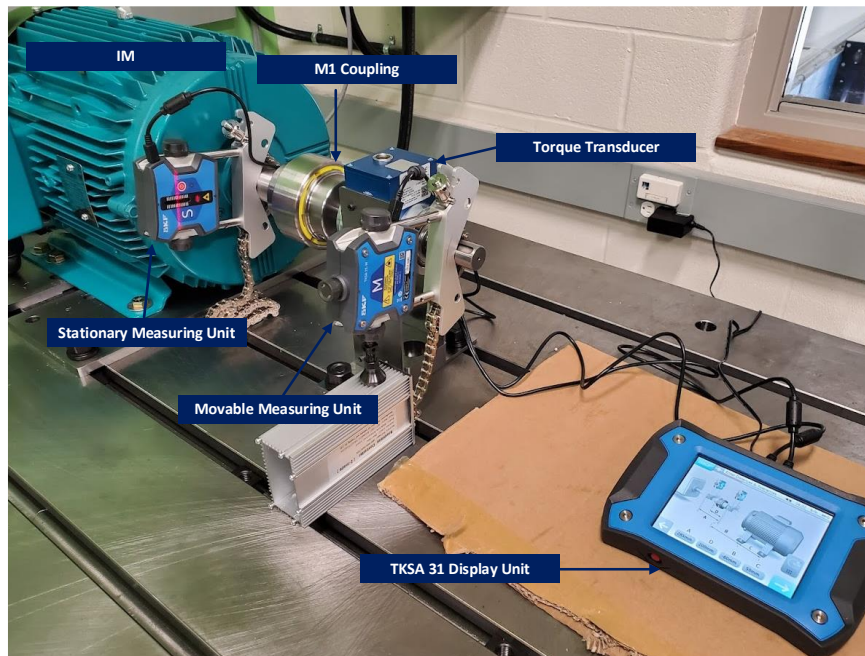
Fig. 5.18: TKSA 31 laser shaft alignment tool placement for IM and torque transducer alignment.

Then laser shaft alignment tool was used to align the shaft of the IM relative to the torque transducer in two key axis (horizontal and vertical) and for two parameters (offset and angular misalignment). For this setup, the alignment tolerance selected are for 3000-4000 rpm range (angular misalignment 0.06 mm/100mm and offset 0.04 mm). Once completed, an alignment report is generated for the IM and torque transducer as shown in Fig. 5.19(a). The report shows the initial alignment and end results. However, by using the M1 flexible coupling, the offset can be 0.1 mm and the angular offset can be 2 degrees (3.49 mm/100 mm), but results in the M1 yellow insert to deteriorate faster, shown in Fig. 5.17.

In the next step, the torque transducer and SRM were aligned using the laser shaft alignment tool, in which the fixed component is the torque transducer, and the movable component is the SRM. In Fig. 5.19(b), the alignment report is generated for the torque transducer and SRM. In this case the horizontal alignment is within specification, but the vertical alignment is marginally out of 3000-4000 rpm specification. However, due to the flexible coupling used in the setup, these tolerances are acceptable especially with the maximum speed being limited to 3540 rpm, which is rated speed of the IM.
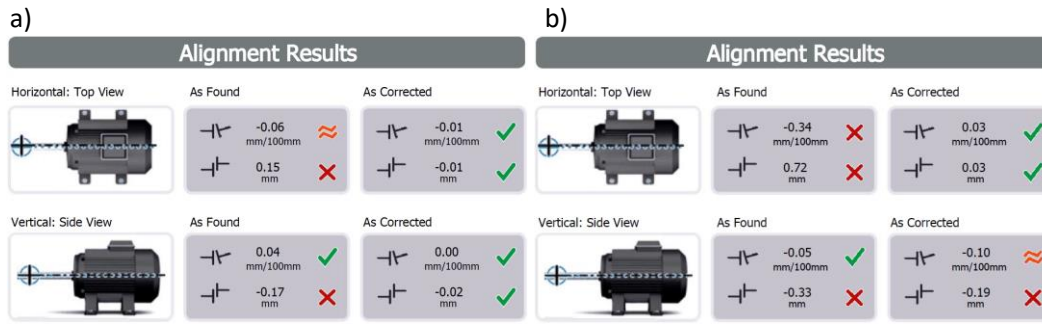
Fig. 5.19: Laser shaft alignment results for a) IM and torque transducer b) torque transducer and SRM.

In Table 5.5, the M1 flexible coupling bore, and key dimensions are shown for the IM, SRM, and torque transducer.

Table 5.5: Shaft diameter and key dimensions used for M1 flexible couplings.

Shaft	Diameter	Key height	Key width
IM	1.625 in	0.167 in	0.375 in
SRM	30 mm	3.3 mm	8 mm
Torque transducer	25 mm	3.3 mm	8 mm

In Fig. 5.20, the completed experimental SRM setup is shown. Shaft guards are placed over the flexible shaft couplings, torque transducer, and SRM absolute encoder. In addition, an emergency stop button is wired to regenerative power supply to switch off the voltage being supplied to the SRM inverter. An interface board was designed to convert various connector types, organize IO, and supply power to the sensors and gate drive boards. The interface board is placed on a 3D printed base which stores all the AC/DC converters and routes all sensor cables. In addition to the host PC, an oscilloscope is used to monitor the phase current and rotor position of the SRM.
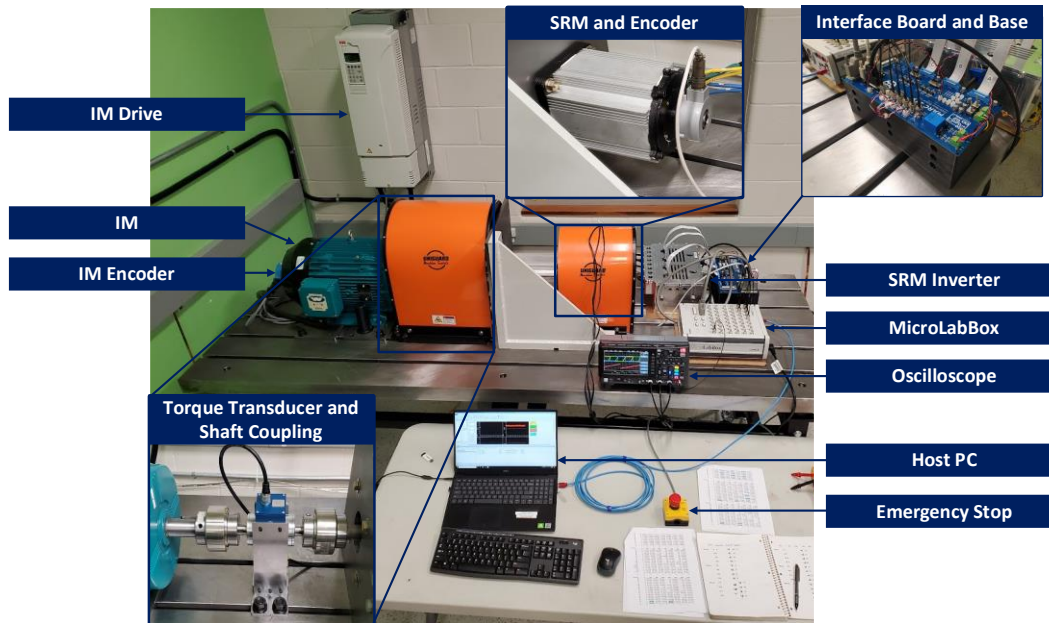
Fig. 5.20: Complete experimental SRM setup.

5.2 – Experimental Validation

In this chapter, the experiment SRM static characterization is completed through position indexing, the generating mode setup is developed for experimental validation, and the experimental results are shown.

5.2.1 – SRM Static Characterization

The internal rotor and stator geometry of the SRM that is used in experimental validation is not available. With this limitation, the motor geometry cannot be implemented in FEA to obtain the static characteristics which is used for the dynamic modeling of the motor. However, the static characteristics of the motor can be determined through position indexing.

Physical motor indexing is done by locking the rotor of the SRM and applying voltage pulses at different rotor position to determine the flux linkage characteristics. As flux linkage cannot be physically measured, the phase voltage

and current will be measured instead. The flux linkage can be determined from the phase voltage and current using the expression:

$$\lambda(\theta, i) = \int_0^t [V(t) - Ri(t)] \, dt \qquad (5.1)$$

where the flux linkage λ can be calculated for a fixed rotor position θ and current reference i by solving the time integral containing phase voltage V and phase resistance R.

To perform indexing, the SRM rotor was locked mechanically at a specific rotor position using a vertical rotary table. A single phase of the SRM was connected to the SRM inverter to apply the voltage pulse, and the control is provided by the MicroLabBox. An oscilloscope was used with differential probes and current sensors to measure the phase voltage and phase current, respectively. The oscilloscope is also used to capture and save data for post-processing. An encoder was used to determine the rotor position accurately and ensure that the rotor position was maintained during the experiments. In Fig. 5.21, the indexing setup is shown for the experimental SRM.

The SRM indexing experiment was carried out using the voltage pulse method [32]. The phase winding resistance was measured using a micro-ohmmeter multiple times to determine the average phase resistance. The micro-ohmmeter was zeroed after every measurement by connecting the measurement leads together. The micro-ohmmeter is shown in Fig. 5.22, and the average phase resistance measured was 23.175 mΩ.
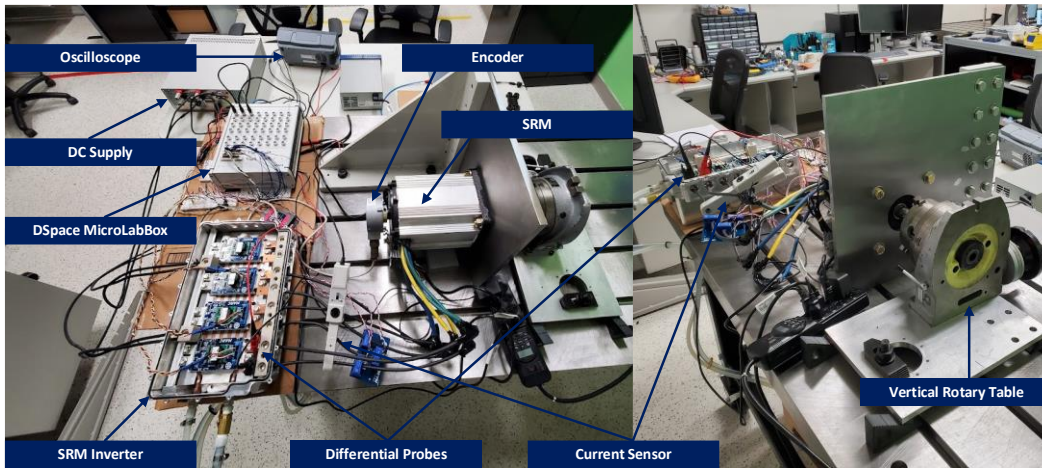
Fig. 5.21: Experimental SRM with locked rotor for indexing.
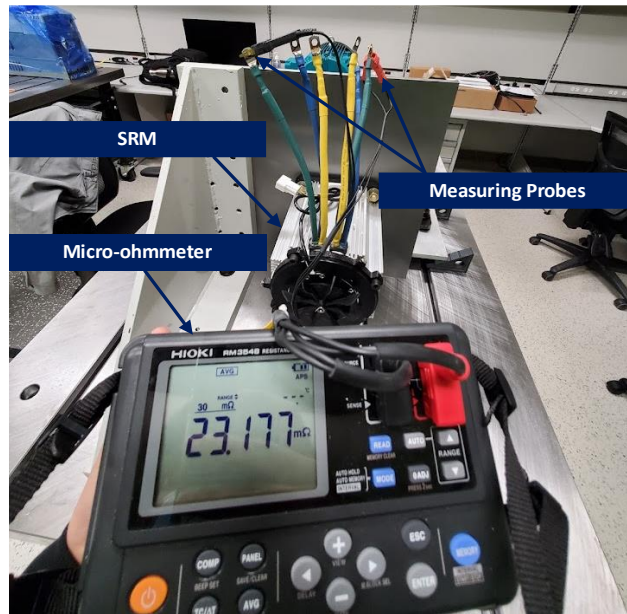
Fig. 5.22: Micro-ohmmeter used to measure the SRM phase winding.

After the phase resistance measurement, the SRM rotor was locked in the aligned position (180 degree electrical) using the rotary table. Using the MircoLabBox, a Simulink model was created to generate a voltage pulse until the SRM phase current increased to a desired reference. For a given rotor position, the voltage pulse was applied to achieve 5 A to 95 A phase current with 5 A increments,

and an oscilloscope was used to capture and save data. This process was carried out

from the aligned position to the unaligned position (180 to 0 degree electrical). With

this method, only one short duration voltage pulse was applied for each

measurement and the time in between allowed the phase to dissipate heat, resulting

in thermal deviation in the phase winding being negligible. The remaining data

from past alignment was acquired by mirroring the data obtained prior to alignment.

In Fig. 5.23, a sample voltage and current pulse are shown for the 90 degrees

electrical rotor position captured from the oscilloscope.
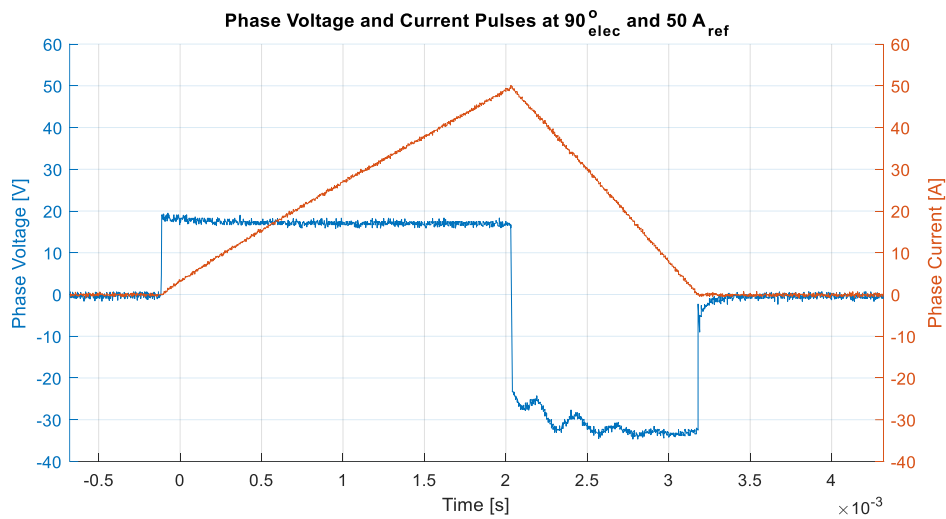
Fig. 5.23: The phase voltage and current pulses at 90 degrees electrical and 50 A current reference for the 12/8 3-phase SRM.

Once the data was captured, the flux linkage is calculated from the phase

voltage using (5.1). In Fig. 5.24, the flux linkage measurement results are shown.

a)   b)
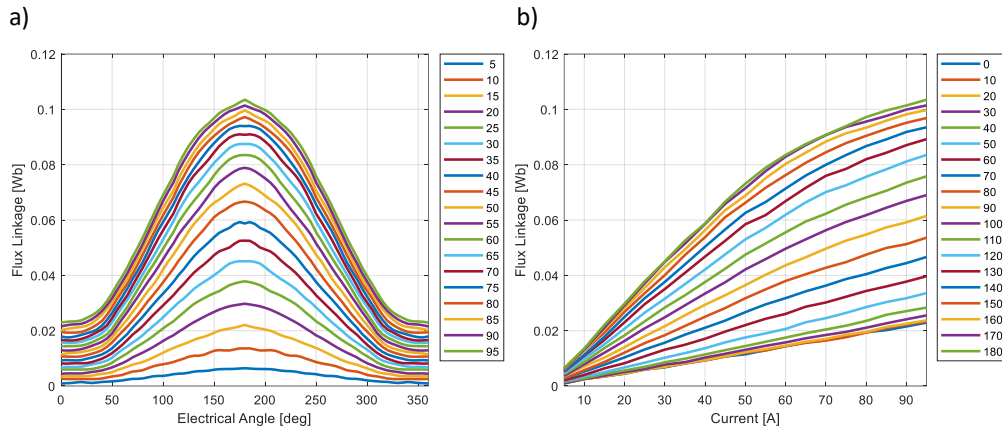
Fig. 5.24: Experiment SRM flux-linkage characteristic for (a) electrical rotor position, (b) phase current.

During the SRM indexing experiment, the torque transducer was not coupled between the SRM shaft and vertical rotary table. The flexible couplings introduce gear lash which results in the rotor position to change, and the torque transducer might not be very accurate in static reaction [33]. The static torque can be calculated using the flux linkage characteristics. In (5.2), the co-energy is calculated from flux linkage. Then using (2.14), the electromagnetic torque is calculated from co-energy.

$$W_c = \int \lambda di \qquad\qquad (5.2)$$

In Fig. 5.25, the static electromagnetic torque is calculated from flux linkage for the 12/8 SRM. A quick validation of the static torque characterisation was conducted by measuring the torque using the torque transducer and comparing it to the torque calculated from the flux-linkage. The setup is shown in Fig. 5.26. As discussed earlier, a small deviation in torque measurement is expected due to the rotor position changing and the torque transducer not being designed for static reaction but can still be a good indication of successful characterisation. In

Table 5.6, the percent error is shown between the measured and calculated torque for the 90 degrees electrical rotor position. In general, the absolute error is below 10 % for all the cases compared.
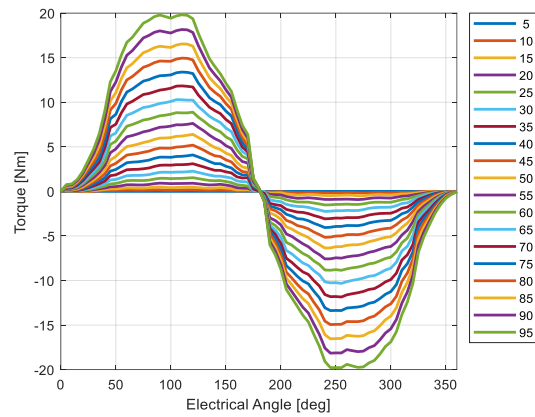
Fig. 5.25: Experiment SRM electromagnetic torque characteristic for electrical rotor position.
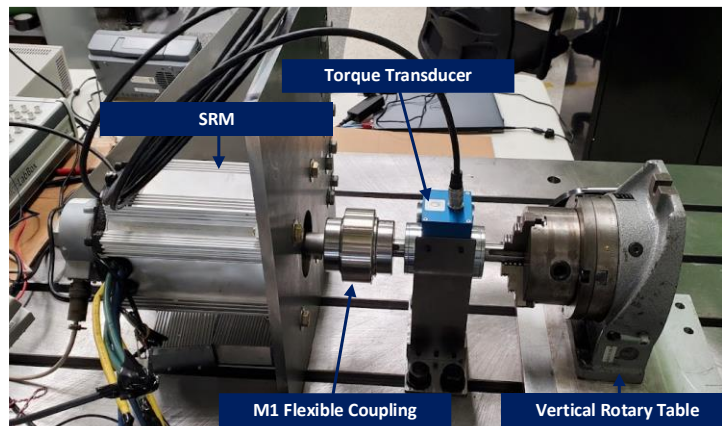
Fig. 5.26: SRM shaft fixed by a vertical rotary table through the torque transducer.

Table 5.6: Calculated torque and measured torque comparison for 90 degrees electrical with a locker rotor.

Current [A]	Calculated torque [Nm]	Measured torque [Nm]	Absolute error [%]
20	0.923	1.000	8.292
30	2.138	2.300	7.553
40	3.840	4.100	6.762

50	5.980	6.500	8.702
60	8.480	9.250	9.074
70	11.364	12.300	8.240
80	14.626	15.800	8.030
90	18.010	19.300	7.162

5.2.2 – Experimental Control Setup and Simulation Correlation

The experimental validation is completed using the setup shown in Fig. 5.20, with the bidirectional power supply supplying 20 V to the SRM inverter. The experimental validation for generating mode is done using soft-switching. The MicroLabBox uses the position and current sensor feedback to control the SRM's phase current using the generating specific current control conditions in (3.5). As the motoring current control conditions in (3.2) results in the phase current to rise uncontrollably, shown in Fig. 5.27.
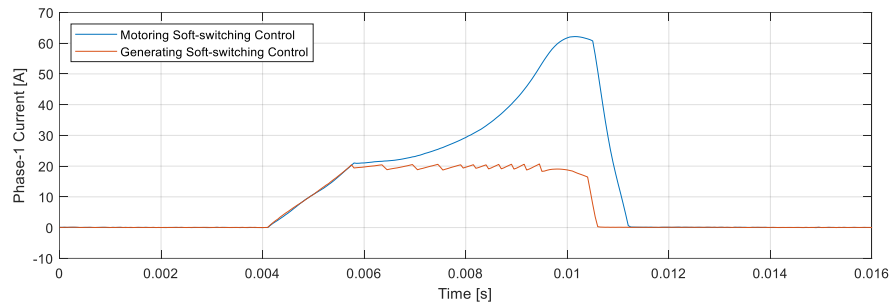
Fig. 5.27: Generating mode phase current using 20 V DC-link at 600 rpm and 20 A current reference using the motoring soft-switching control and generating specific soft-switching control.

The transient behavior of the experimental and simulation data needs to be compared. This is due to the conduction angles being generated using the Simulink based optimizer which uses the static characteristics determined in Section 5.2.1 and the static characterization could result in a deviation in dynamic performance.

In Fig. 5.28, the simulation and experimental results are compared for 600 rpm and

40 A current reference, for the turn-on and off conduction angles of 143.47 and

323.46 degrees electrical, respectively. In Fig. 5.28(a), the experimental and

simulation phase currents match closely, with the difference occurring at initial

excitation, due to voltage-current regulation of the power supply providing slightly

less than 20 V. In Fig. 5.28(b), the source current behavior matches closely. The

difference can be attributed to the bidirectional power supply filtering the source

current with a single pole low-pass filter (cut-off frequency of 2.1 kHz). In Fig.

5.28(c), the simulation torque does not show the ripples observed as the limited

bandwidth of the torque transducer filters the torque ripple. But the average torques

match closely.
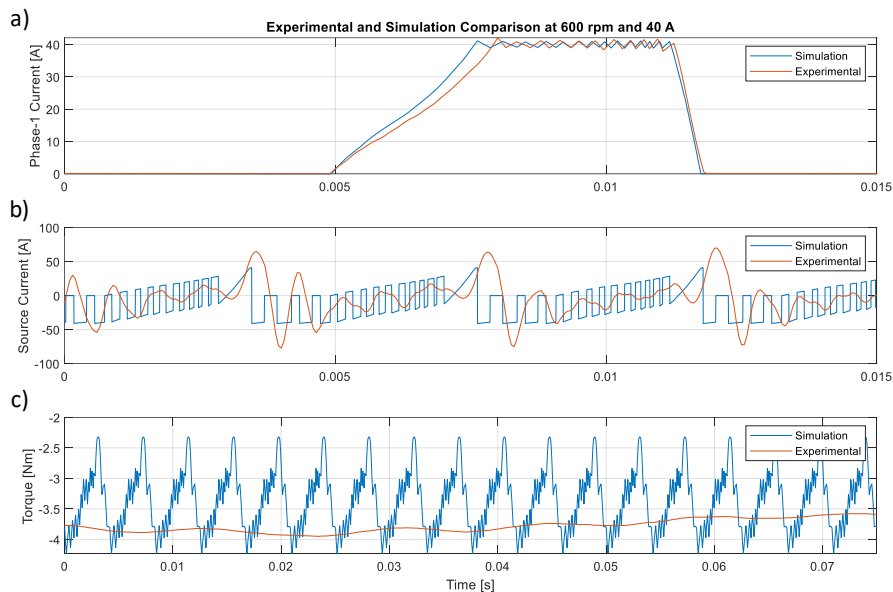
Fig. 5.28: Experimental and simulation results at 20 V DC-link, 600 rpm and 40 A current reference (a) phase-1 current, (b) source current, (c) shaft torque.

In Table 5.7, the phase current RMS and average torque have less than 10%

difference when comparing the simulation data to the experimental data for the

same operating conditions. The average source current has a considerable

difference in magnitude, because the internal filtering of the bi-directional power

supply results in the much smaller source current being supplied back to the source.

This comparison is done for various speeds and current reference points, and results

in similar percent differences for all three objectives. The consistency observed

shows that the constructed experimental setup has good correlation to the

simulations results.

Table 5.7: Experimental and simulation comparison using 20 V DC-link at 600
rpm and 40 A current reference.

600 rpm at 40 A$_{ref}$	Experimental value	Simulated value	Percent difference
Phase current RMS	15.549 A	15.014 A	3.5 %
Avg. source current	-2.78 A	-8.667 A	-102.9 %
Avg. torque	-3.643 Nm	-3.360 Nm	-8.08 %

5.2.2.1 – Experimental Validation of Optimization Objectives with 20 V

Supply Voltage and 600 rpm

In Fig. 5.29, the simulation results for the optimization objectives in Opt 1

of $\max|T_{avg}|$ and $\min(\Delta T_{RMS})$ are compared to the proposed generating specific

optimization objectives in Opt 2 of $\max|I_{source,avg}/T_{avg}|$ and $\min(\Delta T_{RMS})$. In Fig.

5.29(a), the conduction period for Opt 2 is smaller than Opt 1. Specifically, the turn-

off occurs earlier in the new optimization objectives (Opt 2). In Fig. 5.29(b), both

optimizations have source current oscillations with the same frequency as the

experiment is done at the same rotor speed. However, the proposed optimization

Opt 2 has much larger peaks for both the positive and negative magnitudes. In Fig. 5.29(c), the proposed generating specific objectives in Opt 2 extract much lower prime mover torque for a similar amount of source current when compared to the objectives in Opt 1.
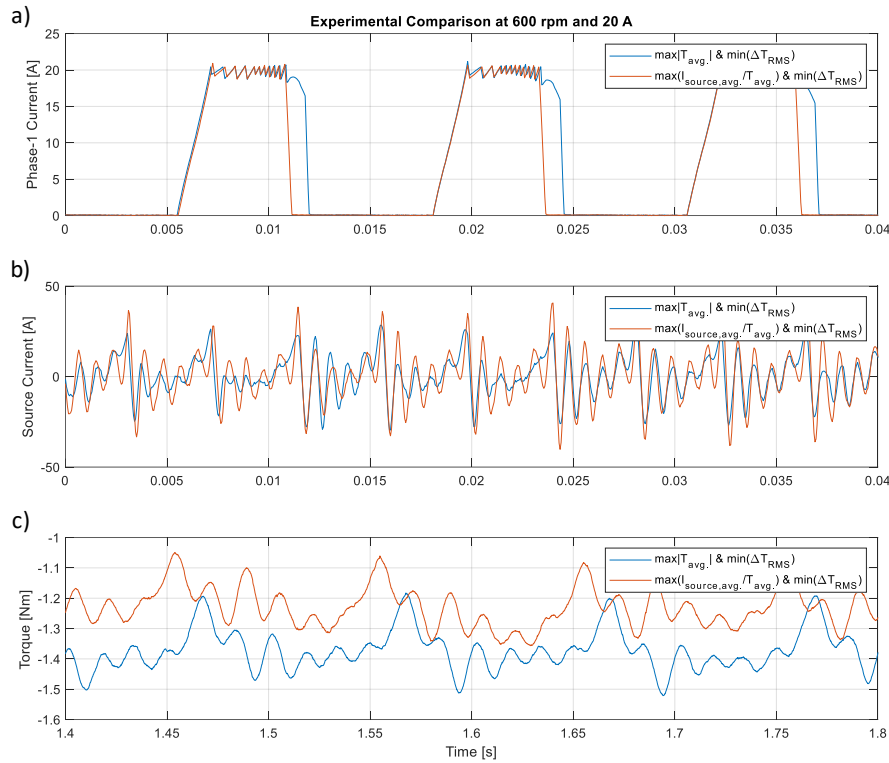
Fig. 5.29: Experimental results using 20 V DC-link at 600 rpm and 20 A current reference for (a) phase-1 current (b) source current (c) shaft torque.

In Table 5.8, the old Opt 1 and proposed optimization Opt 2 objectives are compared using the experimental results at 600 rpm and 20 A current reference. Using the proposed objectives (Opt 2), the phase current is reduced by 14.7 % which results in less copper loss. At 600 rpm and 20 A current reference, both cases draw power from the bidirectional power supply; however, the proposed objectives

in Opt 2 draw 54.2 % less current compared to the older objectives in Opt 1. The

proposed objectives (Opt 2) draw 10.4 % less prime mover torque. When

comparing the average source current per average torque for the two different

objectives, the proposed optimization shows a 48.6 % improvement.

Table 5.8: Comparison of old, Opt 1 and new, Opt 2 optimization objectives using 20 V DC-link at 600 rpm and 20 A current reference.

600 rpm at 20 A$_{ref}$	**Opt 1** $\max\lvert T_{avg}\rvert$ & $\min(\Delta T_{RMS})$	**Opt 2** $\max\lvert I_{source,avg}/T_{avg}\rvert$ & $\min(\Delta T_{RMS})$	**Percent change**
Phase current RMS	8.62 A	7.35 A	14.7 %
Avg. source current	0.48 A	0.22 A	54.2 %
Avg. torque	-1.35 Nm	-1.21 Nm	10.4 %
Avg. source current per avg. torque	-0.35 A/Nm	-0.18 A/Nm	48.6 %

At 600 rpm and 20 A current reference the average source current was

drawn from the bidirectional power supply. To improve the amount of source

current returned, the current reference is increased to 30 A for the same speed,

shown in Fig. 5.30. The proposed optimization objectives (Opt 2) have a slightly

earlier condition interval, which results in a phase current to rise and demagnetize

earlier compared to the older objectives in Opt 1, as shown in Fig. 5.30(a). The

source current of the proposed optimization objectives in Opt 2 have smaller peak

magnitudes compared to the older objectives in Opt 1. In the source current for Opt

2, there are fewer instances where the current is positive as shown in Fig. 5.30(b),

indicating less power is drawn from the bidirectional power supply. The proposed

optimization objectives in Opt 2 draw slightly more torque when compared to the

older objectives, as shown in Fig. 5.30(c).

The experimental results from Opt 1 and Opt 2 are compared in Table 5.10 for 600 rpm and 30 A current reference. The proposed optimization objectives in Opt 2 show a 2.02 % decrease in RMS phase current as the conduction interval is 0.07 electrical degrees smaller. With the advanced conduction angles, the proposed optimization (Opt 2) supplies 8.69 % more source current back to the bidirectional power supply. The proposed optimization objectives draw 2.42 % more generating torque when compared to the results from Opt 1. Lastly, the proposed optimization objectives in Opt 2 show a 5.41 % improvement in the amount of average source current per average torque when compared to the older objectives in Opt 1.
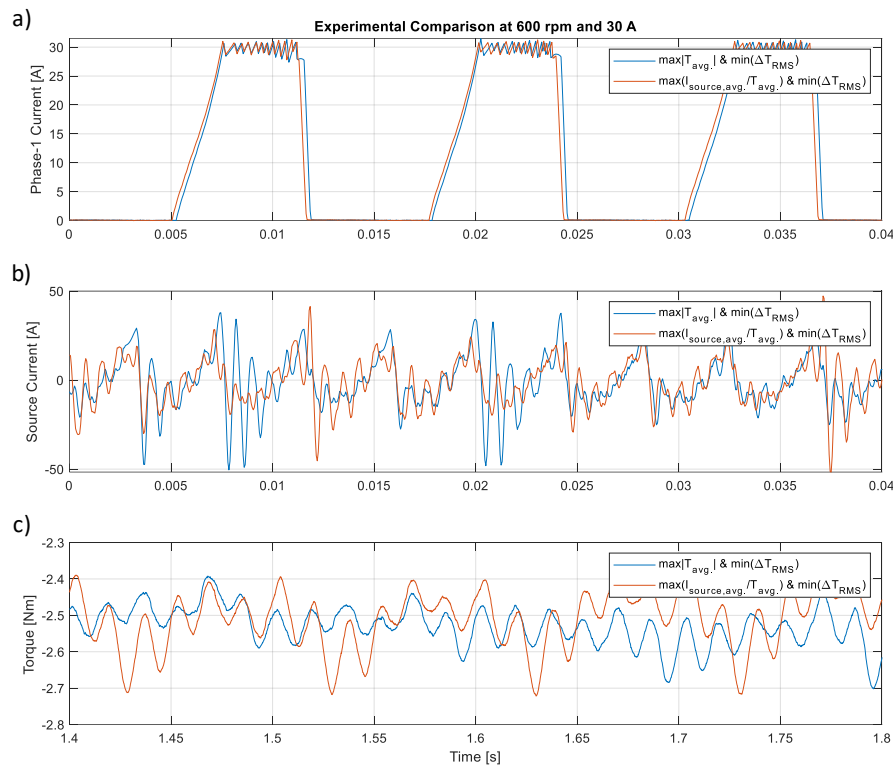
Fig. 5.30: Experimental results using 20 V DC-link at 600 rpm and 30 A current reference for (a) phase-1 current (b) source current (c) shaft torque.

Table 5.9: Comparison of old, Opt 1 and new, Opt 2 optimization objectives using 20 V DC-link at 600 rpm and 30 A current reference.

600 rpm at 30 A_{ref}	Opt 1 max$\|T_{avg}\|$ & min(ΔT_{RMS})	Opt 2 max$\|I_{source,avg}/T_{avg}\|$ & min(ΔT_{RMS})	Percent change
Phase current RMS	12.36 A	12.11 A	2.02 %
Avg. source current	-0.92 A	-1.00 A	8.69 %
Avg. torque	-2.48 Nm	-2.54 Nm	2.42 %
Avg. source current per avg. torque	0.37 A/Nm	0.39 A/Nm	5.41 %

5.2.2.2 – Experimental Validation of Optimization Objectives with 20 V

Supply Voltage and 1400 rpm

The experimental validation is also conducted at a higher speed at 1400 rpm and 20 A current reference as shown in Fig. 5.31. The proposed optimization objectives in Opt 2 result in a slightly delayed turn-on angle, shown in Fig. 5.31(a). The source current has the same oscillation frequency for the older (Opt 1) and proposed optimization (Opt 2) objectives, with the proposed objectives having higher peak magnitudes as shown in Fig. 5.31(b). Similarly, due to the shorter conduction duration, the proposed optimization in Opt 2 draw a smaller amount of generating torque while having a similar torque ripple profile, shown in Fig. 5.31(c).

In Table 5.10, the Opt 1 and Opt 2 optimization objectives are compared using the experimental setup at the higher speed of 1400 rpm and 20 A current reference. Using the proposed optimization objectives in Opt 2, the RMS phase current decreased by 5.34 % due to the shorter conduction duration. The proposed optimization objectives result in 2.79 % less source current being supplied back to

the bidirectional power supply, but also extract 3.54 % less generating torque from the prime mover. The source current per torque supplied back to the bidirectional power supply only increased by 0.75 %.
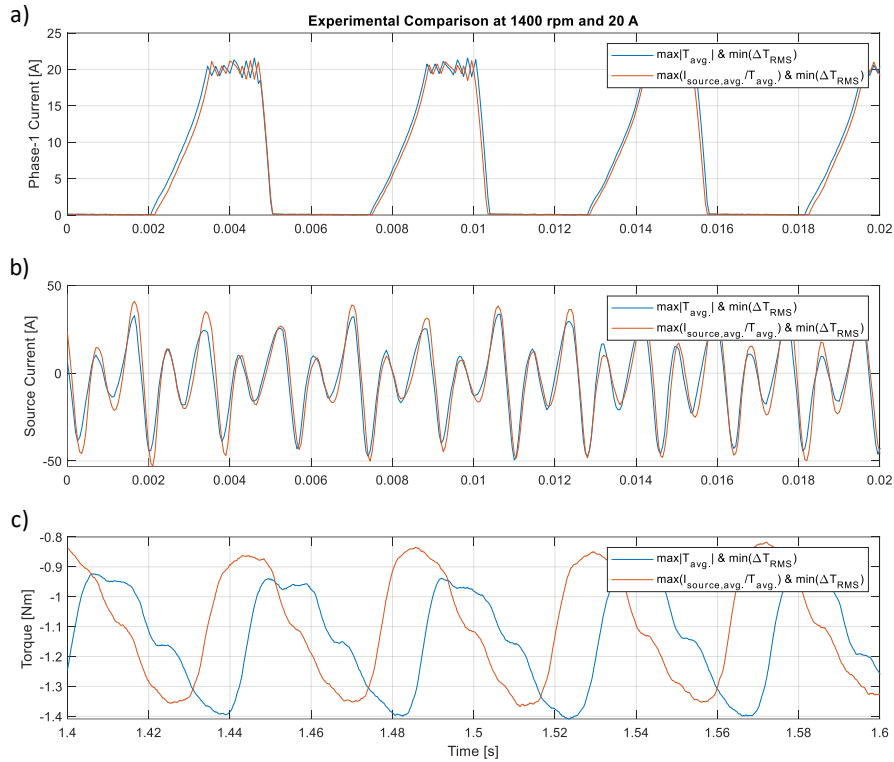
Fig. 5.31: Experimental results using 20 V DC-link at 1400 rpm and 20 A current reference for (a) phase-1 current (b) source current (c) shaft torque.

Table 5.10: Comparison of old, Opt 1 and new, Opt 2 optimization objectives using 20 V DC-link at 1400 rpm and 20 A current reference.

1400 rpm at 20 A_{ref}	Opt 1 $\max\|T_{avg}\|$ & $\min(\Delta T_{RMS})$	Opt 2 $\max\|I_{source,avg}/T_{avg}\|$ & $\min(\Delta T_{RMS})$	**Percent change**
Phase current RMS	7.67 A	7.26 A	5.34 %
Avg. source current	-2.87 A	-2.79 A	2.79 %
Avg. torque	-1.13 Nm	-1.09 Nm	3.54 %
Avg. source current per avg. torque	-2.53 A/Nm	-2.55 A/Nm	0.79 %

5.2.2.3 - Experimental Validation of Optimization Objectives with 72 V Supply Voltage and 1800 rpm

The power supply voltage is increased to 72 V to supply the experimental 12/8 SRM with the rated phase voltage. In Fig. 5.32(a), the proposed objectives in Opt 2 have a shorter conduction period of 0.71 degrees electrical when compared to the older objectives in Opt 1. In Fig. 5.32(b), similar to the 20 V DC-link cases the source current has the same oscillation frequency for both objectives, but the proposed objectives reduce the amount of source current drawn. In Fig. 5.32(c), the proposed objectives reduce the amount of prime mover torque extracted as well.
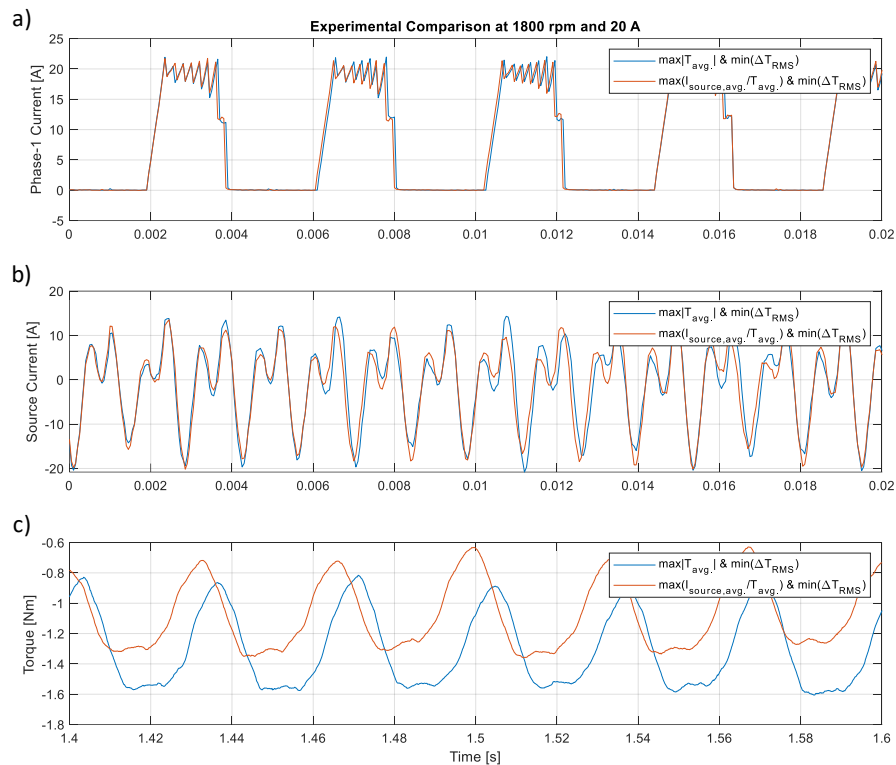
Fig. 5.32: Experimental results using 72 V DC-link at 1800 rpm and 20 A current reference for (a) phase-1 current (b) source current (c) shaft torque.

142

In Table 5.11, the old and proposed optimization objectives in Opt 1 and Opt 2 are compared using the experimental setup at 1800 rpm and 20 A current reference but with a 72 V DC-link voltage. Due to the slightly shorter conduction interval produced by the proposed optimization objectives in Opt 2, the phase current RMS reduced by 0.313 %. The average source current returned also improves marginally by 0.450 % using the proposed objectives in Opt 2. However, the proposed optimization greatly reduced the amount of prime mover torque extracted. This results in the average source current per average torque improving by 17.956 % when compared to the older objectives in Opt 1.

Table 5.11: Comparison of old, Opt 1 and new, Opt 2 optimization objectives using 72 V DC-link at 1800 rpm and 20 A current reference.

1800 rpm at 20 A$_{ref}$	Opt 1 $\max\lvert T_{avg}\rvert$ & $\min(\Delta T_{RMS})$	Opt 2 $\max\lvert I_{source,avg}/T_{avg}\rvert$ & $\min(\Delta T_{RMS})$	Percent change
Phase current RMS	7.672 A	7.648 A	0.313 %
Avg. source current	-0.888 A	-0.892 A	0.450 %
Avg. torque	-1.296 Nm	-1.104 Nm	14.815 %
Avg. source current per avg. torque	0.685 A/Nm	0.808 A/Nm	17.956 %

In Fig. 5.33, the speed is kept at 1800 rpm, and the current reference is increased to 30 A. In Fig. 5.33(a), the proposed optimization objectives in Opt 2 have a significantly earlier turn-off conduction angle which results in the conduction period to be reduced. The source current is largely similar in both cases, shown in Fig. 5.33(b). Similar to the 20 A case at 1800 rpm, the proposed objectives in Opt 2 extract much lower prime mover when compared to the older objectives in Opt 1, observed in Fig. 5.33(c).
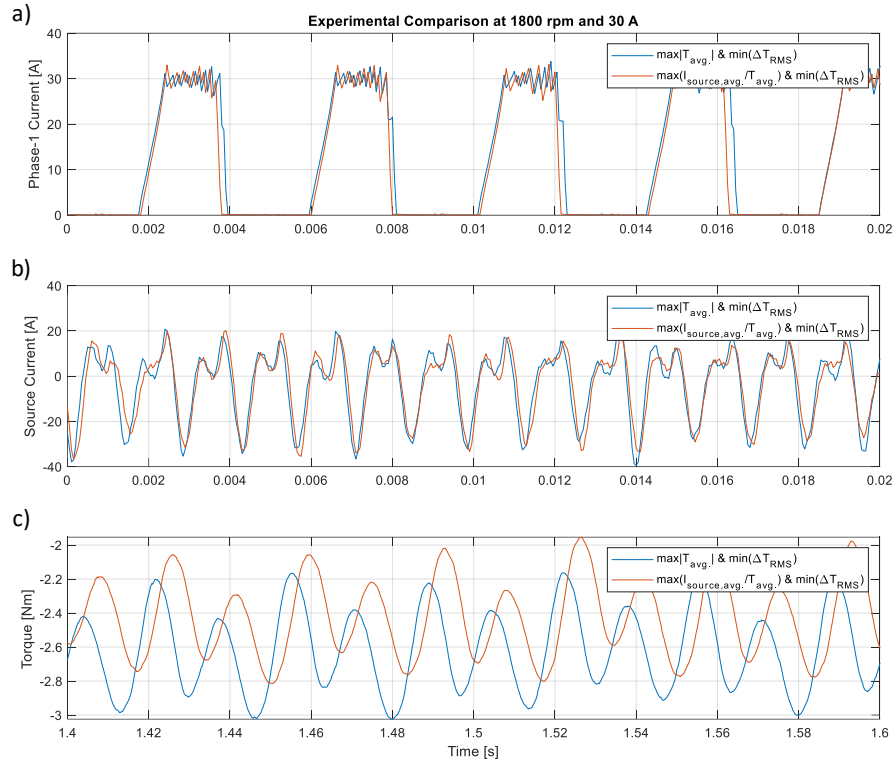
Fig. 5.33: Experimental results using 72 V DC-link at 1800 rpm and 30 A current reference for (a) phase-1 current (b) source current (c) shaft torque.

In Table 5.12, the old and proposed optimization objectives in Opt 1 and Opt 2 are compared using the experimental setup at 1800 rpm and 30 A current reference but with a 72 V DC-link. The significantly shorter conduction period is generated using the proposed optimization objectives in Opt 2, which results in the 9.535 % reduction in phase current RMS. The average source current for both cases is similar. The proposed optimization objectives result in the 6.902 % reduction in the amount of generating torque when compared to the older objectives in Opt 1. This leads to a 7.796 % increase in the amount of average source current per average torque when using the Opt 2 objectives when compared to the Opt 1 objectives.

Table 5.12: Comparison of old, Opt 1 and new, Opt 2 optimization objectives using 72 V DC-link at 1800 rpm and 30 A current reference.

1800 rpm at 30 A$_{ref}$	Opt 1 $\max\|T_{avg}\|$ & $\min(\Delta T_{RMS})$	Opt 2 $\max\|I_{source,avg}/T_{avg}\|$ & $\min(\Delta T_{RMS})$	**Percent change**
Phase current RMS	12.617 A	11.414 A	9.535 %
Avg. source current	-3.156 A	-3.167 A	0.349 %
Avg. torque	-2.637 Nm	-2.455 Nm	6.902 %
Avg. source current per avg. torque	1.197 A/Nm	1.290 A/Nm	7.769 %

5.2.2.4 - Experimental Validation of Optimization Objectives with 72 V Supply Voltage and 2600 rpm

In the next case, the speed is increased to 2600 rpm with a current reference of 20 A, and the DC-link supplying 72 V. In Fig. 5.34(a), the proposed objectives in Opt 2 have a delayed turn-on and earlier turn-off conduction angle which leads to shorter conduction interval when compared to the older objectives in Opt 1. In both cases, the same source current oscillation frequency is observed, but the proposed objectives slightly increasing the peak source current magnitude returned to the supply, shown in Fig. 5.34(b). The proposed objectives in Opt 2 greatly reduce the amount of generating torque as observed in Fig. 5.34(c).

In Table 5.13, the old (Opt 1) and proposed (Opt 2) optimization objectives are compared using the experimental setup at 2600 rpm and 20 A current reference. Similar to the 1800 rpm at 30 A case the proposed optimization objectives in Opt 2 reduce the conduction period when compared to the original objectives in Opt 1 which results in a 6.088 % reduction in phase current RMS. The Opt 2 objectives result in 1.056 % more source current returned when compared to the Opt 1

objectives. The proposed objectives result in the average generating torque to reduce by 9.689 % when compared to the older objective, which leads to an 11.828 % increase in the amount of average source current per average torque.
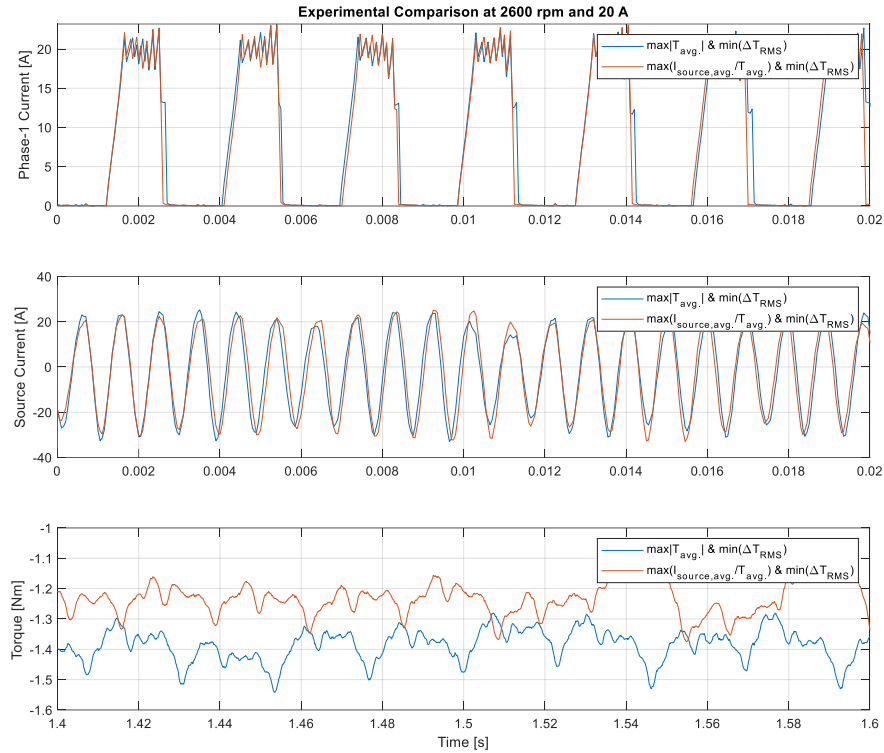
Fig. 5.34: Experimental results using 72 V DC-link at 2600 rpm and 20 A current reference for (a) phase-1 current (b) source current (c) shaft torque.

Table 5.13: Comparison of old, Opt 1 and new, Opt 2 optimization objectives using 72 V DC-link at 2600 rpm and 20 A current reference.

2600 rpm at 20 A_ref	Opt 1 $\max\lvert T_{avg}\rvert$ & $\min(\Delta T_{RMS})$	Opt 2 $\max\lvert I_{source,avg}/T_{avg}\rvert$ & $\min(\Delta T_{RMS})$	Percent change
Phase current RMS	8.311 A	7.805 A	6.088 %
Avg. source current	-1.800 A	-1.819 A	1.056 %
Avg. torque	-1.383 Nm	-1.249 Nm	9.689 %
Avg. source current per avg. torque	1.302 A/Nm	1.456 A/Nm	11.828 %

5.3 – Conclusion

In this chapter, the experimental setup is assembled to validate the proposed generating specific optimization objectives of $\max|I_{source,avg}/T_{avg}|$ and $\min(\Delta T_{RMS})$. The setup configuration is presented in detail and provides insight on how it is assembled from the ground up. A 12/8 SRM's static characteristics are determined using the voltage pulse method and rising phase current profile. The calculated torque is compared to the instantaneous shaft torque to validate the static characterization. The generating specific soft-switching current control conditions are compared to the motoring mode soft-switching current control. To ensure the conduction angles generated by the optimizer would yield similar experimental results, the experimental and simulation results are compared. The comparison shows acceptable correlation.

Using the experimental setup, the proposed objectives of $\max|I_{source,avg}/T_{avg}|$ and $\min(\Delta T_{RMS})$ are compared to the objectives $\max|T_{avg}|$ and $\min(\Delta T_{RMS})$ in generating mode using soft-switching. It was observed that at different DC-link voltages, rotor speeds, and current references, the amount of average source current per torque was improved. Additionally, the proposed objectives result in the phase current RMS value to decrease, which results in smaller copper losses.

Chapter 6. Summary

In this chapter, a summary is provided for the thesis content and presents the future work related to the thesis.

6.1 – Thesis Summary

The switched reluctance machine has several advantages over conventional electric motors such as induction machines and permanent magnet synchronous machines. Simple construction, robust structure, and low-cost manufacturing being some of the advantages. The most significant advantage for SRMs is the lack of permanent magnets or rotor excitation needed for operation. However, there are factors limiting the SRMs ability to be used in motoring and generating application, such as torque ripple, unique converter topology, acoustic noise, and vibration. Due to these limiting factors, the SRM is actively being explored to improve its performance. In this thesis, the SRM is explored in generating mode and is compared to motoring mode of operation. Using the comparison, optimization objectives are established to specifically improve generating mode of operation.

In Chapter 2, the fundamental electromagnetic principles of an SRM are discussed and the energy conversion process is shown. The non-linear nature of the SRM is shown and the concept of co-energy is outlined. The static characteristics of an 8/6 SRM are shown to better understand the motors operational behaviour, and the losses of an SRM are presented. Finally, the asymmetric bridge converter's modes of operation are shown for hard and soft-switching.

In Chapter 3, the generating mode of operation is introduced for the SRM, and the effects of hard and soft-switching are explored for different current references. The phase current and torque performance for the 8/6 SRM are compared using motoring conduction angles that were either shifted or mirrored to obtain generating conduction angles. The comparisons are shown for single pulse mode and current control to outline the differences in the rate of change in phase current behaviour and effect on the electromagnetic torque. Soft-switching current control conditions specific to generating mode are developed due to the motoring mode conditions not being able to control the phase current to a specified reference value. The new soft-switching conditions are then compared to hard-switching in generating mode at different rotor speeds.

In Chapter 4, generating specific optimization objectives are developed. The new objectives are determined using an exhaustive conduction angle search. The exhaustive search suggests three objects which need to be considered for the generating optimization are: average torque, torque ripple RMS, and source current. In most generating specific applications such as internal combustion engine alternators, the largest amount of source current is returned to the source while minimizing the amount of prime mover torque extracted, resulting in the source current and average torque objectives being combined. The torque ripple is kept as an independent objective and is minimized as it is attributed to acoustic noise and vibration. Using the exhaustive search, it was also determined that having the average torque and source current objectives independently considered results in the optimizer to have a large variation in the Pareto front. Furthermore, this

optimization completely omits the torque ripple objective. The proposed optimizer allows delayed generating conduction angles. Yet, due to the lower generating torque performance, and lower source current, and higher torque ripple, the optimizer did not utilize this capability. The proposed optimization in Opt 2 reduced the amount of prime mover torque for a similar amount of source current. This also results in smaller conduction interval when compared to the objectives in Opt 1. Finally, the Opt 2 optimization objectives result in a Pareto front which produces working conditions with less variation for all rotor speeds and current references.

In Chapter 5, an experimental setup capable of four-quadrant operation is constructed from the ground up to validate the generating specific optimization objectives. The setup configuration and assembly are discussed in detail. A 3-phase 12/8 SRM's static characteristics are determined using the voltage pulse method and the rising phase current profile. The experimental results match the simulation results, ensuring the conduction angles selected using MATLAB optimizer yield similar performance for the experimental setup. The proposed generating specific optimization objectives (Opt 2) of $\max|I_{source,avg}/T_{avg}|$ and $\min(\Delta T_{RMS})$ are compared to the objectives (Opt 1) of $\max|T_{avg}|$ and $\min(\Delta T_{RMS})$ at various DC-link voltages, rotor speeds, and current references. The $\max|I_{source,avg}/T_{avg}|$ objective is improved by 15.4 % on average due to the amount of prime mover torque being minimized while improving or maintaining the amount of source current returned to the supply. The proposed optimization objectives in Opt 2 also reduce the RMS value of phase current by 6.3 % on average for the experimental cases explored, which leads to less copper loss.

6.2 – Future Work

This thesis proposes objectives specific to generating mode and only explores the performance using conventional conduction angle control. However, to further validate whether the generating specific objectives and soft-switching current controller improve generating performance, more complex control schemes need to be explored such as Torque Sharing Functions. Additionally, current profiling conditions can be developed which are specific to generating mode of operation and consider the rate of change of current, and torque production capability and radial force reduction.

Experimental validation was not carried beyond the constant torque region for the 3-phase 12/8 SRM. Using the default software configuration for the bidirectional power supply, significant variation in the DC-link voltage is introduced as a part of the voltage-current regulation control loop at high-speed operation. This causes significantly lower DC-link voltage being applied during the initial excitation phase, and results in the experimental phase current to not having the same rate of change as the simulation phase current. By improving the voltage-current regulation of the bi-directional power supply, higher speeds experimental results can be explored where single pulse control can be utilized.

Chapter 7. References

[1]   "Energy Fact Book 2020-2021," Natural Resource Canada, 2020.
      Accessed: Oct. 2021. [Online]. Available: https://www.nrcan.gc.ca/

[2]   B. Bilgin, P. Magne, P. Malysz, Y. Yang, V. Pantelic, A. Korobkine, W.
      Jiang, M. Lawford, A. Emadi, "Making the Case for Electrified
      Transportation," *IEEE Transactions on Transportation Electrification*,
      vol. 1, no. 1, pp. 4-17, Jun. 2015.

[3]   D. Bauer, D. Diamond, J. Li, D. Sandalow, P. Telleen, B. Wanner, "U.S.
      Department of Energy Critical Materials Strategy," U.S. Department of
      Energy Office of Scientific and Technical Information, Dec. 2010.
      Accessed: Nov. 2021. [Online]. Available: https://www.osti.gov/biblio/

[4]   D. Fickling, "We All Need to Calm Down About Rare Earths,"
      Bloomberg Technology, May, 2019. Accessed: Nov. 2021. [Online].
      Available: https://www.bnnbloomberg.ca/

[5]   "Mineral Commodity Summaries 2021," U.S. Geological Survey, 2021.
      Accessed: Dec. 2021. [Online]. Available:
      https://pubs.er.usgs.gov/publication/mcs2021

[6]   "Rare Earth Elements: A Review of Production, Processing, Recycling,
      and Associated Environmental Issues," United States Environmental
      Protection Agency, Dec. 2012. Accessed: Nov. 2021. [Online].
      Available: https://nepis.epa.gov/

[7]   B. Bilgin, A. Emadi, "Electric Motors in Electrified Transportation: A
      step toward achieving a sustainable and highly efficient transportation
      system," *IEEE Power Electronics Magazine*, vol. 1, no. 2, pp. 10-17,
      Jun. 2014.

[8]   J. Ye, B. Bilgin, A. Emadi, "An Offline Torque Sharing Function for
      Torque Ripple Reduction in Switched Reluctance Motor Drives," *IEEE
      Transactions on Energy Conversion*, vol. 30, no. 2, pp. 726-735, Jun.
      2015.

[9]   H. Li, B. Bilgin, A. Emadi, "An Improved Torque Sharing Function for
      Torque Ripple Reduction in Switched Reluctance Machines," *IEEE*

Transactions on Power Electronics, vol. 34, no. 2, pp. 1635-1644, Feb. 2019.

[10] R. Tarvirdilu-Asl, S. Nalakath, B. Bilgin and A. Emadi, "A Finite Control Set Model Predictive Torque Control for Switched Reluctance Motor Drives with Adaptive Turn-off Angle," *IECON 2019 - 45th Annual Conference of the IEEE Industrial Electronics Society*, pp. 840-845, Oct. 2019.

[11] Z. Xia, B. Bilgin, S. Nalakath and A. Emadi, "A New Torque Sharing Function Method for Switched Reluctance Machines with Lower Current Tracking Error", *IEEE Transactions on Industrial Electronics*, vol. 68, no. 11, pp. 10612-10622, Nov. 2021.

[12] R. Yuan, Q. Cheng, S. Song, L. Ge, X. Zhao, R. Ma, W. Liu, "A Method of Torque Ripple Suppression of SRM based on Model Predictive Control," *2021 IEEE International Conference on Predictive Control of Electrical Drives and Power Electronics*, pp. 229-234, Nov. 2021.

[13] J. Liu, L. Wang, L. Yi, G. Zhu, X. Yin, "Optimization of SRM Direct Instantaneous Torque Control Strategy based on Improved Firefly Algorithm," *2019 IEEE 3rd Conference on Energy Internet and Energy System Integration*, pp. 364-368, Nov. 2019.

[14] N. Saha, S. Panda, D. K. Sahoo, "Modified Whale Optimization Technique for Combined Objective of Torque Ripple Minimization & Speed Control of SRM Drive," *2020 3rd International Conference on Energy, Power and Environment: Towards Clean Energy Technologies*, pp. 1-5, Mar. 2021.

[15] Z. Huang, L. Yi, J. Wan, "Research on optimization control of SRM system based on APSO algorithm," *The 27th Chinese Control and Decision Conference*, pp. 4953-4958, May, 2015.

[16] J. Deskur, T. Pajchrowski, K. Zawirski, "Optimal control of current commutation of high speed SRM drive," *2008 13th International Power Electronics and Motion Control Conference*, pp. 1204-1208, Sep. 2008.

[17] J. Gao, H. Sun, Y. Dong, L. He, "RBF Neural Network SMC design and torque ripple optimization research for switched reluctance motor," *Proceedings of the 30th Chinese Control Conference*, pp. 3512-3516, Jul. 2011.

[18] A. Shahabi, A. Rashidi, S. M. Saghaian-Nejad, "Torque ripple reduction of SRM drives below the base speed using commutation angles control," *2013 21st Iranian Conference on Electrical Engineering*, pp. 1-6, May, 2013.

[19] X. D. Xue, K. W. E. Cheng, J. K. Lin, Z. Zhang, K. F. Luk, T. W. Ng, N. C. Cheung, "Optimal Control Method of Motoring Operation for SRM Drives in Electric Vehicles," *IEEE Transactions on Vehicular Technology*, vol. 59, no. 3, pp. 1191-1204, Mar. 2010.

[20] M. K. Jha, N. Seth, N. Tyagi, S. A. Khan, "SRM Torque Ripple Reduction Using Grey Wolf and Teaching and Learning Based optimization in Hysteresis Control," 2021 International Conference on Intelligent Technologies, pp. 1-7, Jun. 2021.

[21] T. Kojima, R. W. De Doncker, "Optimal torque sharing in direct instantaneous torque control of switched reluctance motors," *2015 IEEE Energy Conversion Congress and Exposition*, pp. 327-333, Sep. 2015.

[22] F. Al-Amyal, L. Al Quraan, L. Szamel, "Torque Sharing Function Optimization for Extended Speed Range Control in Switched Reluctance Motor Drive," *2020 IEEE 3rd International Conference and Workshop in Óbuda on Electrical and Power Engineering*, pp. 119-124, Nov. 2020.

[23] Y. Wang, H. Wu, W. Zhang, Y. Ma, "A high efficiency direct instantaneous torque control of SRM using commutation angles control," *2014 17th International Conference on Electrical Machines and Systems*, pp. 2863-2866, Oct. 2014.

[24] M. M. Namazi, M. M. Borujeni, A. Rashidi, S. M. S. Nejad, J. W. Ahn, "Torque ripple reduction of switched reluctance motor drive with adaptive sliding mode control and Particle Swarm Optimization," *2015 IEEE International Conference on Advanced Intelligent Mechatronics*, pp. 371-376, Jul. 2015.

[25] M. Yaich, M. Ghariani, "Artificial intelligence-based control for torque ripple minimization in switched reluctance motor drives," *2017 18th International Conference on Sciences and Techniques of Automatic Control and Computer Engineering*, pp. 320-327, Dec. 2017.

[26] R. Abraham, S. Ashok, "Data-Driven Optimization of Torque Distribution Function for Torque Ripple Minimization of Switched

Reluctance Motor," *2020 International Conference for Emerging Technology*, pp. 1-6, Jun. 2020.

[27] B. Bilgin, J. W. Jiang, and A. Emadi, Switched Reluctance Motor Drives: Fundamentals to Applications. Boca Raton, FL, USA: CRC Press/Taylor & Francis Group, pp. 55-58, 2018.

[28] S. Zurek, K. Chwastek, "Co-energy," Encyclopedia Magnetica, Jan. 2016. Accessed: Nov. 2021. [Online]. Available: https://e-magnetica.pl/coenergy

[29] B. Bilgin, J. W. Jiang, and A. Emadi, Switched Reluctance Motor Drives: Fundamentals to Applications. Boca Raton, FL, USA: CRC Press/Taylor & Francis Group, pp. 58-61, 2018.

[30] B. Bilgin, J. W. Jiang, and A. Emadi, Switched Reluctance Motor Drives: Fundamentals to Applications. Boca Raton, FL, USA: CRC Press/Taylor & Francis Group, pp. 189-192, 2018.

[31] "Hot Rolled Steel A36 (44W in Canada)," Metal Supermarkets, Accessed: Dec. 2021. [Online]. Available: https://www.metalsupermarkets.com/hot-rolled-steel-a36/

[32] M. V. Terzic, H. Li, B. Bilgin, A. Emadi, "Comparison of Experimental Methods for Electromagnetic Characterization of Switched Reluctance Motors," *2018 XIII International Conference on Electrical Machines*, pp. 1881-1888, Sept. 2018.

[33] S. Song, L. Ge, S. Ma, M. Zhang, L. Wang, "Accurate Measurement and Detailed Evaluation of Static Electromagnetic Characteristics of Switched Reluctance Machines," *IEEE Transactions on Instrumentation and Measurement*, vol. 64, no. 3, pp. 704-714, Mar. 2015.